UNIVERSITY OF SUSSEX

DOCTORAL THESIS

Experimental and Numerical Investigation of Flow Structure and Heat Transfer in Gas Turbine HP Compressor Secondary Air Systems

Author:
Mark Richard
PUTTOCK-BROWN

Supervisor:
Prof. Martin G. ROSE

A thesis submitted in fulfillment of the requirements
for the degree of Doctor of Philosophy

in the

Thermo Fluid Mechanics Research Centre
School of Engineering and Informatics

March 2018

Declaration of Authorship

I, Mark Richard PUTTOCK-BROWN, declare that this thesis titled, "Experimental and Numerical Investigation of Flow Structure and Heat Transfer in Gas Turbine HP Compressor Secondary Air Systems" and the work presented in it are my own. I confirm that:

- This work was done wholly or mainly while in candidature for a research degree at this University.
- Where any part of this thesis has previously been submitted for a degree or any other qualification at this University or any other institution, this has been clearly stated.
- Where I have consulted the published work of others, this is always clearly attributed.
- Where I have quoted from the work of others, the source is always given. With the exception of such quotations, this thesis is entirely my own work.
- I have acknowledged all main sources of help.
- Where the thesis is based on work done by myself jointly with others, I have made clear exactly what was done by others and what I have contributed myself.

Signed:

_____

Date:

_____

"Improvise, Adapt, Overcome"

Abstract

With the continuing growth of the air traffic sector and a drive towards increasingly efficient aero engines the overall pressure ratio of such engines is set to climb. As a consequence, blade tip clearances will become proportionally larger as blade size decreases. Accurate sizing of the tip clearance is dependent on knowledge of the radial growth of the compressor discs, which in turn is dependent on their radial temperature gradient. Currently, 2D thermo-mechanical models based upon empirical correlations and scaling laws are used to predict this radial growth and the temperature increase in the secondary air system. These require knowledge of the buoyancy-induced flow that occurs in heated cavities between adjacent co-rotating discs.

This thesis presents experimental and numerical results of the heat transfer and flow structure of a buoyancy-induced rotating cavity flow field undertaken using the University of Sussex TFMRC Multiple Cavity Rig. This rig simulates the rotating components of a gas turbine secondary air system of a high pressure compressor. The objective is to gain a deeper understanding of the flow mechanisms operating within a rotating cavity at low Rossby numbers, representative of non-dimensional engine conditions and demonstrate that the shroud is the dominant source of heat transfer to the axial throughflow. The working conditions cover the range: $1.1 \times 10^5 < \mathrm{Re}_z < 5.1 \times 10^5$, $1.7 \times 10^6 < \mathrm{Re}_\theta < 3.2 \times 10^6$, $0.1 < \mathrm{Ro} < 0.6$, $0.32 < \beta\Delta T < 0.40$ and $3.1 \times 10^{11} < \mathrm{Gr} < 1.3 \times 10^{12}$ in Phase A and $1.2 \times 10^4 < \mathrm{Re}_z < 5.2 \times 10^4$, $1.5 \times 10^6 < \mathrm{Re}_\theta < 3.2 \times 10^6$, $0.05 < \mathrm{Ro} < 1.34$, $0.33 < \beta\Delta T < 0.51$ and $2.4 \times 10^{11} < \mathrm{Gr} < 1.6 \times 10^{12}$ in Phase B. The numerical study uses the working conditions: Gr$= 8.94 \times 10^{11}$, $\mathrm{Re}_z = 4.4 \times 10^4$, $\mathrm{Re}_\theta = 2.83 \times 10^6$, $\beta\Delta T = 0.35$, $\beta\Delta T_{av} = 0.14$ and Ro = 0.29.

Using experimental measurements of surface temperature, the Nusselt numbers on the rotating surfaces have been derived using a finite-element conduction solution. Monte Carlo simulation is used to give confidence intervals based on experimental uncertainty. New correlations have been derived for both the shroud and diaphragm and compared to existing literature. The shroud surface is shown to exhibit a magnitude of heat transfer similar to turbulent levels but with a trend - correlated to Grashof number - indicative

of laminar behaviour. This is thought due to unsteady laminar free convection. Also discussed is the shroud corner, the interface between the disc diaphragm and shroud, which has received little previous attention, yet shows a high level of heat transfer. The diaphragm Nusselt number correlation is based on a modified form of the Grashof number that acknowledges the effects of both free and forced convection inside the rotating cavity.

An accompanying numerical simulation has been conducted using Computational Fluid Dynamics to assess the complex nature of the buoyancy-induced cavity flow field. The 3D Unsteady Reynolds-Averaged Navier-Stokes equations with the SST k-ω turbulence model and experimentally measured boundary conditions are solved on a mesh of approximately 16 million elements. Validation of the numerical results is presented and includes comparison to measured high-frequency pressures on the static central shaft and air temperatures inside the rotating cavity . A type of Rayleigh-Bénard convection manifesting as a series of propagating streaks along the shroud periphery is identified and shown to modify the local Nusselt number, however their existence cannot be ratified without experimental evidence. Assessment of the cavity surface heat transfer shows that the shroud contributes 36%, the shroud corners 30%, the diaphragms 31% and the cobs 2%. Illustrating the shroud surface as the dominant heat transfer feature in the cavity system.

Acknowledgements

Firstly I would like to express my gratitude to my supervisor Prof. Martin Rose, for his guidance and support throughout. I would also like to acknowledge Dr Chris Long for his friendship and support even after he had retired. My gratitude is also extended to Mr Simon Davies for his technical wizardry and continual assistance. I would like to thank all my colleagues at the Thermo Fluid Mechanics Research Centre who make it such a great place to work. In particular Mr Harri Koivisto and Mr Daniel Payne (soon to be Dr's) for years of friendship and for proof-reading my thesis and Mr Reza Rafizadeh-farahani for his early work on the MCR. I would also like to thank the EPSRC and the University of Sussex for my initial funding and our industry partners for their continual input and discussion. I would also like to thank Steve Bancroft of Kulite Sensors Limited for supplying the unsteady pressure transducers used in this thesis. My thanks to my friends and family for their support and encouragement.

And finally, to my wife without whom I would never have succeeded.

Contents

List of Figures

List of Tables

List of Abbreviations

CFD	**C**omputational **F**luid **D**ynamics
C.I.	**C**onfidence **I**nterval
DNS	**D**irect **N**umerical **S**imulation
DSA	**D**igital **S**ensor **A**rray
FD	**F**inite **D**ifference
HP	**H**igh **P**ressure
R-B	**R**ayleigh-**B**énard
LDA	**L**aser **D**oppler **A**nemometry
LES	**L**arge **E**ddy **S**imulation
MCR	**M**ultiple **C**avity **R**ig
PDE	**P**artial **D**ifferential **E**quation
PRT	**P**latinum **R**esistance **T**hermometer
RANS	**R**eynolds-**A**veraged **N**avier-**S**tokes
RMS	**R**oot **M**ean **S**quare
TSW	**T**urbine **S**tator **W**ell
TVR	**T**urbulent **V**iscosity **R**atio
URANS	**U**nsteady **R**eynolds-**A**veraged **N**avier-**S**tokes

List of Symbols

a	inner radius	[m]
A	neck area	[m^2]
b	outer radius	[m]
C	specific heat capacity	
C_0, C_1, C_2, C_3	regression coefficients	
C_p	specific heat at constant pressure	[J/K]
d	probe diameter	[m]
D	outer diameter	[m]
d_h	hydraulic diameter	[m]
f_H	Helmholtz frequency	[Hz]
G	gap ratio	
Gr	Grashof number $(= \rho^2\Omega^2 b\beta\Delta T L^3/\mu^2)$	
Gr$_{sh}$	shroud Grashof number $(= \rho^2\Omega^2 b\beta\Delta T (s/2)^3/\mu^2)$	
Gr$_y$	modified Grashof number $(= \rho^2\Omega^2 r\beta\Delta T y^3/\mu^2)$	
k_{ti}	thermal conductivity of titanium (= 7.71)	[W/mK]
k_{air}	thermal conductivity of air (= 0.0271)	[W/mK]
L	characteristic length, neck length	[m]
$\dot{m}$	mass flow rate of axial throughflow	[kg/s]
N_r	rotor rotational speed	[1/s]
N_s	shaft rotational speed	[1/s]
Nu	Nusselt number $(= q_C L/k\,(T - T_{ref}))$	
Nu$_{sh}$	shroud Nusselt number $(= q_{sh}(s/2)/k(T_{sh} - T_{ref}))$	
Nu$_y$	modified Nusselt number $(= q_C y/k(T - T_{in}))$	

P	static pressure	[Pa]
$P*$	reduced static pressure	[Pa]
Pr	Prandtl number $(= \mu C_p/k)$	
q_C	conductive heat flux	[W/m^2]
q_R	radiative heat flux	[W/m^2]
q_T	total heat flux $(= q_C + q_R)$	[W/m^2]
Q_v	volumetric heat generation rate	[W/m^3]
r	radial coordinate	[m]
r_s	shaft radius	[m]
Ra	Rayleigh number $(=$ Gr $\cdot$ Pr$)$	
Ra′	modified literature Rayleigh number	
Re$_d$	sphere Reynolds number $(= \rho V_\theta d/\mu)$	
Re$_\theta$	rotational Reynolds number $(= \rho\Omega b^2/\mu)$	
Re$_y$	modified Reynolds number $(= \rho\Omega y^2/\mu)$	
Re$_z$	axial Reynolds number $(= \rho W d_h/\mu)$	
Ro	Rossby number $(= W/\Omega a)$	
s	axial distance between discs	[m]
S	surface length	[m]
t	diaphragm thickness	[m]
T	temperature	[K]
$T*$	reduced static temperature	[K]
T_f	film temperature $(= (T_s + T_{in})/2)$	[K]
$\mathbf{v}$	velocity vector	
V	cavity volume	[m^3]
V_r	radial velocity	[m/s]
V_z	axial velocity	[m/s]
V_θ	tangential velocity	[m/s]
W	axial velocity of throughflow	[m/s]
x	nondimensional radius $(= r/b)$	

y	distance from shroud $(= b - r)$	[m]

Greek Symbols

β	volumetric coefficient of expansion	[1/K]
Δ	temperature difference	[K]
ϵ	emissivity	
Θ	nondimensional temperature $(= (T - T_{in})/(T_{sh} - T_{in}))$	
μ	dynamic viscosity	[m^2/s]
ρ	density	[kg/m^3]
σ	Stefan-Boltzmann constant $(= 5.67 \times 10^{-8})$	[Wm/K^4]
Ω	angular speed of discs	[1/s]
ω	vorticity	[1/s]

Subscripts

0	total conditions
av	average
cav	cavity
C	cold
f	flow
H	hot
in	inlet
p	probe
r	radial direction
ref	reference value
rel	relative
s	surface
sh	shroud
θ	circumferential direction
z	axial direction
∞	free stream

To my wife, for all her patience and love. . .

1 Introduction

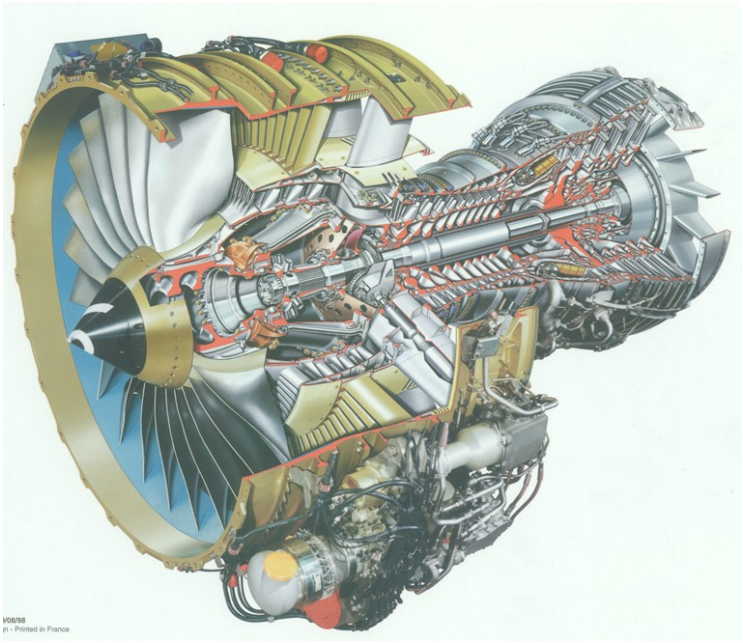

FIGURE 1.1: CFM International CFM56-7B, contemporary civil turbofan engine. Courtesy of CFM International

Demand for higher thermal efficiency, lower specific fuel consumption, improved thrust-to-weight ratio and longer component life in the modern civil turbofan engine (Figure 1.1) is driving innovation forward. These have, in part, been achieved through increasing bypass ratios (typically 10-1 in the latest generation engines, e.g. GE9X or Trent 1000) and higher overall pressure ratios (60:1 for the GE9X). This trend is set to continue with the Rolls-Royce Advance and Ultrafan engines (set for release in 2020 and 2025 respectively) pushing bypass ratios up to 15:1 and pressure ratios to 70:1. This will result in even smaller engine cores and reduced compressor blade heights. Between the compressor stationary casing and rotating blades is the tip clearance. On the assumption that this will remain constant, any decrease in blade height will result in proportionally

larger clearances, reducing stability and increasing aerodynamic losses, making it more difficult to maintain efficiency.

With high pressure (HP) compressor exit temperatures above 900K and rotational speeds above 10000 rpm the main contributing factor to tip clearance is radial growth of the compressor rotor discs. The need to accommodate the rapid radial growth of the rotating discs during an emergency situation, such as an aborted landing, determines the cold build clearances, which may include an acceptable level of blade rub. This, however, will increase the tip gap and reduce the efficiency of the compressor. To accurately determine the clearance requires a thermo-mechanical prediction of the compressor across the operating envelope. Whilst the rotational stress is relatively straightforward to predict, thermal stress due to the radial temperature gradient on the compressor discs is much more complex. This is due to the need to account for buoyancy-induced flow and heat transfer and predict disc temperatures inside the cavities formed between adjacent co-rotating discs of the compressor.

Engine design predictions using 2D axisymmetric thermo-mechanical models typically rely on a series of empirical correlations and scaling factors obtained by matching to test engine measurements. Not only is accurate predictions of tip clearance important but also the temperature increase of the internal cooling air as it flows through the HP compressor. Given that the turbine inlet temperatures of modern aero engines (above 2000K) are above the melting point of the materials used, a significant percentage of air must be bled from the compressor into an internal air system. This air is critical for turbine cooling and is also used throughout the engine. Without an internal air system, the modern gas turbine could not function.

Figure 1.2 shows a schematic of a typical HP compressor. Each stage of the compressor is formed by a stator-rotor pair, with the rotor discs joined together to form a single rotating drum. Between the stationary casing and rotor blades is the tip clearance. The upstream cooling air flows in the annular space formed between the rotor drum and central shaft. Each rotating cavity is formed by a pair of co-rotating discs inside which a buoyancy-induced flow field occurs. The outer surface of each cavity is formed by a

shroud. Under these circumstances the heat transfer is dependent on the temperature of the discs and vice-versa, giving a conjugate heat transfer problem.

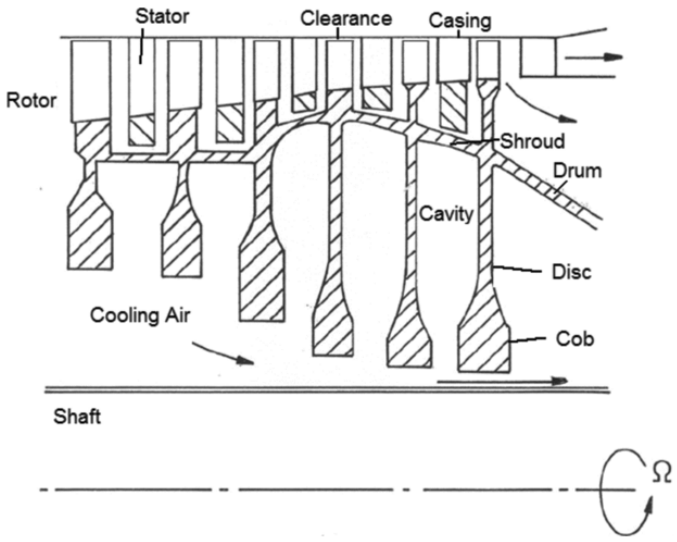

FIGURE 1.2: Schematic of a somewhat dated HP Compressor, from Owen and Long (2015)

The unsteady and unstable nature of buoyancy-induced flow in rotating cavities and the thermal transients of the engine mean that coupled fluid-solid prediction using computational fluid dynamics (CFD) is currently unfeasible for practical use in engine design, where typically many iterations are needed in a relatively short timescale. Consequently, 2D axisymmetric thermo-mechanical design models will still be required for the foreseeable future. However, this does not mean that CFD cannot be used to understand the dynamics of the flow field and used to gain insight into buoyancy-induced rotating flows. This thesis uses both experimental and numerical methods to develop new empirical correlations for such systems and gain further insight into the nature of the buoyancy-induced rotating cavity flow field. In particular, attention is paid to the shroud surface between the co-rotating discs.

2 Literature Review

2.1 Nondimensional Parameters and Geometry

2.1.1 Geometry

The geometry of a simplified cavity with axial throughflow commonly found in the HP compressor of a gas turbine is shown in Figure 2.1. Formed from two adjacent co-rotating discs the terms shroud, diaphragm and cob denote the outer casing, the thin parallel-sided section of the disc and the protuberant area at low radius respectively. In this work the term shroud corner is used to denote the fillet radius joining the diaphragm and shroud surfaces. A simple rotating cavity does not feature the cobs and a square corner is used in place of a fillet radius for the shroud corner. All disc sections rotate at the same angular speed Ω. An inner shaft rotates independently of the discs. Between this and the cobs an annular area is formed where the axial throughflow air flows, commonly referred to as the bore region.

The literature standard symbols used to describe the dimensions of the cavity system are: disc-to-disc axial spacing s, diaphragm thickness t and radius of the inner shaft r_s. The dimensions a and b denote the inner and outer radii of the cavity. The cylindrical coordinate system with radial r, circumferential θ and axial z directions is used.

Nondimensional geometric parameters allow comparison between different engine and experimental configurations. The nondimensional radius x is defined as:

$$x = r/b \tag{2.1}$$

the gap ratio G as:

$$G = s/b \tag{2.2}$$

and the clearance ratio as d_h/b, where $d_h = 2(a - r_s)$, the hydraulic diameter of the annulus formed between the cobs and central shaft.

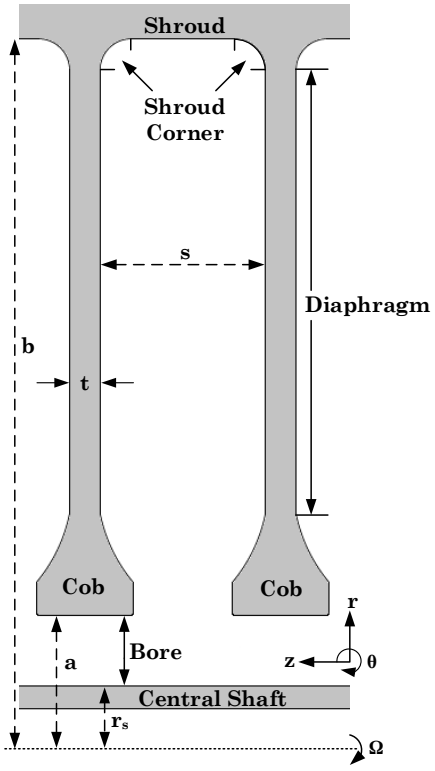

FIGURE 2.1: Schematic diagram of a rotating cavity

2.1.2 Nondimensional Flow Parameters

The nondimensional parameters presented here describe the working conditions of an engine or experiment and are based on the geometric parameters described in Figure 2.1. Fluid properties are evaluated where appropriate, though it is typical in rotating cavities for these to be in the axial throughflow.

The rotational speed is described by the rotational Reynolds number Re_θ such that:

$$\mathrm{Re}_\theta = \frac{\rho \Omega b^2}{\mu} \tag{2.3}$$

where ρ is the density and μ the viscosity. The axial throughflow via the axial Reynolds number Re_z:

$$\mathrm{Re}_z = \frac{\rho W d_h}{\mu} \tag{2.4}$$

where W is the bulk-average axial throughflow velocity and d_h the hydraulic diameter. These are commonly combined to give the Rossby number, Ro, defined as:

$$\mathrm{Ro} = \frac{W}{\Omega a} = \frac{b^2}{d_h a}\frac{\mathrm{Re}_z}{\mathrm{Re}_\theta} \tag{2.5}$$

which is the ratio of inertial to Coriolis forces. A low Rossby number (typically found in engines) indicates a rotationally dominated system, whilst a high number indicates an axial throughflow dominated system. A stationary cavity gives Ro =∞.

With heating in the cavity, buoyancy-induced flow can occur. To describe such a free (or natural) convection system the Grashof number Gr is used, describing the ratio of buoyancy forces to viscous forces, such that:

$$\mathrm{Gr} = \frac{\rho^2 \Omega^2 b \beta \Delta T L^3}{\mu^2} = \left(\frac{L}{b}\right)^3 \mathrm{Re}_\theta^2 \beta \Delta T \tag{2.6}$$

where L is a characteristic length - commonly for rotating cavities this is the radial extent of the disc $(b - a)$. The acceleration term $\Omega^2 b$ replaces the conventionally used gravitational acceleration g. The term $\beta \Delta T$ is the buoyancy parameter where; β is the volumetric coefficient of expansion - which for a perfect gas is $\beta \approx T_{in}^{-1}$, where T_{in} is the cavity inlet air temperature; and ΔT is the shroud to cavity inlet temperature difference $(T_{sh} - T_{in})$, where T_{sh} is the shroud temperature.

Another commonly used alternative parameter is the Rayleigh number Ra defined as:

$$\mathrm{Ra} = \mathrm{Gr} \cdot \mathrm{Pr} \tag{2.7}$$

where Pr= $\mu C_p / k$ is the Prandtl number.

2.1.3 Nondimensional Heat Transfer Parameters

To describe the heat transfer present in a rotating cavity system it is again necessary to nondimensionalise the relevant variables. Commonly the disc temperatures are expressed in nondimensional terms such that:

$$\Theta = \frac{T - T_{in}}{T_{sh} - T_{in}} \tag{2.8}$$

where T denotes a local disc temperature. Similar forms can be used to express the cavity air temperatures.

The Nusselt number Nu describes the heat transfer such that:

$$\mathrm{Nu} = \frac{q_C L}{k_{air}\left(T - T_{ref}\right)} \tag{2.9}$$

where q_C is the local wall normal conductive heat flux, T the local wall temperature, k the thermal conductivity and L a relevant length scale. Typically the length scale when evaluating the local disc Nusselt numbers is r. For rotating cavity systems, the axial throughflow inlet temperature is commonly used as the reference air temperature T_{ref}.

It is common also to describe the rotating cavity system based on an average disc Nusselt number, such that:

$$\mathrm{Nu}_{av} = \frac{q_{av} b}{k_{air} \Delta T_{av}} \tag{2.10}$$

where a radially-weighted average value of q_{av} and T_{av} between radius b and r is used such that:

$$q_{av} = \frac{2}{(b^2 - a^2)} \int_r^b q_C r \mathrm{dr} \tag{2.11}$$

and

$$\Delta T_{av} = \frac{2}{(b^2 - a^2)} \int_r^b \Delta T r \mathrm{dr} \tag{2.12}$$

It is shown in the last two sections that buoyancy-induced flow and heat transfer in rotating cavities is dependent on a number of nondimensional parameters, eventually reducible to Ro and Re_θ and $\beta \Delta T$. The local Nusselt number is therefore dependent on

these parameters as well as the temperature distribution on the disc due to the conjugate nature of the system (Owen and Long, 2015).

2.2 Flow Structure

The flow structure of a rotating cavity with axial throughflow is reviewed, firstly the isothermal flow scenario is considered and then the buoyancy-induced flow of the non-isothermal case.

2.2.1 Isothermal Flow

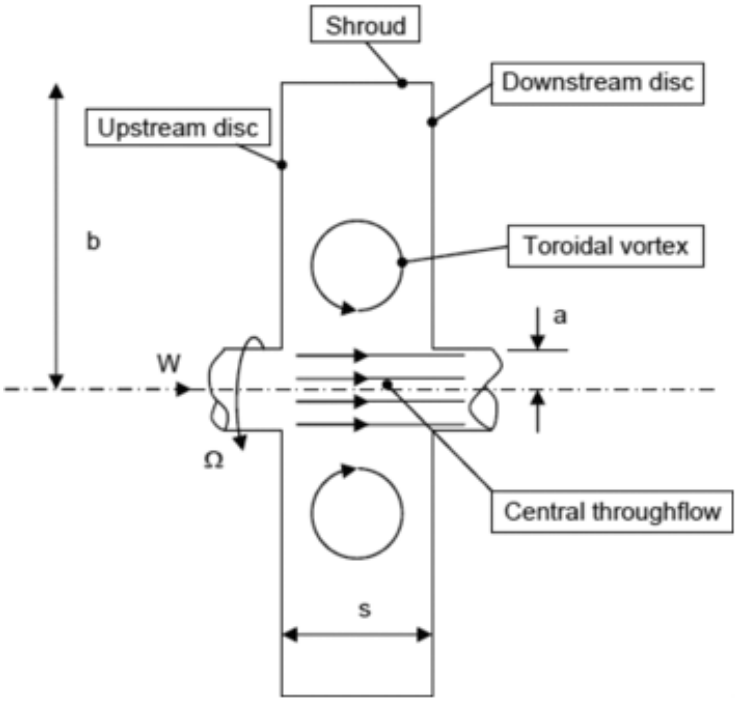

FIGURE 2.2: Schematic diagram of flow structure in an isothermal rotating cavity with axial throughflow, r-z plane, from Owen and Long (2015)

Figure 2.2 shows a simplified diagram of the flow inside a rotating isothermal cavity, where the axial throughflow creates a toroidal vortex in the cavity. An increase in rotational speed has the effect of suppressing the toroidal vortex whilst an increase in the throughflow extends the radial extent of the vortex. Owen and Pincombe (1979) used

Laser-Doppler Anemometry (LDA) and flow visualisation on a simplified isothermal rotating cavity where $G = 0.53$ and $a/b = 0.1$ without a central shaft. Tests were conducted over $0.8 <$ Ro $< \infty$. The extent of the toroidal vortex was observed to decrease with Ro; radially outward of the vortex solid-body rotation occurred. Inside the toroidal vortex the tangential velocity to disc rotational speed or swirl ratio $V_\theta/\Omega r$ was observed to exceed 1.

Farthing et al. (1992b) used similar LDA and flow visualisation techniques in four different rotating cavities, where $a/b \approx 0.1$ in all cases with gap ratios over the range $0.133 < G < 0.533$ without a central shaft. The Rossby number was varied such that $1 <$ Ro $< \infty$ with constant axial Reynolds number $\mathrm{Re}_z = 5000$. A phenomena referred to as *vortex breakdown* which has been observed as axisymmetric or non-axisymmetric was found. In the latter the central throughflow departs from the central axis and precesses around the cavity creating non-axisymmetric flow in the cavity. This was also observed by Owen and Pincombe (1979). The radial extent of the toroidal vortex was seen to decrease with Ro and G.

2.2.2 Nonisothermal Flow

In the nonisothermal case buoyancy-induced flow becomes dominant. Farthing et al. (1992b) found that when the rotating cavity is heated, either symmetrically (both discs heated) or asymmetrically (only one disc heated) the flow develops into a non-axisymmetric system of cyclonic and anti-cyclonic circulations. The axial throughflow enters the cavity radially via a structure referred to as a *radial arm*, similar to a rising plume of smoke, and bifurcates into two circulation zones. A *dead zone* was found between the two zones, so-called as no smoke was seen to enter the core area. However a radial inflow was observed to occur in the Ekman layers (Figure 2.3). Three gap ratios, $0.12 < G < 0.27$ were tested using smoke visualisation and found to exhibit highly unsteady 3D buoyancy-induced flow in all cases. The LDA measurements showed that the core of the cavity flow had a swirl ratio of slightly less than one, indicating it precessed slower than the discs. Though there was an effect of G, ΔT and Ro, typically it was found that $0.9 < V_\theta/\Omega r < 1$.

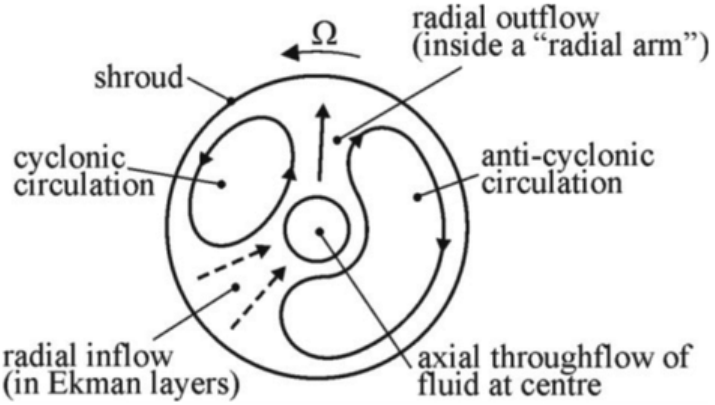

FIGURE 2.3: Schematic diagram of flow structure in a nonisothermal rotating cavity with an axial throughflow r-θ plane, from Farthing et al. (1992b)

Bohn et al. (2000) used ammonium chloride smoke and laser sheet illumination on the cavity mid-axial plane, with symmetrically heated discs and axial throughflow. A co-rotating central shaft was used with $a/b = 0.3$, $G = 0.2$ and $d_h/b = 0.09$. Though the working parameters - $2 \times 10^5 < \mathrm{Re}_\theta < 8 \times 10^5$ and $2 \times 10^4 < \mathrm{Re}_z < 7 \times 10^4$ - were markedly different, similar flow structures to those found by Farthing et al. (1992b) were observed. The visualisation results indicated laminar behaviour across all experimental conditions with a swirl ratio typically $0.88 < V_\theta/\Omega r < 0.9$. Qualitative observations were made of the cyclonic, anti-cyclonic, radial arm and dead zone, referred to as the centripetal zone. Figure 2.4 shows the mid-axial plane in the centripetal zone, where there is an indication of a radially inflowing structure (leftmost picture central dark zone) with smoke structures rolling up on either side indicating this may be a jet, moving faster than the surrounding flow.

Owen and Powell (2004) obtained LDA measurements in an axial throughflow rig with working parameters $4 \times 10^5 < \mathrm{Re}_\theta < 3.2 \times 10^6$ and $0.05 < \mathrm{Ro} < 14$ for $a/b = 0.4$ and $G = 0.2$. Only the downstream disc was heated and a central shaft was used. Spectral analysis of the velocity measurements indicated a multi-celled flow structure consisting of one, two or three pairs of cyclonic and anti-cyclonic circulations. The steady-state time-averaged LDA results indicated a swirl ratio $0.96 < V_\theta/\Omega r < 0.99$ for $0.67 < x < 0.97$.

Long, Miche, and Childs (2007) presented LDA measurements from the University of Sussex Multiple Cavity Rig (MCR). This rig is a 70% replica of a HP compressor rotor

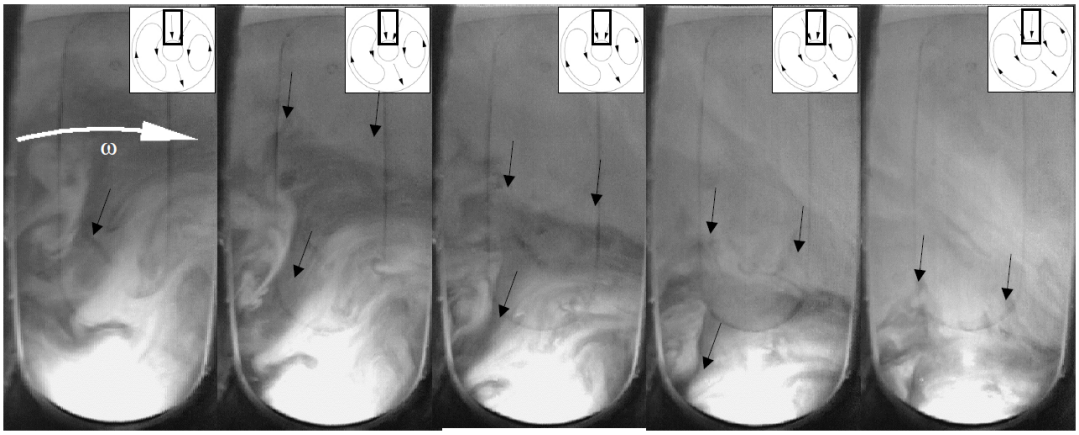

FIGURE 2.4: Flow visualisation of centripetal zone by Bohn et al. (2000)

with $a/b = 0.318$ and $G = 0.195$. Similar to an engine, the shroud was heated directly via an external supply of pressurised hot air. The rig also featured an axial throughflow of cooling air and a central shaft that could co-rotate, counter-rotate or remain stationary. Figure 2.5 shows a schematic of the MCR used by Long, Miche, and Childs (2007), LDA measurements were taken from cavities 2 and 3.

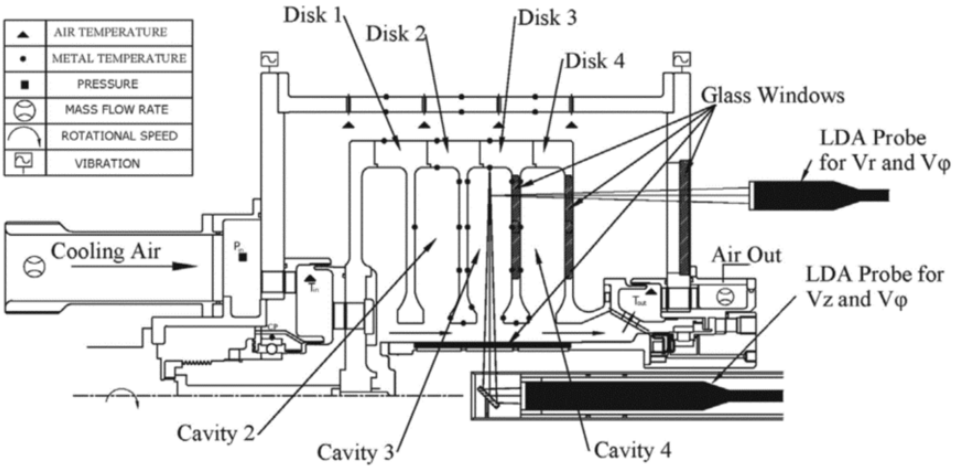

FIGURE 2.5: The Multiple Cavity Rig (MRC) from Long, Miche, and Childs (2007)

Figure 2.6 shows the values of swirl ratio $V_\theta/\Omega r$ across a range of Rossby numbers and two different values of d_h/b, referred to as *wide* and *narrow* with $d_h/b = 0.164$ and $d_h/b = 0.092$ respectively. Although there is a tendency for increasing Ro to increase the swirl ratio in the inner part of the cavity, there is more of an effect due to the clearance

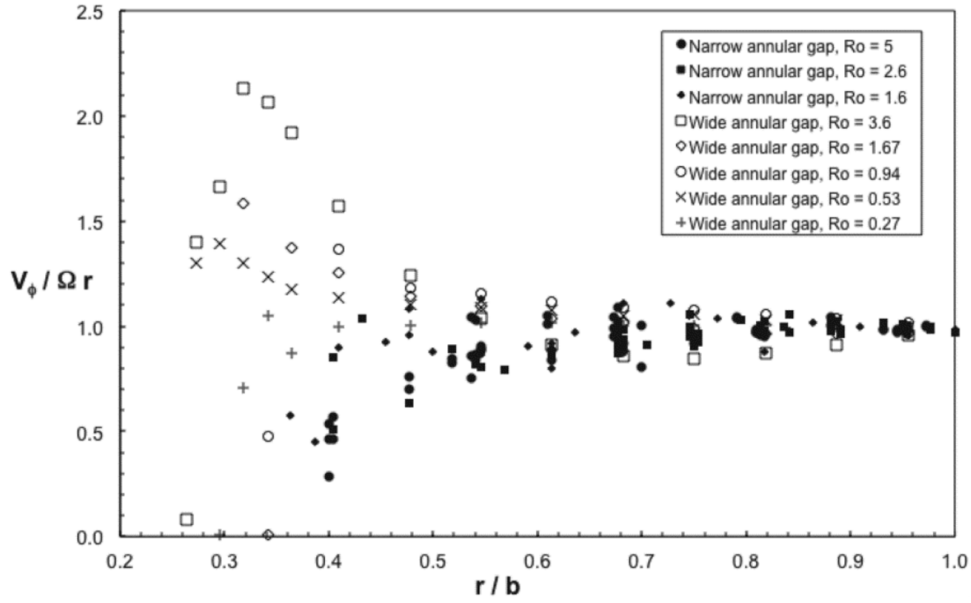

FIGURE 2.6: Radial distribution of swirl ratio, $V_\theta/\Omega r$ in a rotating cavity with axial throughflow showing the effects of clearance ratio, d_h/b and Rossby number, Ro, from Long, Miche, and Childs (2007)

ratio. In all cases the value of $V_\theta/\Omega r$ tends to one in the outer part of the cavity and the toroidal vortex is thought suppressed at lower radius for all *narrow* cases as the swirl ratio is less than one. It was also shown that the axial velocities inside the cavity were essentially zero, consistent with the Taylor-Proudman theorem, and that radial velocities were comparable to relative tangential velocities.

2.3 Heat Transfer in Rotating Cavities

Here the heat transfer in rotating cavities is presented. Firstly the closed cavity is considered, with attention paid to the shroud, followed by the open rotating cavity and heat transfer from the discs.

2.3.1 Closed rotating cavity

With a closed cavity the buoyancy-induced flow can develop unperturbed without interaction with the axial throughflow. With a heated shroud and cooled inner radius (due to the axial throughflow) the system is analogous to two parallel horizontal plates in a

gravitational field. In this circumstance the Rayleigh number is defined as:

$$\text{Ra} \equiv \text{Pr}\frac{\rho^2 \beta \Delta T g d^3}{\mu^2} \equiv \text{PrGr} \tag{2.13}$$

where d is the vertical distance between the plates and ΔT is the plate temperature difference $\Delta T = T_H - T_C$. When Ra > 1708, with the hotter surface on the bottom, a mode of unstable heat transfer referred to as *Rayleigh-Bénard convection* develops. This critical value of Ra indicates when the buoyancy effects overcome the viscous. Rayleigh-Bénard (R-B) convection is characterised by a series of counter-rotating vortices, shown in Figure 2.7. The semi-empirical correlation of Grossmann and Lohse (2000) approximates the

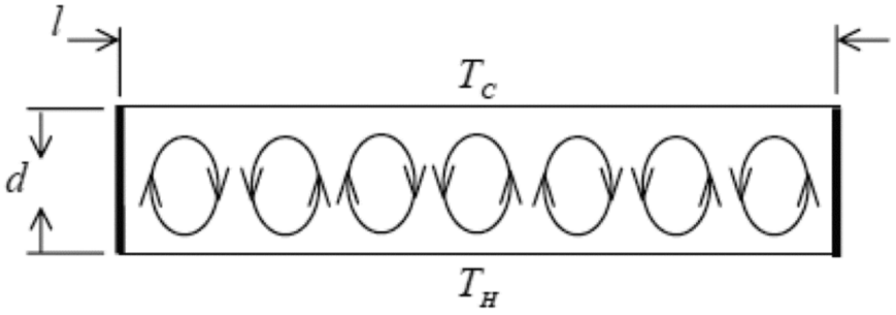

FIGURE 2.7: Rayleigh-Bénard convection between horizontal plates where $T_H > T_C$

Nusselt number for this type of convection over ten orders of magnitude of Ra, such that:

$$\text{Nu}' = 0.27\text{Ra}^{1/4} + 0.038\text{Ra}^{1/3} \tag{2.14}$$

for Pr = 1. In this case Nu′ = 1 would imply heat transfer due purely to conduction. This would be the case when the upper surface is hotter in R-B convection and the flow thermally stratifies.

The use of two powers laws is required to account for the differing regimes; determining whether the boundary layer or bulk flow dominates the global kinetic and thermal dissipation, respectively and whether the thermal or kinetic boundary layer is thicker. In the case of rotating cavities the Coriolis forces would tend to attenuate velocity fluctuations and so it is likely that this critical value of Ra′ = 1708 would be much higher than

a stationary cavity. Whilst the bulk convection may itself be turbulent the heat transport is limited by the laminar boundary layers on the plate. Recently He et al. (2012) took measurements over the Rayleigh number range $10^{12} \leq \text{Ra} \leq 10^{15}$ and Prandlt number near 0.8, a transition region between $10^{13} \leq \text{Ra} \leq 5 \times 10^{14}$ was identified by in the exponent of the fitted relationship $\text{Nu} \propto \text{Ra}^{\gamma_{eff}}$ where γ_{eff} changed from 0.31 - consistent with classical turbulent Rayleigh-Benard convection with laminar boundary layers - to 0.38 indicating turbulent boundary layers on the plate.

Bohn et al. (1995) performed experiments on a closed cavity with a heated shroud with three different geometric configurations. Using a modified version of Equation 2.13 such that:

$$\text{Ra}' = \text{Pr}\beta\Delta T\frac{\Omega^2 r_m \left(b-a\right)^3}{\nu^2} \tag{2.15}$$

where r_m is the mean radius. This replaces the gravitational term in Equation 2.13 with a rotational term. Using experimental results three empirical correlations were produced, one for each configuration, such that:

$$\begin{aligned}
\text{Case A:} \quad \text{Nu} &= 0.246\text{Ra}'^{0.228}, \quad a/b = 0.35, \quad G = 0.34 \\
\text{Case B:} \quad \text{Nu} &= 0.317\text{Ra}'^{0.211}, \quad a/b = 0.52, \quad G = 0.34 \\
\text{Case C:} \quad \text{Nu} &= 0.365\text{Ra}'^{0.213}, \quad a/b = 0.52, \quad G = 0.50
\end{aligned} \tag{2.16}$$

Where case C featured radial partitions to create eight 45 degree segments. All for values of Ra' up to 10^{12} and $\beta\Delta T$ up to 0.3 where Nu was the shroud Nusselt number. The attenuation of convection due to Coriolis forces delays transition so it is unclear whether the correlations describe laminar or turbulent boundary layers behaviour but given the limited range of $\text{Ra}' \leq 10^{12}$ it is considered likely that laminar convection is present.

Tang and Owen (2018) modelled buoyancy-induced flow in a closed rotating cavity assuming laminar free convection and found an analytical solution for the Nusselt number, such that:

$$\text{Nu} = ca\text{Ra}'^{1/4}\left(1-\chi\text{Re}_\theta^2\right)^{5/4} \tag{2.17}$$

where c is an empirical constant, a is a geometric parameter, χ is a compressibility parameter. Due to compressibility effects in the core and for constant ΔT a maximum value of Nu is found at a critical Reynolds number:

$$\mathrm{Re}_{crit} = \left(\frac{9}{4}\chi\right)^{-1/2} \tag{2.18}$$

The authors found generally good agreement to the measured experiments of Bohn et al. (1995) and suggest that buoyancy-induced flow in closed cavities remains laminar at values of Ra' approaching 10^{12}. Additionally, compressibility effects are postulated as the reason for the correlations of Bohn et al. (1995) (Equation 2.16) showing an exponent slightly less than $1/4$, the value typically associated with laminar flow.

2.3.2 Shroud heat transfer for rotating cavities with axial throughflow

Long and Tucker (1994b) used the simplified rotating cavity shown in Figure 2.8(a), with $a/b = 0.1$, $G = 0.13$ and without a central shaft to investigate the heat transfer from the shroud over the parameter range; $\beta\Delta T \leq 0.3$, $2 \times 10^3 \leq \mathrm{Re}_z \leq 1.6 \times 10^5$ and $2 \times 10^5 \leq \mathrm{Re}_\theta \leq 2 \times 10^6$. The heat flux on the shroud was measured at two locations using thermopile fluxmeters. The cavity air temperature was also measured using an exposed thermocouple at the end of a 1 mm diameter probe, Figure 2.8(b), at the cavity mid-axial plane and used as a reference temperature for Grashof and Nusselt numbers. Whilst no correlation was produced, it was found that the shroud Nusselt numbers were in close agreement to established correlations for laminar natural convection from a horizontal plate, provided the cavity air temperature was used as a reference. The shroud heat transfer was found to be insensitive to disc surface temperature distribution. The air temperature inside the cavity is strongly affected by disc surface temperature distribution yet there was no systematic variation of nondimensional cavity air temperature with Re_z or Re_θ.

Long and Childs (2007) used the MCR (shown in Figure 2.5) to measure shroud Nusselt numbers for cavities 2 and 3. Using two embedded thermocouples at the same axial

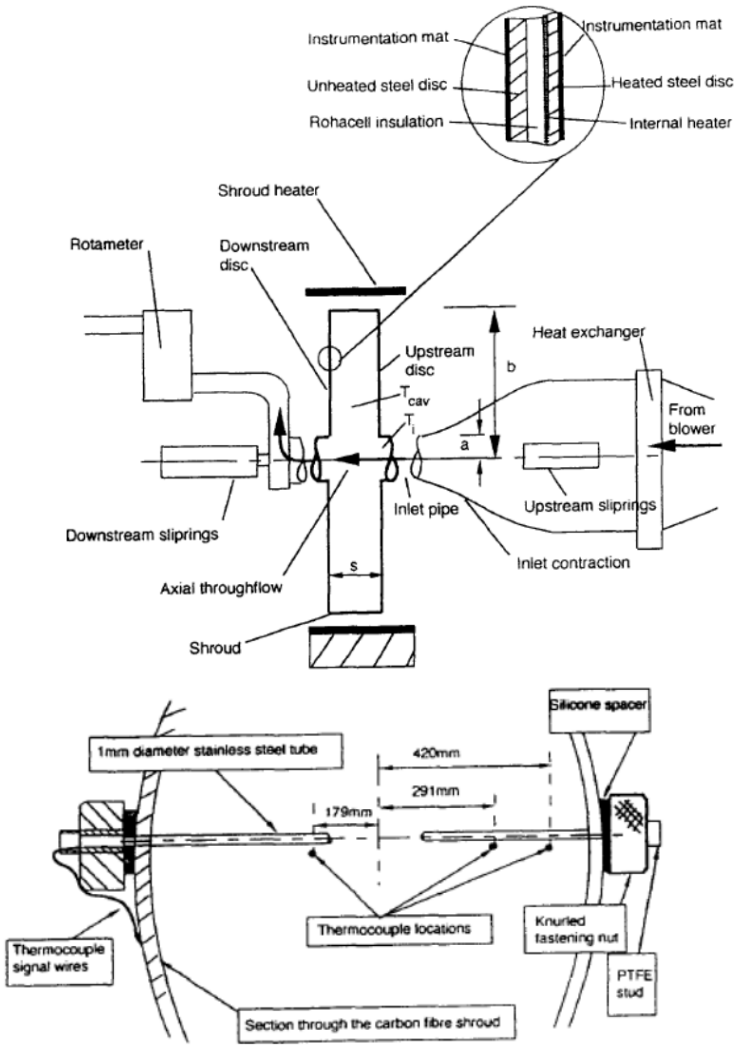

FIGURE 2.8: Schematic of the rotating test rig used in Long and Tucker (1994b): (a) r-z plane; (b) r-θ plane

location, the heat flux through the titanium shroud was determined using a 1D conduction solution and corrected for cavity radiative heat flux to calculate the shroud Nusselt number Nu_{sh}, such that:

$$\mathrm{Nu}_{sh} = \frac{q_{sh}\,(s/2)}{k_{air}\,(T_{sh} - T_{ref})} \tag{2.19}$$

and

$$\mathrm{Gr}_{sh} = \frac{\rho^2 \Omega^2 b}{\mu^2} \beta \Delta T \left(\frac{s}{2}\right)^3 \tag{2.20}$$

where the characteristic length is the shroud area over perimeter, s/2. The value of T_{ref} is based on the inlet air temperature such that;

$$T_{ref} = T_{in} + \frac{\Omega^2 \left(b^2 - a^2\right)}{2C_p} \tag{2.21}$$

where the fraction denotes an adiabatic temperature rise.

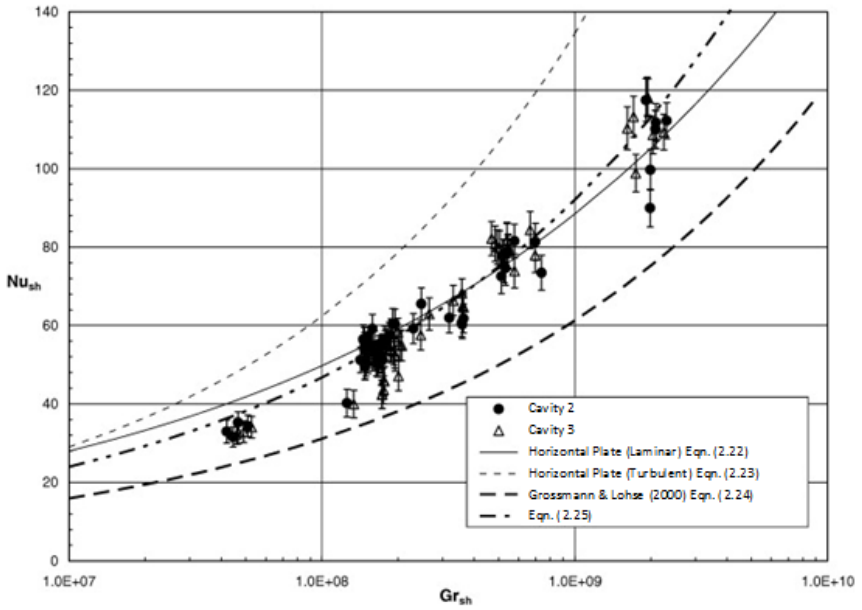

FIGURE 2.9: Variation of shroud Nusselt number with Grashof number from a rotating multiple cavity rig with axial throughflow with; $d_h/b = 0.164$, over the range $4.1 \times 10^4 < \mathrm{Re}_z < 2.0 \times 10^5$, $0.27 < \mathrm{Ro} < 5.8$, from Long and Childs (2007)

Figure 2.9 shows the variation of shroud Nusselt number Nu_{sh} with shroud Grashof number Gr_{sh} for cavities 2 and 3 with a $d_h/b = 0.164$. This shows a dependency of Nu_{sh} on Gr_{sh}. The error bars are derived using a Taylor series uncertainty propagation method and show approximately $\pm 5\%$. The accepted empirical correlations of laminar free convection and turbulent free convection from a horizontal plate (Lloyd and Moran, 1974) are also shown, such that:

$$\text{laminar:} \quad \mathrm{Nu}_{sh} = 0.54 \left(\mathrm{Gr}_{sh}\mathrm{Pr}\right)^{1/4} \tag{2.22}$$

$$\text{turbulent:} \quad \mathrm{Nu}_{sh} = 0.15 \left(\mathrm{Gr}_{sh}\mathrm{Pr}\right)^{1/3} \tag{2.23}$$

Recognising that the flow structure in rotating cavities might be described via a R-B convection mechanism, the authors suggested a modified form of the Grossmann and Lohse (2000) correlation (Equation 2.14) for air, based on the clearance ratio d_h/b, giving:

$$\mathrm{Nu}_{sh} = 0.25\,(\mathrm{Gr}_{sh}\mathrm{Pr})^{1/4} + 0.057\,(\mathrm{Gr}_{sh}\mathrm{Pr})^{1/3} \tag{2.24}$$

for $d_h/b = 0.164$ (shown in Figure 2.9 as Eqn. (20)) and for $d_h/b = 0.092$,

$$\mathrm{Nu}_{sh} = 0.216\,(\mathrm{Gr}_{sh}\mathrm{Pr})^{1/4} + 0.0494\,(\mathrm{Gr}_{sh}\mathrm{Pr})^{1/3} \tag{2.25}$$

Whilst there is no discernible difference between the cavities, the Nusselt numbers for $d_h/b = 0.164$ were much greater. This was attributed to the effect of the clearance ratio on the flow structure. It was also indicated (for $d_h/b = 0.092$) that there was no influence of axial Reynolds number on the shroud Nusselt number, suggesting that there was no impingement of the axial throughflow on the shroud surface.

2.3.3 Disc heat transfer for rotating cavities with axial throughflow

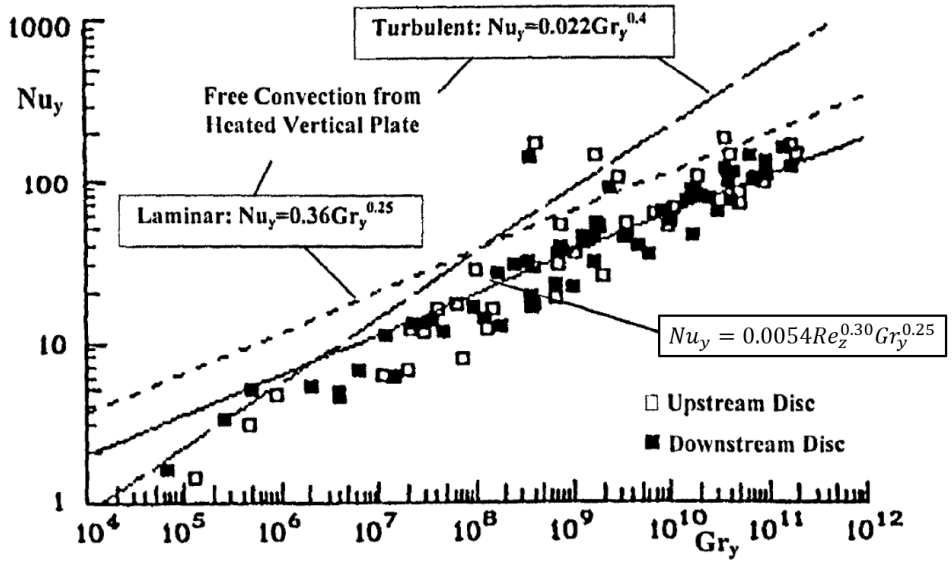

FIGURE 2.10: Variation of Nu_y with Gr_y for a symmetrically heated rotating cavity with an axial throughflow; $\mathrm{Re}_z = 2 \times 10^4$, (Farthing et al., 1992a)

Using two simple rotating-cavity rigs with axial throughflow ($a/b = 0.1$, $G = 0.138$) and with and without a central shaft ($d_h/b = 0.067$), Farthing et al. (1992a) measured the disc local Nusselt numbers using eight radially distributed fluxmeters on each disc over the range; $2 \times 10^4 \leq \mathrm{Re}_z \leq 1.6 \times 10^5$, $2 \times 10^5 \leq \mathrm{Re}_\theta \leq 5 \times 10^6$ and $0.25 \leq \beta\Delta T \leq 0.3$. Whilst the Nusselt numbers were not sensitive to G or the presence of a central shaft, the distribution did depend on the radial temperature profile of the discs. In the case of a symmetrically heated cavity with an increasing temperature profile, similar to in-engine conditions during normal operation, the authors used multiple regression analysis to produce a correlation, such that:

$$\mathrm{Nu}_y = 0.0054\mathrm{Re}_z^{0.30}\mathrm{Gr}_y^{0.25} \tag{2.26}$$

where;

$$\mathrm{Nu}_y = \frac{q_C y}{k_{air}\left(T - T_{in}\right)} \tag{2.27}$$

and

$$\mathrm{Gr}_y = \frac{\rho^2\Omega^2 r\beta\Delta T y^3}{\mu^2} \tag{2.28}$$

where $y = b - r$, q_C and T are the local surface heat flux and temperature respectively and T_{in} is the cavity inlet temperature measured from an upstream thermocouple. The modified characteristic length scale y is based on the distance from the shroud surface, given that the boundary layer is flowing radially inward in the Ekman layer from the shroud. Again the exponent of Gr_y suggests that the heat transfer is a result of rotationally induced laminar free convection. Figure 2.10 shows the variation of Nu_y with Gr_y for the symmetrically heated rotating cavity. The correlations for laminar and turbulent free convection are shown (Jaluria, 1980) alongside Equation 2.26. There was no indication of transition from laminar to turbulent free convection.

Burkhardt, Mayer, and Reile (1993) used the middle cavity of a five-cavity rig with a central shaft ($a/b \approx 0.286$, $G = 0.256$) to obtain local Nusselt numbers over the working range; $1.9 \times 10^6 \leq \mathrm{Re}_\theta \leq 5.6 \times 10^6$, $2.7 \times 10^4 \leq \mathrm{Re}_z \leq 9.5 \times 10^4$ and $0.08 \leq \beta\Delta T \leq 0.14$.

The upstream disc heat transfer was found to be greater than the downstream; increasing the axial throughflow increased the downstream heat transfer but reduced the upstream. The outer radius of the cavity showed good agreement for Nusselt numbers predicted by Equation 2.26.

Long (1994) used a simple rotating cavity without a central shaft ($a/b = 0.093$, $G = 0.13$ and $G = 0.36$) over the range; $0.2 \times 10^6 \leq \mathrm{Re}_\theta \leq 5 \times 10^6$, $2 \times 10^3 \leq \mathrm{Re}_z \leq 1.6 \times 10^5$ and $0.03 \leq \beta\Delta T \leq 0.3$. Using fluxmeters and thermocouples the disc heat transfer was determined for an increasing temperature distribution with either a heated or unheated shroud. Cavity air temperature was also measured. A heat balance, using the average disc heat transfer and cavity air temperature, was used to predict the fraction of axial throughflow entering the cavity. It was found that for Ro < 1 approximately 50% entered the cavity, reducing with increasing Ro. It should also be noted that a decrease in Ro below 1 eventually led to estimation of above 100% of axial throughflow entering the cavity, suggesting there was considerable uncertainty in the prediction. The heated shroud was not found to impact disc heat transfer.

Bohn et al. (2000) used the same rig previously used for flow visualisation to measure disc heat transfer; $a/b = 0.3$, $G = 0.2$, $d_h/b = 0.15$. Six test cases were explored across the range of nondimensional parameters listed in Table 2.1. Their definition of Grashof number was:

$$\mathrm{Gr}' = \mathrm{Re}_\theta^2 \beta\Delta T \tag{2.29}$$

Case	**1**	**2**	**3**	**4**	**5**	**6**
Ro	0.28	0.28	0.56	1.1	0.56	0.97
$\mathrm{Re}_\theta/10^5$	8.0	8.0	4.0	2.0	8.0	8.0
$\mathrm{Re}_z/10^4$	2.0	2.0	2.0	2.0	4.0	7.0
$\beta\Delta T$	0.27	0.27	0.27	0.27	0.27	0.27
$\mathrm{Gr}/10^{11}$	1.7	1.7	0.43	0.11	1.7	1.7

TABLE 2.1: Nondimensional parameter of Bohn et al. (2000)

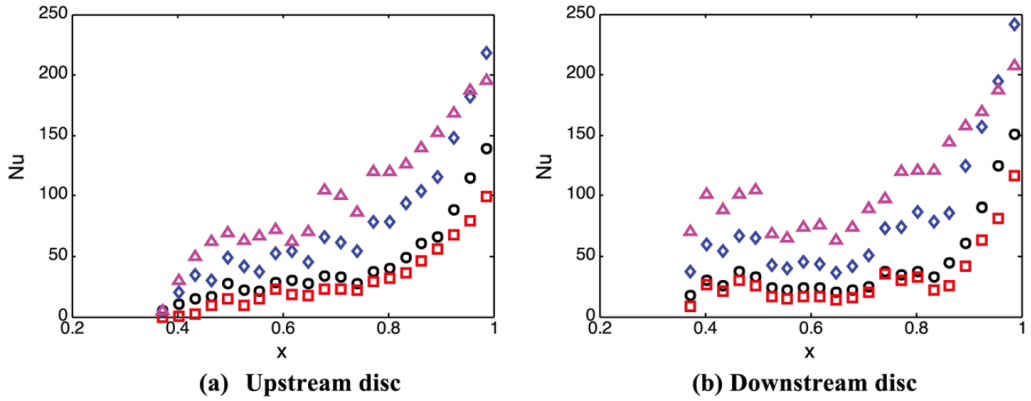

FIGURE 2.11: Nusselt number distribution for (a) upstream and (b) downstream discs (Bohn et al., 2000): ○, case 3; □, case 4; ◇, case 5; △, case 6

Using a quasi-linear increasing temperature profile and unheated shroud, the measured Nusselt numbers for all six test cases were found to be consistent with the empirical correlations of Kantha (1987). Figure 2.11 shows that for test cases 3-6 the Nusselt numbers increase radially and that in each case the maximum value of Nu increases with Gr′. It is also noted that the local values of Nu tend to be higher on the downstream disc, particularly towards lower values of x, suggesting that impingement of axial throughflow is likely the cause. In all cases shown the local Nu tends to a minimum in the vicinity of $x \approx 0.6$ before increasing with decreasing radius. There is a significant increase in Nu towards $x = 1$.

Owen and Powell (2004) used the same rig as for their LDA experiments to measure the Nusselt numbers on the downstream disc for $0.05 \leq \text{Ro} \leq 14$. At low Ro, the radially increasing Nusselt numbers were consistent with buoyancy-induced flow. At large values of Re_z (high Ro) the throughflow dominated over the buoyancy effects.

Günther, Uffrecht, and Odenbach (2012) used a two cavity rotating rig (shown in Figure 2.12) with a central shaft ($a/b = 0.21$, $G \approx 0.31$, $d_h/b = 0.062$) to measure the central disc temperatures (shown as dark green in Figure 2.12) and calculate the axial heat flux. The tests covered parameters: Re_θ up to 10^7 and Re_z up to 2×10^5. The shroud was heated. A 2D finite element model of the central disc with applied surface temperature boundary conditions (smoothed via a spline and then a fourth-order polynomial) was used to derive the axial heat fluxes.

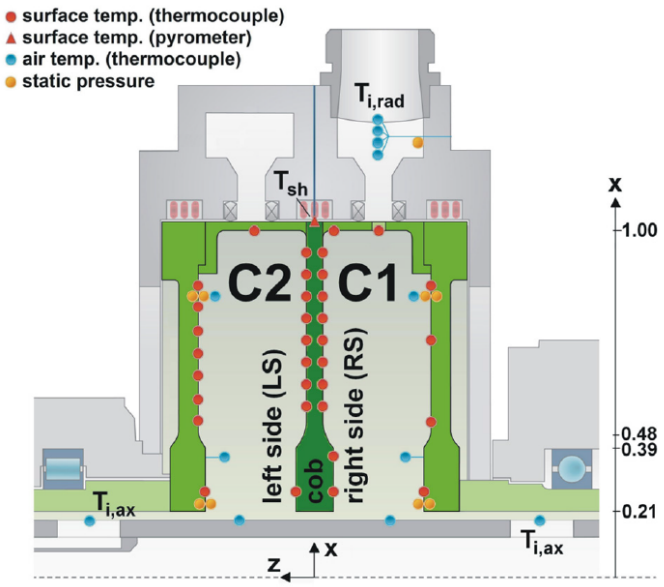

FIGURE 2.12: Schematic of rotating cavity rig used by Günther, Uffrecht, and Odenbach (2012), note the same rig was also used for radial-inflow experiments

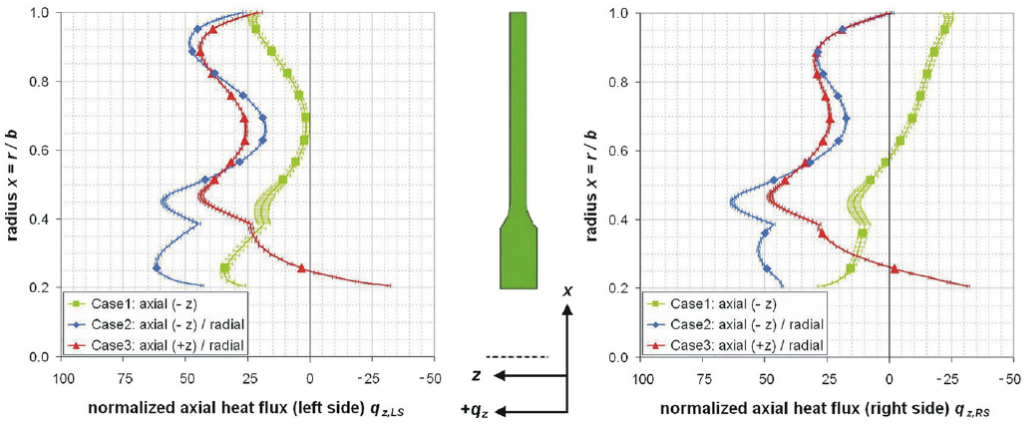

FIGURE 2.13: Axial heat flux across central disc of the Günther, Uffrecht, and Odenbach (2012) rotating cavity rig. Upstream (a) and downstream (b) disc surfaces for three flow regimes, Case 1 is an axial throughflow at conditions; $\mathrm{Re}_\theta = 5.8 \times 10^6$ and $\mathrm{Re}_z = 9.0 \times 10^4$

Figure 2.13 shows the radial distribution of normalized axial heat flux for three test cases (only case 1 corresponds to axial throughflow). These show that for the left side of the disc (upstream side) heat is transferred out of the disc into the cavity air at all radial locations, notably there is a local minimum at $x \approx 0.6$ as can be interpreted in Figure 2.11(b). For $x < 0.6$ heat is conducted from the right side to the left, indicated by negative

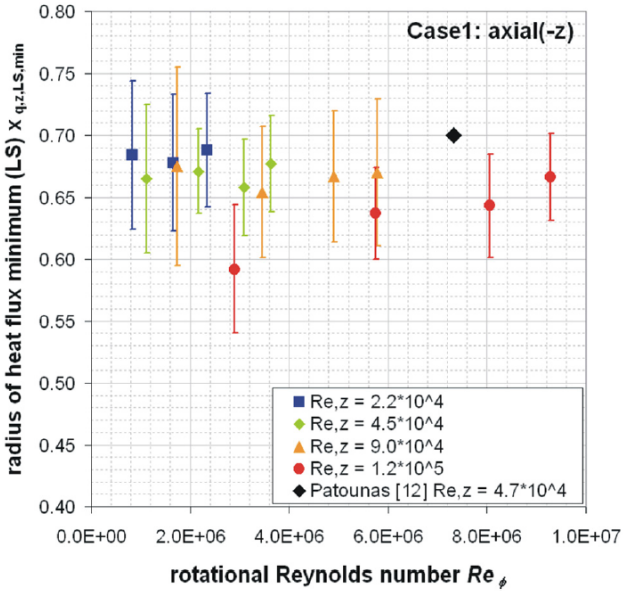

FIGURE 2.14: Location of heat flux minimum on downstream disc surface for the axial throughflow case, from Günther, Uffrecht, and Odenbach (2012) rotating rig

heat flux, for $x > 0.6$ heat flux is positive on both sides suggesting buoyancy-induced flow. Figure 2.14 shows the location of the minimum heat flux on the upstream side of the central disc across a range of tested Re_θ, this shows that the minimum is in the range $0.59 \leq x \leq 0.69$ (omitting uncertainty bars), suggesting that there is an interplay between the outer radius buoyancy-induced flow and inner radius axial throughflow dominated region. There is no clear relationship between the minimum location and the tested nondimensional parameters.

Günther, Uffrecht, and Odenbach (2014) used the same rig as Günther, Uffrecht, and Odenbach (2012). Using air thermocouple measurements taken from two radial locations inside the cavities, a heat balance was performed to estimate the percentage of axial throughflow entering the cavity (similar to Long (1994)). Again it was found that the percentage of ingested throughflow increased with decreasing Rossby number.

Atkins and Kanjirakkad (2014) used a rebuild of the MCR rig used by Long, Miche, and Childs (2007), with $a/b = 0.318$, $G = 0.195$ and $d_h/b = 0.164$. Nineteen test cases were presented giving nondimensional radial temperature profiles for the range of working conditions: $2 \times 10^4 \leq \mathrm{Re}_z \leq 1.1 \times 10^5$, $0.3 \leq \mathrm{Ro} \leq 5$ and $0.05 \leq \beta\Delta T \leq 0.32$. The

nondimensional temperature was defined as in Equation 2.8. These results were used to investigate the flow field using CFD (discussed in section 2.4).

Tang, Shardlow, and Owen (2015) used the nineteen test cases of Atkins and Kanjirakkad (2014) to derive the disc local Nusselt numbers using Bayesian statistics. By assuming that the rotor discs can be modelled using the fin equation, the Bayesian method can be used to determine the Biot numbers and by extension the disc Nusselt numbers. The authors demonstrated a radially increasing Nu profile with a maximum at $x = 1$ and in most cases tending to a minimum value below $x < 0.6$.

Tang (2017) used a laminar theoretical model of buoyancy-induced flow and the general fin equation - developed from Owen and Tang (2015) - to predict the Nusselt number and temperatures of rotating discs along with the shroud and cob to calculate the axial throughflow temperature rise. The shroud heat transfer used a correlation of laminar free convection from a horizontal plate, modified for a rotating surface and the cobs an optimized forced convection correlation. The model was used to predict the axial throughflow temperature rise and when compared to measurements taken from the Phase A test programme of this thesis, showed good agreement. These results are also presented in Tang, Puttock-Brown, and Owen (2017) and show that the average contribution of shroud, both disc surfaces and cobs to the temperature rise was predicted to be approximately 62%, 37% and 1%, indicating that the shroud is the predominant contributor in the heat transfer system despite its lower surface area.

2.4 Computational Fluid Dynamics Simulation

With the growth in computational power and reduction in the associated cost, numerical simulation of rotating cavities has become increasingly prevalent. Initially solving the Reynolds-averaged Navier-Stokes (RANS) equations on 2D axisymmetric domains, 3D unsteady computation is now readily accessible. Whilst the use of CFD has grown for the investigation of the flow structure in rotating cavities, its use as a practical day-to-day design tool for gas turbines is still limited, due in part to the significant differences

in timescales between the flow structure and engine thermal transients.

Using a simple rotating cavity rig similar to that of Farthing et al. (1992b); Long and Tucker (1994a) and Tucker (1993) used 3D unsteady laminar CFD on modest working conditions; $\mathrm{Re}_z = 2180$ and $\mathrm{Re}_\theta = 1.3 \times 10^4$ for four different radial temperature profiles. They found that the flow structure formed and would vacillate between either one or two radial arms with cyclonic and anti-cyclonic circulations, in keeping with the observations of Farthing et al. (1992b). It was also noted that the maximum number of circulation pairs (and radial arms) increased as the maximum disc temperature moved radially outward. Tucker (2002) also showed good qualitative agreement to the observations of Farthing et al. (1992b) regarding the formation of the circulation pair through the bifurcation of the radial arm. It was also concluded that the highest unsteadiness was in the area of high tangential velocity gradients yet axial flow unsteadiness was found to be relatively small. Long, Morse, and Tucker (1997) used 3D unsteady CFD with a mixing-length turbulence model based on the rig of Long (1994). The trend of Nusselt number distribution was predicted but the magnitude was underpredicted.

Sun et al. (2004) used 3D laminar unsteady CFD on the closed rotating cavity of Bohn et al. (1995). Good agreement was found between the calculated shroud Nusselt numbers and the correlation presented in Equation 2.16(b).

Tian et al. (2004) used a simple rotating cavity with axial throughflow of cooling air using 3D steady model with a low Reynolds k-ϵ turbulence model. A separation in the cavity flow structure was observed; at high radius there was buoyancy-induced flow, forming R-B type convection and a forced convection zone at lower radius, the toroidal vortex. Sun et al. (2007) compared RNG k-ϵ turbulence model and Large Eddy Simulation (LES) computations using the measurements of Long, Alexiou, and Smout (2003) and Alexiou (2000). It was found that LES predicted the Nusselt numbers (on the shroud) well whilst the RANS model underpredicted them. The unsteadiness of the LES was also significantly higher. Comparison of the ratio of relative tangential velocity to disc speed, with a core flow rotating slower than the discs, again showed LES out-performed the RANS simulation, though there was good agreement with RANS at the outer radii.

Owen, Abrahamsson, and Linblad (2007) used 3D unsteady CFD with RANS k-ϵ turbulence modelling to compare with the experimental results of Owen and Powell (2004) for three cases, two of which are shown in Figure 2.15 for the mid-axial plane where for Exp 2, $\mathrm{Re}_\theta = 0.43 \times 10^6$, $\mathrm{Re}_z = 0.303 \times 10^4$ and Ro = 0.674 and for Exp 5, $\mathrm{Re}_\theta = 1.57 \times 10^6$, $\mathrm{Re}_z = 0.164 \times 10^4$ and Ro = 0.100, Ra was not reported. In both cases the cooling axial throughflow enters the cavity in radial arms and bifurcates into cyclonic and anti-cyclonic cells of low and high-pressure respectively. Whilst there is a clear two cell structure in Figure 2.15(a) the situation is more complex in (b). Several radial arms have formed and unlike (a) there is no thin layer of cold air adjacent to the unheated shroud, rather the radial arms appeared to have been deflected by a layer of hot gas.

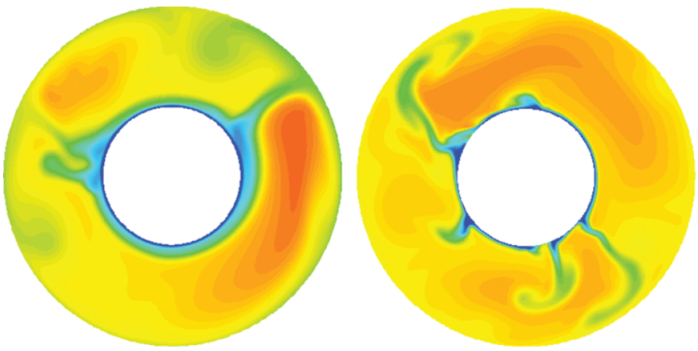

FIGURE 2.15: Temperature contours from mid-axial plane for heated clockwise rotating cavity (shroud unheated) from Owen, Abrahamsson, and Linblad (2007): (a) Exp 2 and (b) Exp 5

Dweik et al. (2009) used unsteady 3D RANS simulation with the SST k-ω turbulence model to investigate the temporal behaviour of a developing rotating cavity flow structure from a steady state for three engine representative running conditions. Initial validation used the results and rig of Owen and Powell (2004) and showed very good agreement to measured disc Nusselt numbers. Their computations show the development of radial arms that propagate radially outward, bifurcate and form opposing circulation cells which in turn vacillate. Whilst not discussed directly, instantaneous temperature difference $(T - T_{in})$ contours indicate not only the radial arms but also hot gas leaving the shroud and travelling radially inward through the core region where the circulation cells

meet, as shown in Figure 2.16. Here the numbers indicate simulation time in milliseconds; the saturated red zones indicate a +50 K temperature difference and the working conditions are; $\mathrm{Re}_\theta = 2.4 \times 10^6$, $\mathrm{Re}_z = 1.4 \times 10^4$, Ro$= 0.053$ and Ra$= 5.3 \times 10^{10}$.

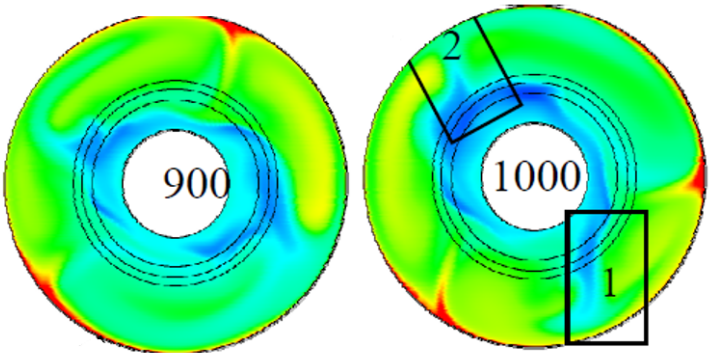

FIGURE 2.16: Instantaneous temperature difference contours for rotating cavity, L2 Idle case, from Dweik et al. (2009): (a) Flow at 900 ms and (b) Flow at 1000 ms

Tan, Ren, and Jiang (2009) used 3D steady RANS, unsteady RANS (URANS) and LES on three cases presented by Bohn et al. (2000) (Ro$= 3.7$ and Ra$= 8.2 \times 10^9$). Comparison was made to experimental results and it was found that both URANS and LES produced similar large-scale structures (circulation cells) and reasonable agreement to heat transfer measurements. Steady RANS failed to capture the flow structure but gave acceptable heat transfer predictions. LES predictions took x28 longer to compute than URANS. Tan, Ren, and Jiang (2014) later repeated a single calculation case using a discontinuous Galerkin method and a transition model. This increased the accuracy of the predicted results.

Atkins and Kanjirakkad (2014) used a hybrid RANS/LES method for two of their presented experimental cases; $\mathrm{Re}_\theta = 3.1 \times 10^6$, $\mathrm{Re}_z = 1.1 \times 10^5$, $\beta\Delta T = 0.15$ and 0.32 giving Ra$= 10^{12}$ and Ra$= 2.2 \times 10^{12}$ respectively. Figure 2.17 shows mid-axial plane contours of density for the two cases; by increasing $\beta\Delta T$ the flow has turned from a relatively stable and stratified regime to an unstable R-B convection type flow with enhanced mixing in the cavity. Whilst the radial arms are difficult to determine (located at seven and eleven o'clock) there is again an indication of hot gas departing from the shroud surface and traveling radially inwards, seen by the lower density regions breaking up the higher

regions in the shroud area close to the previously indicated radial arms. The finer detail of the cavity flow structure predictions should also be noted compared to previous illustrations.

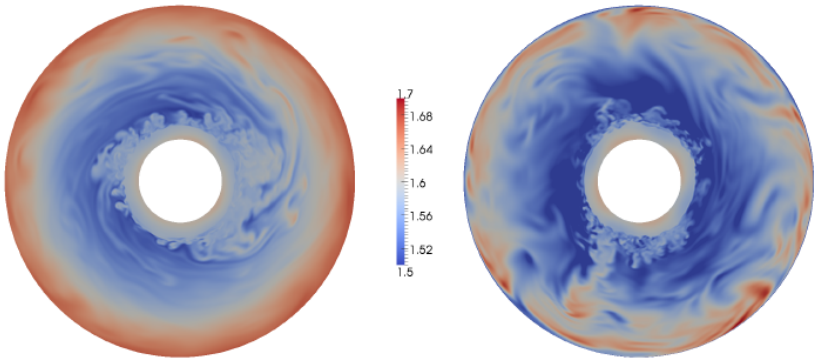

FIGURE 2.17: Instantaneous density contours for mid-axial plane of rotating cavity at $\mathrm{Re}_\theta = 3.1 \times 10^6$, $\mathrm{Re}_z = 1.1 \times 10^5$, from Atkins and Kanjirakkad (2014): (a) $\beta\Delta T = 0.15$ and (b) $\beta\Delta T = 0.32$

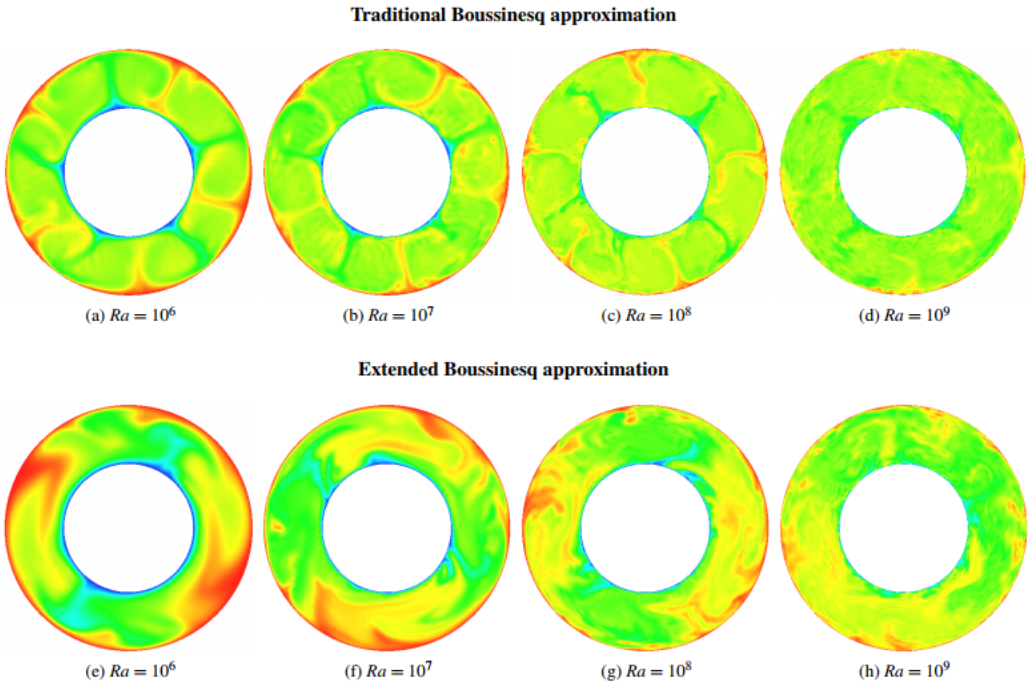

FIGURE 2.18: Instantaneous temperature contours for a sealed rotating cavity across the interval $T_C \leq T \leq T_H$, from Pitz et al. (2017)

Pitz et al. (2017) used Direct Numerical Simulation (DNS) and spectral element-Fourier analysis to investigate buoyancy-induced flow in a sealed rotating cavity with the traditional and an extended Boussinesq approximation proposed by Lopez, Marques, and

Avila (2013). It was found that the traditional Boussinesq approximation significantly over-predicted shroud Nusselt numbers reported by Bohn et al. (1995). The extended approximation gave close agreement to the proposed correlations in Equation 2.16, indicating that the buoyancy effects due to non-linear terms in the momentum equation are key to accurate prediction of flow structure and heat transfer. Figure 2.18 shows a comparison of instantaneous temperature contours for $T_C \leq T \leq T_H$ across a range of Rayleigh numbers in the mid-axial plane, whilst the traditional Boussinesq shows the familiar series of counter-rotating cells consistent with R-B convection the extended approximation shows a much more de-stabilised flow field with much less uniform temperature.

2.4.1 Summary of Literature Review

The rotating cavities relevant to this work can be categorised into isothermal and non-isothermal, sealed and unsealed. For a sealed heated cavity the flow develops into a series of coherent structures referred to as Rayleigh-Bénard convection. This convection mode has been observed, at sufficiently high Rayleigh number, to transition from a laminar bulk and boundary layer state to a turbulent bulk and boundary layer state. Between these exist a region where the bulk convection is itself turbulent, but the boundary layers remain laminar. The different regimes being determined by the exponent of the correlated Rayleigh to Nusselt number. The state of the shroud boundary layer is thought to remain laminar, the effects of the centrifugal force acting to suppress transition, however experiments has yet to reach the Rayleigh number (Ra > 10^{13}) at which transition is thought to occur. In the case of the unsealed cavity the axial throughflow is thought not to penetrate the shroud boundary layer as there is no evidence of a dependency on the shroud Nusselt number on the axial Reynolds number.

In the case of unsealed heated cavities with a radially increasing temperature distribution an unsteady and unstable three-dimensional flow develops, pairs of cyclonic and anti-cyclonic circulations form due to the rotationally-induced buoyancy forces. Flow visualisation has qualitatively observed axial throughflow entering the cavity through a radial outward plume that bifurcates into the two circulations zones. Where these two

circulations meet no smoke was seen to enter in the core region and so this was termed the dead zone. Despite this early work laying the foundations for the understanding of the cavity flow structure there has been little advancement. This region between the circulation zones has received little attention, and whilst there has been a focus on how flow enters the cavity the mechanisms for its departure remain elusive. Some observation of radial inflow in the Ekman layers has been made but in an experimental rig that does not accurately reflect the engine, either in materials or nondimensional parameter. There is some tentative evidence of a radial inflow structure in the core through later flow visualisation and numerical results that would suggest a fast-moving jet like structure, however this has not been discussed in depth.

There have been no recent experimental investigations into the state of the disc boundary layers in terms of flow direction, in part due to the difficulties of near wall non-invasive techniques such as LDA. The experimental evidence for flow structure and heat transfer on the rotating cavity disc wall has primarily been through thermocouples or fluxmeters. In either case the density of instrumentation has been sparse and remained at a low acquisition frequency. Time resolved experimental results are not reported despite being of importance for numerical validation. In-cavity air temperatures have also received little attention; it is acknowledged that intrusive instrumentation would disrupt the flow field however as the cavity flow exhibits a near solid-body rotation the effect of any rotor mounted instrumentation would be reduced due to lower relative velocities.

The primary focus of research to date has been in the understanding of the macroscopic properties of the cavity system, the interplay between the flow field and wall heat transfer. This approach has been vital in the development of thermo-mechanical simulations of secondary air systems, as these typically rely on scaling laws and correlations to predict the temperature distribution, and consequently HP compressor tip clearances. The differences between time-scales of the engine thermal transients and the unsteady flow structure are still impractical to allow the use of time-resolved CFD in design iterations. However, computer power is set to increase and so CFD usage in the design cycle is near, this requires a better fundamental understanding of the cavity flow structure.

3 Experimental Apparatus

The original experimental data reported in this thesis are taken from the fifth and sixth builds of the Multiple Cavity Rig (MCR), referred to in later sections as Phase A and Phase B respectively. The MCR simulates the secondary air system of an aero engine HP compressor, allowing investigation of the convective heat transfer and flow structures present in this system. Previous experiments performed on the MCR relevant to this thesis are indicated in Chapter 2.

3.1 General Description

A general assembly drawing of the rig is shown in Figure 3.1. The rotating assembly or rotor (Figure 3.1 I) is scaled down from a Rolls Royce Trent aero engine HP compressor, at a 0.7:1 ratio. Five Titanium-318 discs form four cylindrical cavities, all having an outer rim diameter $D = 491.3$ mm. The first three cavities (in the direction of flow) are identical with a disc spacing $s = 42.9$ mm and a shroud radius $b = 220$ mm, giving a gap ratio $G = 0.195$. The inner radius a = 70.1 mm, $a/b = 0.318$.

The axial throughflow air is supplied via two Ø30 mm pipes (Figure 3.1 P) which feed into an annular plenum in the circumferential direction, transferring radially inwards through twelve Ø24 mm holes (Figure 3.1 Q) through the inner radius of the plenum and the outer radius of the shaft assembly mount. The air is turned 90^{o} to the axial direction and flows down an annular duct (Figure 3.1 N) formed by the shaft outer radius and rotor stub-shaft. There is a convergence in the duct to form an annular space equal to that formed in rotor test section. Finally there are six 10 mm wide rectangular blocks (Figure 3.1 K) bolted to the rotor stub-shaft forming a similar flow restriction to the circumferential array of six Ø25 mm holes in the rotor endplate (Figure 3.1 F), where the flow exits

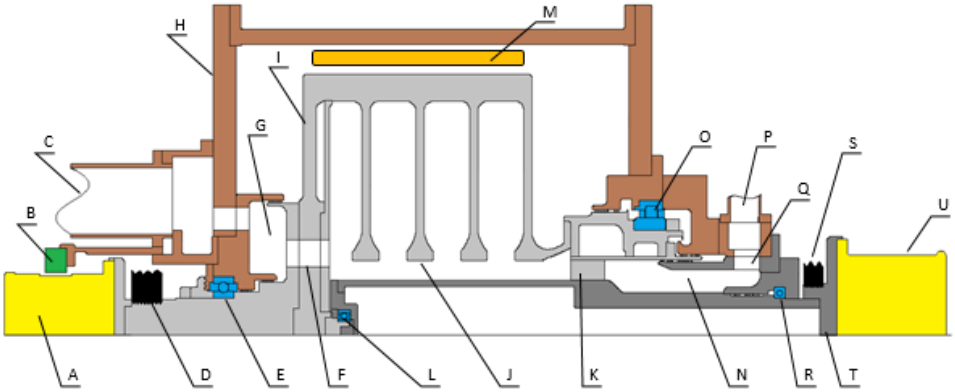

FIGURE 3.1: General layout of the Multiple Cavity Rig, taken from Puttock et al. (2017)

A	Rotor telemetry unit
B	Rotor telemetry antenna
C	Rig exhaust
D	Rotor pulley belt
E	Grease-pack rotor bearing
F	Bore flow exit holes
G	Exit cavity
H	Outer drum
I	Rotating assembly
J	Central rotor disc
K	Bore inlet flow restriction
L	Shaft location bearing
M	Radiative heater
N	Inlet cavity
O	Axial oil fed roller bearing
P	Bore flow inlet
Q	Radial transfer holes
R	Inter-shaft bearing
S	Shaft pulley
T	Central shaft
U	Shaft telemetry unit

TABLE 3.1: Key to Figure 3.1

the test section.

The rotor assembly is driven by a 22kW AC motor with an additional resistor bank. The motor controller allows precise control over the rotor speed, acceleration and deceleration. The tensioned drive pulley (Figure 3.1 D) is mounted on the rotor stub shaft, allowing a maximum rotational speed of 8000 rpm.

In addition to the new - updated from Atkins and Kanjirakkad (2014) - flow inlet path, test Phases A and B feature a driven central shaft manufactured from Mild Steel (Figure 3.1 T) with an outer radius $r_s = 52$ mm, giving $d_h/b = 0.165$. The shaft can be rotated co- and counter-clockwise up to 8000 rpm and is driven by a 3kW AC motor via a pulley belt

(Figure 3.1 S).

The rotor and shaft are housed inside a steel plate outer drum (Figure 3.1 H) formed of two endplates (OD Ø622 mm) and a hollow cylindrical central spacer (15 mm thick). The downstream endplate features eight exit air holes (Ø20 mm), whilst the upstream now incorporates a new axial roller bearing and rotor stub-shaft, to facilitate the new central shaft. The casing also includes the necessary bearing chambers, air plenums, water cooling and mounting points for the ancillary systems.

The rotor is supported by the outer drum via two high precision bearings. The downstream bearing (Figure 3.1 E) is a grease lubricated ball bearing and locates the downstream stub-shaft. Upstream is an oil-fed axial-roller bearing (Figure 3.1 D) - from a Rolls Royce IP turbine - mounted on the casing endplate. The bearing inner race is secured to the stub-shaft bolted to the rotor. This arrangement allows for thermal expansion and gives access to the rotor assembly.

The oil lubrication required for the axial-roller bearing is supplied by a feed pump and a separate scavenge pump. An inclined deaerator tray is used to return the scavenged oil to the feed pump. The oil is passed though a heat exchanger with the cold side supplied by the cooling water exiting the rig. The oil is sprayed into the bearing chamber via a series of nozzles. The chamber itself is pressurised via labyrinth seals to ensure minimal leakage. The balance cavities are fed from the auxiliary air supply. With cold build clearances of order 0.1 mm the system can achieve flow side pressure differentials of ± 10 mbar, ensuring negligible leakage paths.

For the central shaft a similar arrangement of bearings are used. The downstream end (Figure 3.1 L) is a grease lubricated ball bearing, the seat of which is bolted to the rotor end disc. The upstream end (Figure 3.1 R) uses a grease lubricated ball bearing with the outer race indirectly bolted to the outer casing and the inner race to the rotating shaft. An inner balance cavity is used with a labyrinth seal arrangement to ensure negligible leakage.

3.1.1 Throughflow Air Supply

The throughflow air is supplied to the rig from a two stage, screw type, Atlas Copco ZT250 compressor. This is immediately ducted to an Atlas Copco air dryer removing any moisture from the air. The mass flow rate is measured using an calibrated Venturi. A butterfly valve located downstream of the rig exhaust is used to pressurise the rig, allowing the pressure-balanced labyrinth seals to function effectively and reducing leakage to a negligible level. The labyrinth seals specifications are given by Alexiou (2000).

3.1.2 Rig Heating System

The heating effect of main flow path HP compressor air is simulated using a circumferential array of radiant heaters located on the outer drum (Figure 3.1 M). Each heater is insulated from the outer drum to reduce heating losses. Two heat shields are installed on either side of the rotor to avoid overheating the casing end-plates and bearings. This system is capable of delivering a rotor outer temperature in excess of 250°C, however it was found to lead to increased failure of thermocouple during testing so a limit of 230°C is set.

3.2 Instrumentation and Data Acquisition

3.2.1 Ancillary Systems

The throughflow mass flow rate is measured upstream of the rig using an on-site developed and calibrated Venturi section. A differential pressure measurement is taken upstream and downstream of the Venturi section along with a temperature. No measurement is made of the rig exit flow, given the pressure balanced labyrinth seals the leakage is expected to be negligible.

The rotational speed of the rotor assembly and shaft are measured using magnetic pickup probes, outputting an analogue voltage. Software is used to analyse the frequency and convert into an rpm for rig monitoring and recording.

In tests where the central shaft is stationary a series of nine static pressure tappings are measured in the axial direction. These are read by a 16-channel Scanivalve Digital Sensor Array (DSA) 3217.

In Phase B a new low-frequency vibration sensor was installed for monitoring purposes by the author. This used a ADXL345 three-axis accelerometer communicating with an Arduino Uno development board and proved an effective low-cost vibration monitoring system. For the final experiments an analogue voltage output from the accelerometer was measured. This allowed an increase in the frequency response from 70 to 500Hz.

3.2.2 Temperature Measurements - Phase A

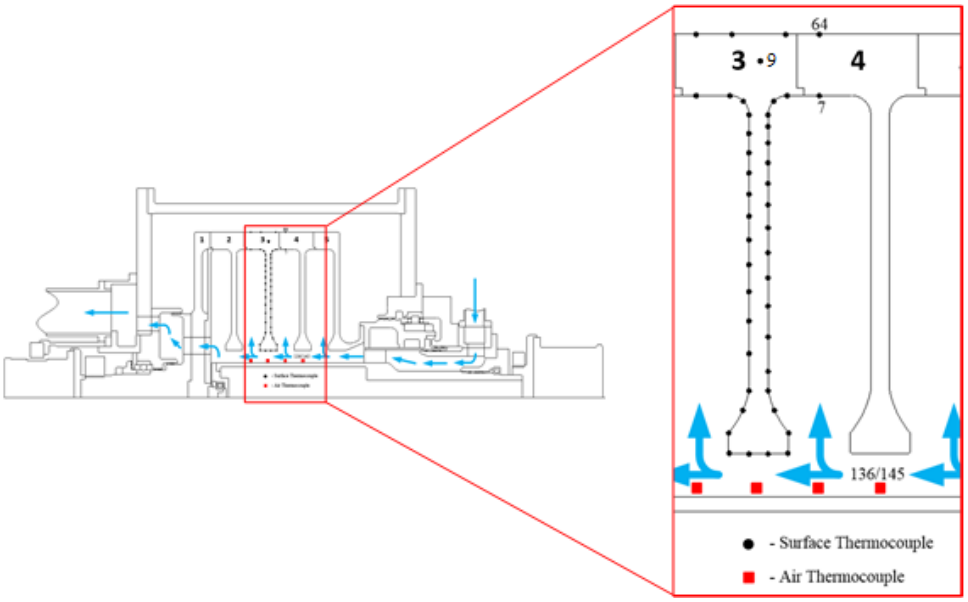

FIGURE 3.2: Phase A thermocouple locations. Specifically referenced locations are numbered. Red squares indicate shaft mounted air thermocouples. Flow from right to left.

The rotating frame temperatures are measured using glass fibre insulated K-type thermocouples with a wire diameter of 0.25 mm and a welded bead nominal diameter of of 0.4 mm. The installation method for the disc thermocouples is described by Atkins and Kanjirakkad (2014). The thermal disturbance errors due to the embedding process has been studied (using 1D models) and found to give errors of the order 0.1 K (Alexiou, 2000).

The data acquisition chain is essentially the same as that described by Atkins (2013) and is repeated here for convenience. The calibration procedure chain including thermocouples, cold junction references, amplifiers and acquisition cards has been calibrated against a national-laboratory-standard reference system. This gives a comparison uncertainty of 20mK, an order of magnitude lower than the thermocouple uncertainty. The typical single point uncertainties of the thermocouples and cold junctions are in the region of 0.1 K.

The same measurement chain as the Sussex Turbine Stator Well (TSW) rig is used (Coren et al., 2012). A Datatel non-contact radio telemetry system to measure the rotating frame thermocouples (Figure 3.1 A) is used and supports 82 channels. The system comprises six individual modules connected in a parallel bus. Each module uses a dedicated Platinum Resistance Thermometer (PRT) for the cold junction reference.

Previous testing with this data acquisition chain has shown that the associated errors cannot be considered normal in distribution so there is no reduction in the uncertainty through averaging. In this thesis the measurement frequency of the rotating thermocouples is 3 Hz, this is hardware selected and corresponding the average of 8 samples taken by the rotating telemetry unit. The total worst case uncertainty is approximately $\pm$0.5 K as the errors are simply added, this is consistent with test data from the TSW rig which showed a realistic bias uncertainty of the same magnitude when using the same measurement chain.

The shaft features 36 air and metal thermocouples arrayed in four circumferential locations spaced 90° apart with the thermocouples at nine axial locations (Figure 3.2). Again, 0.25 mm wire diameter K-Type thermocouples with glass fibre insulation are used. The metal thermocouples were installed as in the rotor. Air thermocouples are positioned at $x = 0.25$ and due to the low radius and direction of centrifugal force they do not require support. This has the advantage of removing a conduction path to the bead from the metal surface through a support tube. Continual monitoring throughout testing showed they did not come into contact with the shaft surface. The shaft thermocouples are able under certain circumstances to detect the unsteady thermal wakes of the upstream blocks

(Figure 3.1 K), as detailed in Puttock and Rose (2016). All the instrumentation wires are routed along the inner shaft radius towards a secondary Datatel radio telemetry system, Figure 3.1 U. Similar PRT cold junction reference as described above are used, giving the same error bias in the acquisition chain.

Phase A rotating thermocouple locations on rotor disc three are detailed in Figure 3.2, with referred thermocouple locations numbered.

Stationary frame temperatures are measured using K-Type thermocouples connected to an Agilent 34970A located in a temperature controlled instrumentation cupboard. The cold junction reference is taken from the onboard PRT and the sample to sample noise reduced by cycle averaging, outputting at approximately 1 Hz.

3.2.3 Temperature Measurements - Phase B

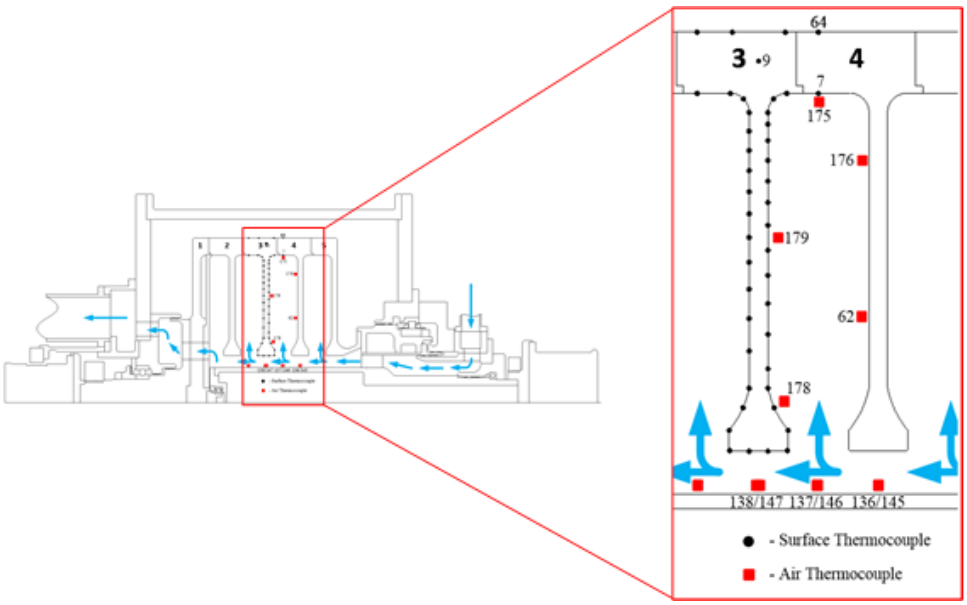

FIGURE 3.3: Phase B thermocouple locations. Red squares in bore region indicate shaft mounted air thermocouples. Specifically referenced locations are numbered. Flow from right to left.

Between Phases A and B the instrumentation density on a new disc four was increased at the authors recommendation with all installation carried out by the author. This mirrored the radial surface thermocouple locations present on disc three (Figure 3.2) however they have not been used in the work presented here. Whilst the installation

method is essentially the same, a new approach was taken with regard to the lead out channels to the rotor periphery. To reduce the aerodynamic and thermal disturbance of the thermocouples present on the downstream face of disc four all thermocouple wires are routed for ten wire diameters circumferentially and through a 1 mm hole to the upstream face. From here the wires are routed in channels to the eight lead-out holes in the rotor periphery.

Additionally, seven air thermocouples (of which only five are used in this thesis) are installed - by the author - in the cavity formed by discs three and four. These protrude 4 mm into the cavity and are unsupported as with previous builds. Inspection (using a borescope) during the test program and monitoring of the signals indicated that the centrifugal forces did not collapse them on the disc surface. All new thermocouples installed are calibrated to their respective telemetry data channels. The thermocouple locations of interest are indicated in Figure 3.3 with non-dimensional radial locations of air thermocouples given in Table 3.2.

Thermocouple	$x = r/b$
62	0.5798
175	0.982
176	0.873
178	0.406
179	0.736

TABLE 3.2: Nondimensional radial positions of cavity air thermocouples in Figure 3.3

3.2.4 Unsteady Pressure Measurements

For the final test described in Chapter 5 the shaft was modified to mount five sub-miniature unsteady pressure transducers. Two types of Kulite^{TM} transducers were used, two XCE-093 absolute measurement with 25 psi range. The other three XCQ-77-062 gauge measurement with a 5 psi range. To ensure non-fluctuating back-pressure these are connected, through a mutual manifold, to an exterior reference chamber. The chamber pressure is logged via the Scanivalve DSA. The installation locations are given in Table 3.3.

Transducer	Axial location	Circumferential location (°)
1	Disc five mid-plane	0
2	Cavity 4-5 mid-plane	0
3	Cavity 4-5 mid-plane	20
4	Cavity 3-4 mid-plane	0
5	Cavity 3-4 mid-plane	20

TABLE 3.3: Locations of high frequency pressure transducers

The measurement of the transducers is performed by a National Instruments NI PXIe-4331 8-channel, 24-bit simultaneous acquisition card operating at 100 kHz. This card provides the excitation voltage for the Wheatstone bridge and gives a ratiometric output. Scaling information is provided using the calibration certificates. Anti-aliasing is performed onboard and given the Nyquist criterion frequency, information up to approximately 46 kHz is recorded. With a rig rotational speed of 8000 rpm (133 Hz) this gives a data point for approximately each degree of rotation. The data acquisition and control system was up updated accordingly.

3.2.5 Data Acquisition & Control

The management system for Phase A was controlled from two rig monitoring PCs running National Instruments LabVIEW software, communicating with a cRio-9022 and a PXIe-1073. All thermocouple data is routed to the PXIe, along with static pressure and rotational speed sensors, forming the acquisition side. The cDAQ unit is connected to the heater array, exit valve and proportional balancing valves and allows remote operation of these systems, forming the control aspect of the system.

For Phase B the entire system was integrated, by the author, into a single interface. Whilst control is handled by the cRio-9022, acquisition is routed through a PXIe-1073; with both communicating with a single PC. This allows the user interface to be properly redesigned to display all rig critical systems on a single persistent screen, including: bearing, oil and water temperatures, seal balancing, mass flow rate, rotor and shaft speed, exit valve and heater array control. A second screen displays the acquired data, updating in realtime, allowing the user to view and monitor all aspects of the rig.

4 Data Processing

This chapter introduces the conduction heat transfer data analysis technique used. All experimental data presented is acquired under thermally steady state conditions. A 2D conduction modelling strategy is presented and used to derive Nusselt numbers from the experimental temperature measurements. A number of comparisons are made to test and validate this approach.

4.1 Nondimensional Test Matrix

The Phase A test programme comprises a series of tests using the experimental apparatus detailed in section 3.2.2. A test consists of starting the ancillary systems and axial throughflow air. Once this is thermally stabilised, the heaters, rotor and shaft are switched on simultaneously. It takes approximately 45 minutes to reach a thermally steady state condition, which is assumed when the thermocouples show a change of less than 0.2 K within 5 minutes (within their uncertainty limits). The parameters varied throughout the programme include the rotor and shaft rotational speeds, N_r and N_s respectively, and the axial throughflow mass flow rate $\dot{m}$. The heater setting was maintained at a constant level throughout.

The range of nondimensional variables (defined in section 2.1.2) relevant to rotating cavity experiments for Phase A are given in Table 4.1.

The parameters varied throughout the Phase B programme include the rotor rotation speed, N_r, shaft rotational speed, N_s and mass flow rate, $\dot{m}$. The heater setting was constant throughout. The range of the nondimensional parameters for Phase B is given in Table 4.2.

Parameter	**Range**
Axial Reynolds Number	$1.13 \times 10^5 < \mathrm{Re}_z < 5.14 \times 10^5$
Rotational Reynolds Number	$1.65 \times 10^6 < \mathrm{Re}_\theta < 3.16 \times 10^6$
Rossby Number	$0.10 < \mathrm{Ro} < 0.60$
Buoyancy Parameter (shroud)	$0.32 < \beta\Delta T < 0.40$
Buoyancy Parameter (diaphragm)	$0.13 < \beta\Delta T_{av} < 0.17$
Grashof Number	$3.40 \times 10^{11} < \mathrm{Gr} < 1.25 \times 10^{12}$

TABLE 4.1: Range of nondimensional parameters for Phase A

Parameter	**Range**
Axial Reynolds Number	$1.2 \times 10^4 < \mathrm{Re}_z < 5.2 \times 10^4$
Rotational Reynolds Number	$1.5 \times 10^6 < \mathrm{Re}_\theta < 3.2 \times 10^6$
Rossby Number	$0.05 < \mathrm{Ro} < 1.34$
Buoyancy Parameter (shroud)	$0.33 < \beta\Delta T < 0.51$
Buoyancy Parameter (diaphragm)	$0.15 < \beta\Delta T_{av} < 0.26$
Grashof Number	$2.4 \times 10^{11} < \mathrm{Gr} < 1.6 \times 10^{12}$

TABLE 4.2: Range of Nondimensional Parameters for Phase B

where $\beta\Delta T_{av}$ is based on the radially weighted average diaphragm to inlet temperature difference. Unless otherwise stated, all thermodynamic properties are evaluated at bore conditions. The different maximum Grashof number obtained between Phases A and B is due to a reduced maximum operating speed in Phase B due to concerns over rig vibration level.

4.2 Heat Conduction Methodology

This section establishes the conduction modelling methodology adopted in this thesis based on the MATLAB® Partial Differential Equation Toolbox™, hereinafter referred to as the 'PDE solver'. All subsequent comparisons are made on the upstream surface of disc three (Figure 3.1 J) for a single test, Baseline Case A from Phase B, whose working conditions are: $\mathrm{Re}_\theta = 1.6 \times 10^6$, $\mathrm{Re}_z \times 10^4$, $\mathrm{Gr} = 3.58 \times 10^{11}$, $\beta\Delta T = 0.42$, $\beta\Delta T_{av} = 0.17$ and Ro = 0.59.

4.2.1 The Heat Equation

The parabolic partial differential equation describing the internal temperature distribution in a region over time (such as in Figure 4.1) is given as;

$$\rho C \frac{\partial T}{\partial t} - \nabla \cdot (k \nabla T) = Q_v \tag{4.1}$$

where C is the specific heat capacity, ρ the material density, k the thermal conductivity and Q_v the volumetric heat generation rate. In the case of thermally steady-state conditions, $\partial T/\partial t = 0$ and no internal heat generation, $Q_v = 0$, Equation 4.1 reduces to:

$$\nabla \cdot (k \nabla T) = 0 \tag{4.2}$$

In the case of an axisymmetric system, such as an MCR rotating disc, is it convenient to express Equation 4.2 in cylindrical coordinates, such that;

$$\frac{1}{r}\frac{\partial}{\partial r}\left(kr\frac{\partial T}{\partial r}\right) + \frac{1}{r^2}\frac{\partial}{\partial \theta}\left(k\frac{\partial T}{\partial \theta}\right) + \frac{\partial}{\partial z}\left(k\frac{\partial T}{\partial z}\right) = 0 \tag{4.3}$$

where r is the radius, θ the circumferential and z the axial coordinate. By assuming the system is axisymmetric, then $\partial T/\partial \theta = 0$, which reduces Equation 4.3 to;

$$\frac{1}{r}\frac{\partial}{\partial r}\left(kr\frac{\partial T}{\partial r}\right) + \frac{\partial}{\partial z}\left(k\frac{\partial T}{\partial z}\right) = 0 \tag{4.4}$$

In this case the cylindrical form of Equation 4.2 is given as;

$$\nabla \cdot (kr \nabla T) = 0 \tag{4.5}$$

Equation 4.5 is the form of the heat conduction equation used by the PDE solver.

The surface normal heat flux is calculated from the radial and axial components. The heat flux given is the summation of both the conductive and radiative, such that:

$$q_T = q_C + q_R \tag{4.6}$$

The radiative component q_R is calculated using view factors (Howell, 1982) and the method detailed in Long (1999). This is subtracted from the total to give the conductive heat flux required by Equation 2.9.

4.2.2 Geometry and Boundary Conditions

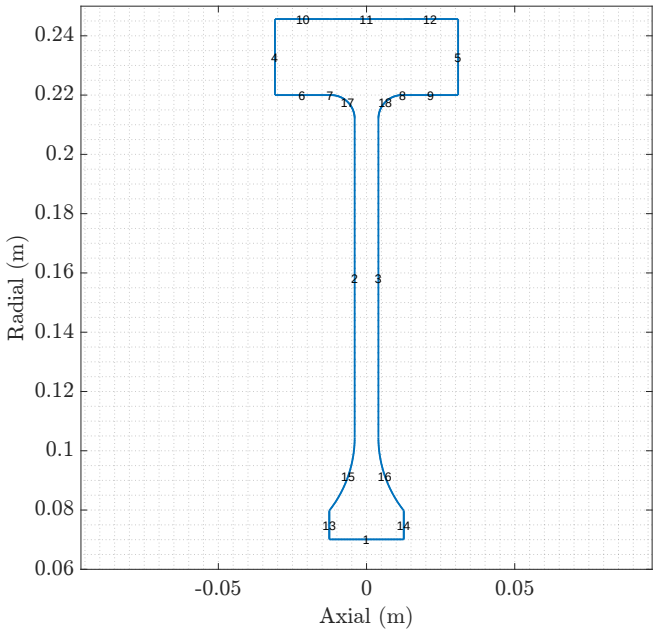

FIGURE 4.1: Geometry domain of MRC disc three. The numbered labels around the edges indicate the domain boundaries

The PDE solver uses finite-element analysis for the solution of PDEs. This method is readily applicable to arbitrary 2D and 3D geometries that, whilst not impossible, are considerably more difficult to numerically model using finite-differencing algorithms. In the case of the MCR rotating discs this allows geometric components such as the cob, shroud and outer rim to be modelled alongside the fillet radii, as opposed to the finite-difference approach assuming constant thickness throughout the disc or an area-weighted average thickness (Patounas, 2007), which can be readily modelled using an equally-spaced rectangular grid.

Figure 4.1 shows the geometric domain, MRC disc three, used. Whilst increasing the computational load and mesh size, the rim (domain boundaries 10, 11 and 12 in Figure

4.1) is included to ensure an accurate isothermal condition on the outer surface and also allows thermocouple 9, see Figure 3.2, to be used for validation. On all disc surfaces (diaphragm, cob and bore) interpolated experimental temperatures are used as fixed isothermal boundary conditions. This is also extended to the shroud surface. Domain boundaries 4 and 5 are adiabatic, based on the assumption that the heat flux is predominantly in the radial direction in the rim. The thermal conductivity is constant throughout the domain at $k = 7.71$ W/mK.

4.2.3 Grid Independence

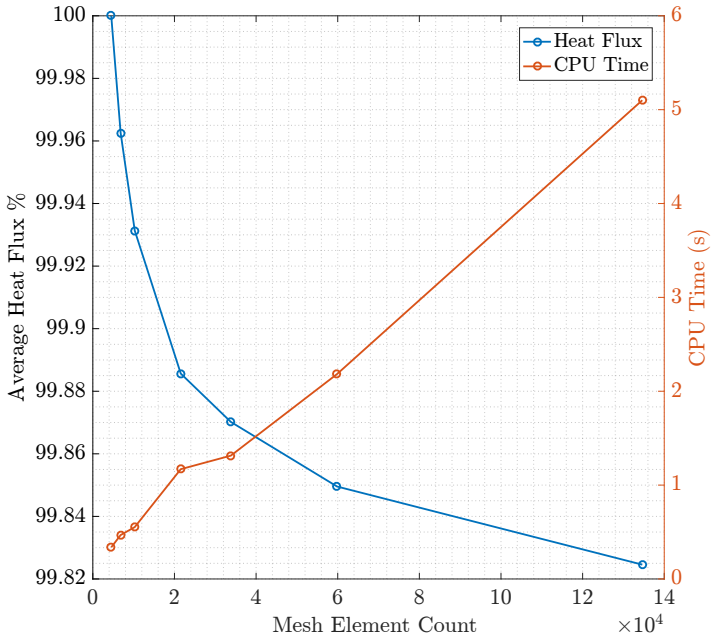

FIGURE 4.2: PDE solver independence study. Left axis shows average heat flux as a percentage of the coarsest mesh. The right axis shows the CPU time in seconds, conditions of Baseline Case A.

As with all numerical methods, a discretisation error is possible and must be mitigated to ensure confidence. A grid independence study was carried out using progressively finer elements on a single test case with a single curve fit to the measured temperatures. Figure 4.2 shows an early over-prediction of the average heat flux (presented as a percentage of the first mesh) that progressively diminishes, indicating convergence.

Also shown is the CPU time in seconds, trending upward as expected with increasing mesh size. From this, it can be seen that the computational time increases considerably between approximately 35000 and 135000 elements. whilst a 5 second calculation time is relatively short, the 35000 element mesh was chosen, due to the use of Monte Carlo uncertainty analysis (see section 4.2.5) which involves running the model many thousands of times and the negligible 0.02% difference in the average heat flux between them.

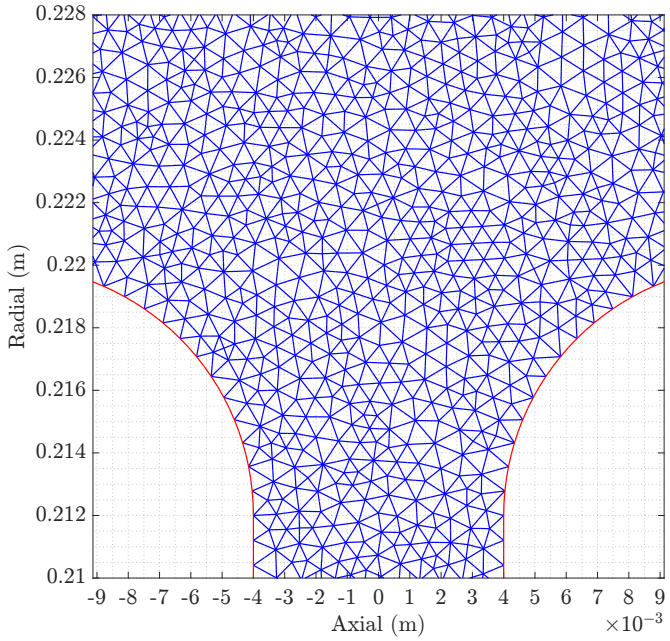

FIGURE 4.3: PDE solver unstructured mesh, close-up of the shroud corner joining the disc diaphram to the shroud

Figure 4.3 shows a closeup of the mesh elements in the vicinity of the shroud corner. Here, the maximum edge length is set to 0.8 mm, with a quadratic element order. The ability of the solver to handle the unstructured mesh allows it to closely approximate the curved parts of the domain without significant deviation from the true geometry. This mesh was verified against the internal thermocouple 9 (Figure 3.3) and found to agree to within 2 K for all tests in PhaseS A and B (Figure 4.4a). Given the stated instrumentation uncertainty of 0.5 K and that the model fails to account for some of the non-axisymmetric rig features such as instrumentation passages and disc pack bolt holes, this is considered acceptable.

A second verification (Figure 4.4b) compares to the 1D heat flux using the measured outer surface and shroud temperatures, $T_{sh,o}$ and $T_{sh,i}$ (thermocouples 64 and 7) respectively and is given as;

$$q_{sh} = \frac{k_{ti}\left(T_{sh,o} - T_{sh,i}\right)}{b\ln\left(D/2b\right)} \tag{4.7}$$

where D is outer diameter of the rotor (Figure 3.1 I) and k_{ti} is the thermal conductivity of titanium. Comparison to the 2D PDE solutions each test - using the same experimental conditions - shows a mean agreement to within 3% for Phase B and 8% for Phase A. The difference is likely due to the instrumentation differences (Phase B has more functioning thermocouples) defining a more accurate boundary condition. Considering that Equation 4.7 makes the assumption that the axial heat flux in the rim is negligible and ignores the non-axisymmetric features, this result is considered sufficient to give confidence in the subsequent analyses.

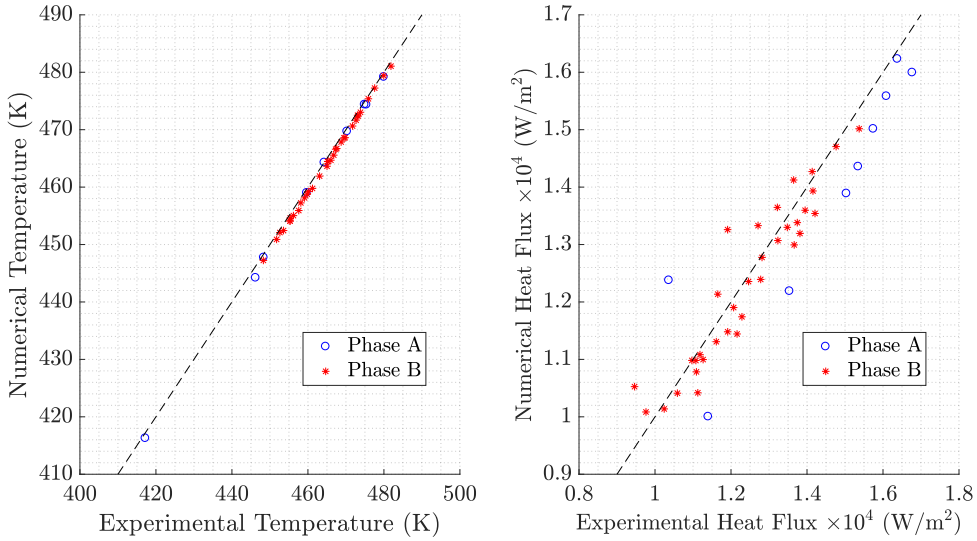

FIGURE 4.4: Validation of the PDE solutions: a) Comparison between numerical and experimental results at internal thermocouple 9. b) Comparison between numerical and experimental heat flux at the shroud surface, thermocouple 7.

4.2.4 Curve Fitting Comparison

The sensitivity of the calculated heat transfer coefficients to the measured temperatures when using the inverse procedure is well documented (Tang, 2017). Small errors in the temperature fit and unrealistic turning points in the curve significantly impact subsequent calculations. Previous work (eg. Alexiou (2000) and Cooke (2007)) has looked at the effects of 3rd, 4th and 5th order polynomials (usually higher orders are not considered due to instrumentation limitations and the introduction of false turning points) and cubic splines curve fits to the experimentally measured diaphragm temperatures. The sensitivity of the procedure is demonstrated by comparing the results back to analytical solutions based on the fin equation. A small study was conducted to choose a suitable curve fit to the measured temperatures by assessing the R^2, a statistical measure of how close to the data a fitted regression line is, and RMS error of the fit to experimental measurements. Five different fit types were used; the three polynomial forms already mentioned, a cubic spline and a 2nd order exponential function of the form $T = ae^{br} + ce^{dr}$, where a, b, c and d are coefficients to be determined.

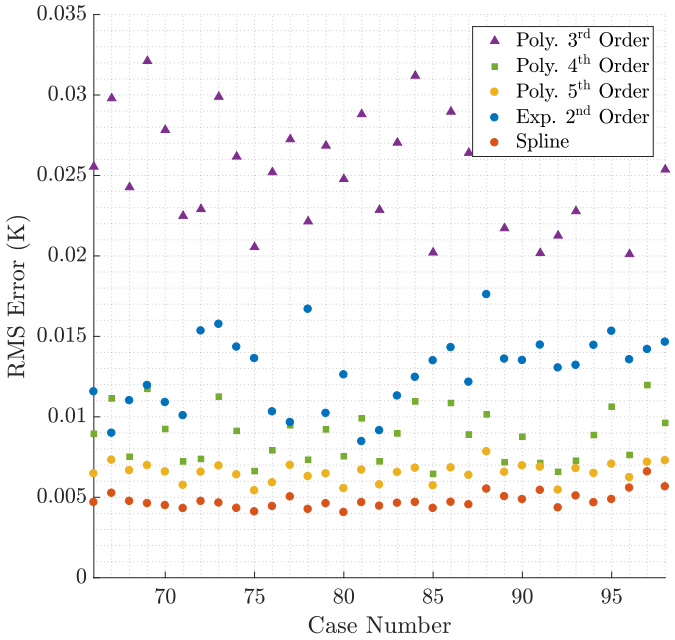

FIGURE 4.5: Comparison of RMS error of five different curve fitting types to experimental temperatures on disc three diaphragm

Figure 4.5 shows a comparison of the five different curve types. As expected the spline shows the lowest RMS error followed by the 5^{th} order polynomial. The 2^{nd} order exponential fit shows a increased error compared to the 4^{th} order polynomial, whilst demonstrating a markedly reduced error compared to the 3^{rd}. In all cases the R^2 parameter is above 0.995. From this it was decided to move forward to a Monte Carlo analysis using the 2^{nd} order exponential, 5^{th} order polynomial and spline curve types. It should be noted that in all cases the RMS is an order of magnitude smaller than the uncertainty, so the decision is also based on the historical choices made and that an exponential fit type has not been attempted previously.

4.2.5 Monte Carlo Analysis

The derived values of heat transfer coefficient, or Nusselt number, are extremely sensitive to the type of curve used to fit the experimental temperature measurements to an arbitrary numerical grid. Traditionally, this has been accepted due to the limitations of rotating instrumentation and thermocouple installation, i.e. four or five thermocouples in the disc radial direction and generally only on a single side. The number of thermocouples (Figures 3.2 and 3.3) on both upstream and downstream disc surfaces offers the opportunity to assess the type of fit in greater detail. However it becomes considerably more difficult to evaluate the Nusselt number uncertainty given the number of thermocouples and their individual experimental uncertainties. For this reason Monte Carlo simulation offers the most practical solution.

Monte Carlo simulation is an alternative to Taylor series uncertainty propagation analysis, which requires independent parameters and is considerably more complicated. This has been previously investigated by Cooke (2007) and shown to offer practical results for evaluating disc surface heat fluxes. In this strategy, classed as a stochastic process, the simulation model is repeatedly run, on the same mesh, using boundary condition temperatures based on those experimentally measured with an applied, randomly generated uncertainty within the prescribed bounds of ± 0.5 K, the experimental uncertainty. The type of probability distribution used is Gaussian. For each test case the PDE

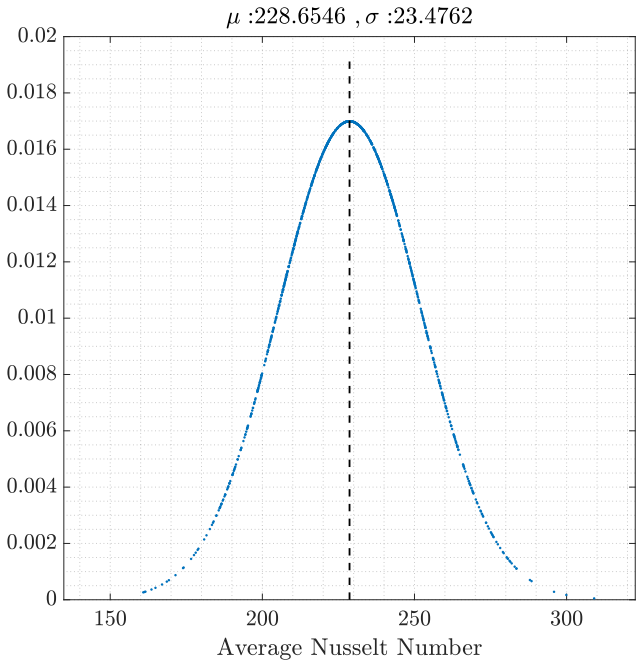

FIGURE 4.6: Monte Carlo simulation output showing Nu_{av}, Equation 2.10, distribution from 10,000 simulations of Baseline Case A

solver is run 10,000 times, which is considered sufficient (Coleman and Steele, 1999) and the surface normal heat fluxes recorded. A second Monte Carlo analysis is used to assess the surface Nusselt numbers, by applying a random uncertainty to the upstream reference temperature (thermocouple 136) discussed in Section 5.5 to give both local and average disc Nusselt numbers.

Figure 4.6 shows the average Nusselt number of Baseline Case A obtained using Monte Carlo simulation. The shape and density of the probability distribution indicates that the number of simulations is sufficient. With a suitable fit to the probability distribution, the mean and standard deviation are calculated and used to report the true mean value with a confidence interval, in this case 95% (1.96 standard deviations). Figure 4.7 shows the local Nusselt numbers, for Baseline Case A, along the diaphragm section of the disc. The shaded area shows the bounds of the 95% confidence interval with Nusselt number shown by a blue line. This is derived by fitting a probability distribution to each evaluation point, allowing the mean to be computed along with the standard deviation.

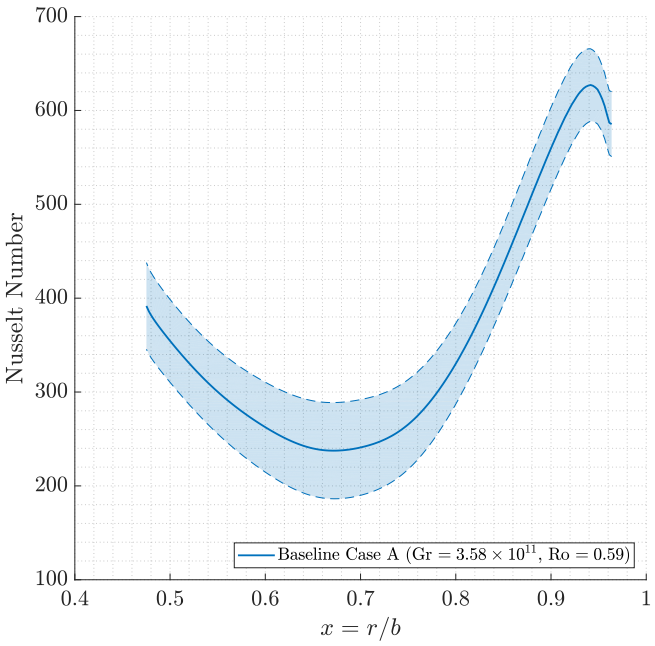

FIGURE 4.7: Monte Carlo simulation giving local Nusselt number along the disc diaphragm for Baseline Case A; Gr = 3.58×10^{11} and Ro = 0.59. The 95% confidence interval is indicated by the shaded area.

4.3 Temperature Fit Comparison

With the Monte Carlo procedure described the effects of different temperature curve fit types on the results can be assessed. For this a comparison is made between the smoothing spline, 5th-order polynomial and a 2nd-order exponential curve types for the Baseline Case A. For comparison to historical data these are assessed over the diaphragm section ($0.47 \leq x \leq 0.97$) only.

Figure 4.8 shows a comparison of the three fit types for the Baseline Case A. Clearly it can be seen that the 5th order polynomial is giving an incorrect profile, with several turning points and a sharp trend towards low Nusselt numbers near the shroud (indeed giving negative numbers in the region of the shroud corner). Similarly, whilst the spline shows a smooth decrease in magnitude towards the bore there is still a sharp decrease in latter regions. All three profiles show an increase towards the cob, yet the exponential profile shows a slight deviation in the outer region, arresting the downward trend that

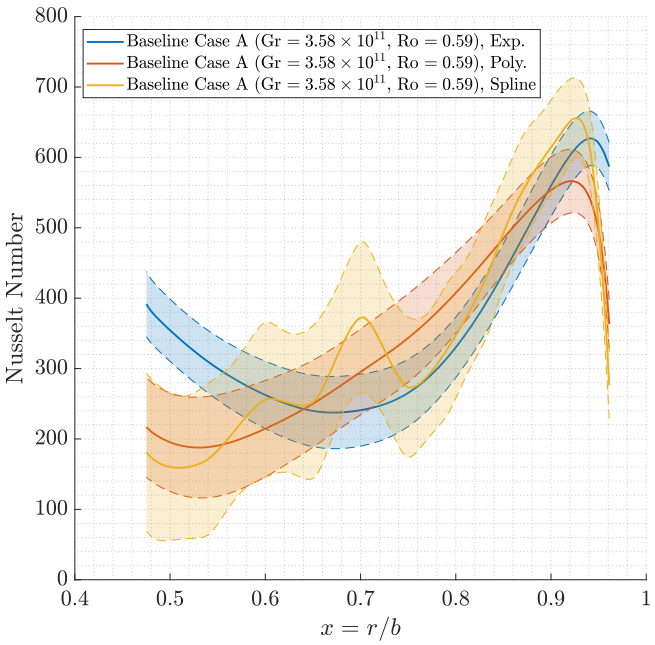

FIGURE 4.8: Comparison of different curve fits to experimental temperature profile for disc three upstream diaphragm, Baseline Case A; Gr = 3.58×10^{11} and Ro = 0.59.

is seen in the other two. The pronounced upward trend in the lower region, whilst appearing false, is notably similar to trends reported by Günther, Uffrecht, and Odenbach (2012) and tends towards a similar magnitude as the other curves at the intersection of the lower fillet radii and cob side-wall.

Figure 4.9 shows the absolute error in the numerical solution at the validation point (thermocouple 9) across all tests using the three different curve fit types. Whilst this validation point is not located on the disc the effects of the fitting are shown to have an impact. In all experimental cases the exponential fit has a reduced error when compared to both the polynomial and spline curve types. This is highlighted by the dashed lines indicating the mean error of all cases for each of the curve fits; the exponential has a mean of 0.9 K followed by the polynomial and spline with 1.5 K and 1.9 K respectively. For this reason the exponential fit is chosen for all further conduction analysis throughout this work.

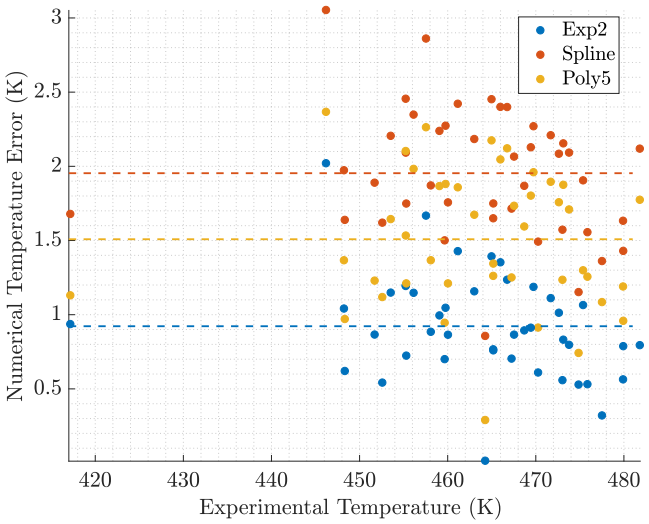

FIGURE 4.9: Comparison of different curve fits to error in validation temperature point across all Phase A and B experiments, dashed lines indicate the mean in each fit type.

4.4 Finite-Difference Comparison

For consistency a study was conducted to compare the current methodology with 2D finite-difference (FD) approach previously used, Miché (2008) and Patounas (2007). The FD approach begins with Laplace's equation for steady state axisymmetric conduction in cylindrical coordinates:

$$\frac{\partial^2 T}{\partial r^2} + \frac{1}{r}\frac{\partial T}{\partial r} + \frac{\partial^2 T}{\partial z^2} = 0 \tag{4.8}$$

This can be approximately via second-order FD equations such that:

$$\frac{\partial^2 T}{\partial r^2} \approx \frac{T_n - 2T_p + T_s}{\delta r^2} \tag{4.9}$$

$$\frac{1}{r}\frac{\partial T}{\partial r} \approx \frac{T_n - T_s}{2\delta r} \tag{4.10}$$

$$\frac{\partial^2 T}{\partial z^2} \approx \frac{T_e - 2T_p + T_w}{\delta z^2} \tag{4.11}$$

where the subscripts n, s, e, w indicate adjoining nodes in the 'north', 'south', 'east' and 'west' directions respectively to a central node p in a uniform rectangular grid with radial and axial spacing given by δr and δz respectively. Solution methods (Long, 1999) allow

for the interior temperatures to be calculated and the total surface heat flux to be given by a second-order backwards difference, such that:

$$q_T = -k\left(\frac{-2T_i + 4T_{i+1} - T_{i+2}}{2\delta n}\right) \tag{4.12}$$

where k is the thermal conductivity, δn the grid spacing normal to the surface and subscripts $i, i+1, i+2$ indicating adjacent nodes moving towards the interior of the grid. The radiative heat flux q_R is subtracted to give the conductive heat flux, q_C, as defined in Equation 4.6.

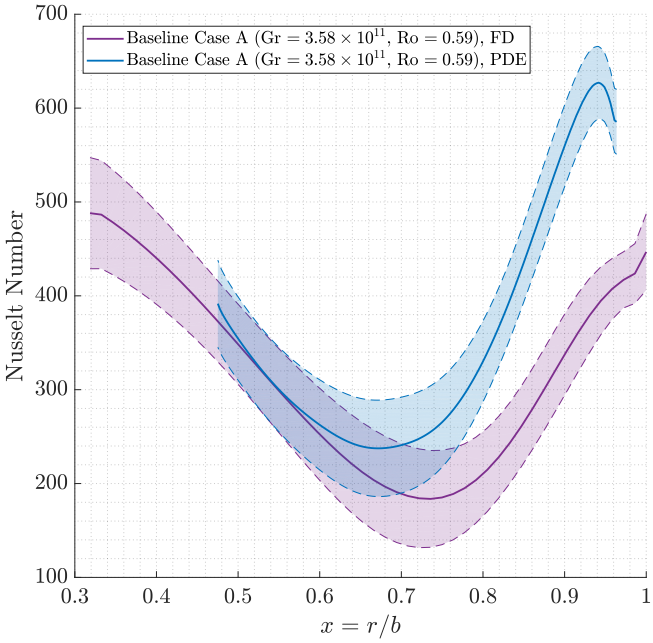

FIGURE 4.10: Comparison of Nusselt numbers between FD and the PDE solver. The 95% confidence interval is indicated by the shaded area, results are for Baseline Case A.

Figure 4.10 shows the Baseline Case A comparison between the FD and PDE solver Nusselt numbers, note that the PDE curve is only given for the diaphragm section of the disc but is based on the real geometry as shown in Figure 4.1 whilst the FD approach assumes a constant disc thickness from the shroud $x = 1$ to bore $x = 0.318$. The boundary conditions are the same in both cases with the exception of the FD upper (shroud)

condition which is linearly interpolated in the axial direction. An independence study of the grid number for the FD was conducted and found to not alter the results significantly.

Whilst there is almost exact agreement in the lower region ($x \approx 0.49$), and similar confidence levels there is particular disagreement in the upper region. The FD approach suggests that the upper region is at a similar magnitude of Nusselt number to the lower. This is contrary to the current understanding of buoyancy-induced flow in a rotating cavity with a radially increasing temperature distribution, which suggests higher Nusselt numbers at greater radius. However similar profiles of the Nusselt are shown by Alexiou (2000) who used a similar methodology. Notably the Nusselt numbers of the PDE solver are much higher in the outer regions, consistent with buoyancy-induced flow, and the confidence interval is also smaller, indicating a smaller uncertainty.

4.5 Solution Geometry Comparison

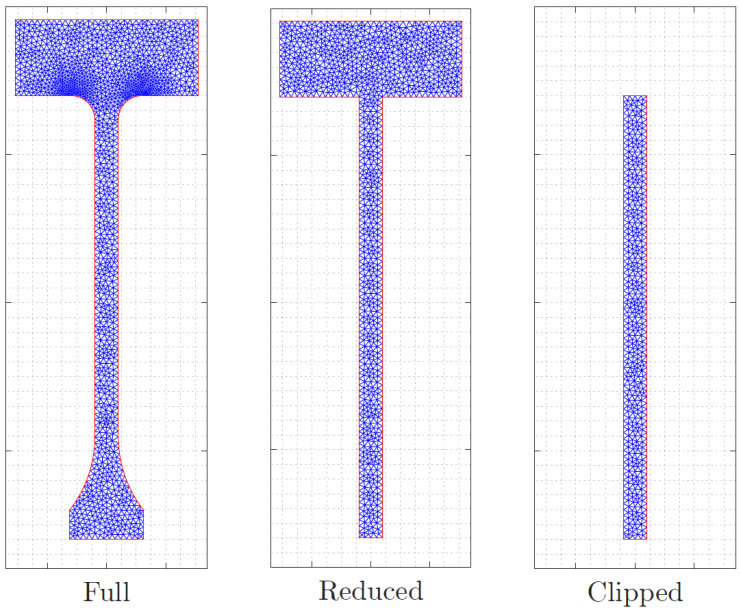

FIGURE 4.11: Modifications of disc geometry used for the conduction modelling. The FD method uses the *clipped* geometry

Whilst a comparison has been made between the FD and PDE solver, it is not complete, notably the two numerical methods use different boundary and geometry conditions. The direct application of the FD approach uses a rectangular grid mapped to the

assumed *clipped* geometry shown in Figure 4.11 whilst the PDE method is applied to the *full* geometry. To investigate the effects of the geometry on the derived Nusselt numbers a study was conducted using the three geometries shown in Figure 4.11 alongside the results from the 2D FD method. Also shown is the PDE mesh used with a maximum edge length established from the independence study in section 4.2.3.

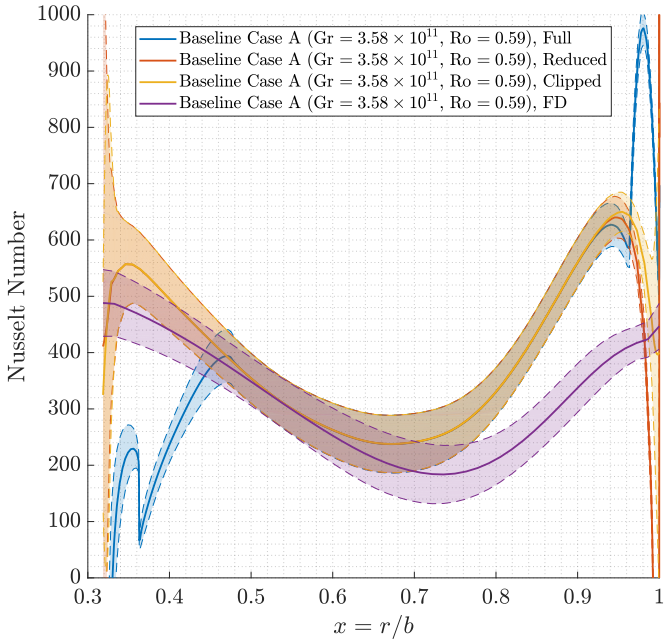

FIGURE 4.12: Comparison of local disc heat fluxes for the different geometries shown in Figure 4.11

Figure 4.12 shows a comparison of Nusselt numbers for the three geometries using the PDE solver method alongside the results of the FD approach. To fully appreciate the differences the entire disc length is shown rather than just the parallel-sided diaphragm section previously shown. Whilst there are clear differences between the four curves they all intersect in the region of $0.46 \leq x \leq 0.62$.

The effect of the shroud corner is demonstrated by the substantial peak in the full geometry. Whilst there is a slight increase in Nusselt number in the other geometries they quickly tend to a large decrease, indicating a strong heat flux gradient in that region. The removal of the rim from the clipped geometry has resulted in negative numbers at the shroud. This is contrary to current understanding and considered erroneous. The

FD approach, whilst in partial agreement, is clearly under-predicting in the near shroud region.

In the near bore region the full geometry diverges. Firstly there is a near linear decrease between $0.36 \leq x \leq 0.46$ which corresponds to the upper radius of the cob and an continual increase in the disc thickness towards the bore. At $x \leq 0.36$ the cob sides show a profile that is thought to be erroneous due to the general trend and very large confidence interval in that region (later shown in Figure 5.4). The small ΔT and Nusselt number sensitivity to temperature uncertainty means that any prediction must be rejected. Overall the full geometry of Figure 4.11 conforms to the general trend of the others whilst having the advantage of capturing more subtle effects and is used in Chapter 5.

4.6 Thermocouple Density Sensitivity Analysis

The number of instrumentation points on both sides of disc three (Figure 3.2) allows an assessment of the sensitivity of the PDE solution to the temperature fit. By reducing the number of thermocouples used to fit the curve to the experimental temperatures, the impact this has on the Nusselt numbers and confidence interval can be investigated. Previously, Cooke (2007) looked at increased thermocouple numbers on a theoretical test case, concluding that a higher density did not offer improved results or a reduction in the associated uncertainty. To assess the impact of the thermocouple density a Monte Carlo simulation was conducted on Baseline Case A using half and then a quarter of the thermocouples used in the standard conduction model. This was achieved by using every second and then every fourth thermocouple respectively. The same second-order exponential fit was used in each assessment. The first and last thermocouple along the disc is in each case the same, to fix the upper and lower boundary conditions. The *full* geometry, as discussed in section 4.5, was used.

Figure 4.13 shows the local upstream Nusselt numbers, with 95% confidence intervals, of the diaphragm of Baseline Case A. The upstream bore temperature (thermocouple 136) is used as the reference and the local radius r is used as a length scale. Whilst there is

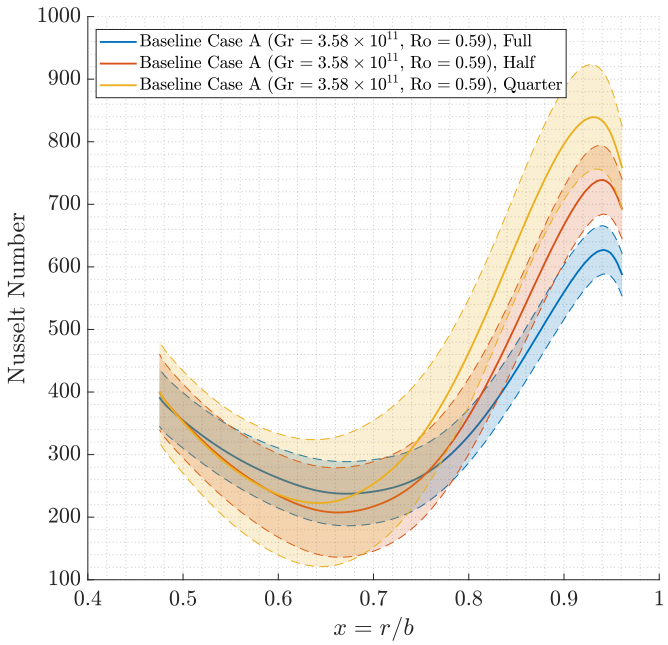

FIGURE 4.13: Nusselt number thermocouple density sensitivity. Full uses all instrumentation points, half uses every other point and quarter uses every fourth point. Instrumentation locations shown in Figure 3.3

agreement in the lower section it is clear that a reduction in the number of thermocouples has led to a relative over-prediction in the Nusselt numbers towards the outer radius, an increase of 35% between using all and a quarter of the thermocouples. The location of the lowest numbers has also shifted towards the bore. The confidence interval has also increased in size as the density was reduced, suggesting more uncertainty when using a more sparsely instrumented disc. This conclusion is opposed to that found by Cooke (2007) who suggested no improvement in uncertainty, a result that is unsurprising given that a reduced number of thermocouples leads to a less constrained curve fit.

4.7 Comparison to 1D Fin Solution

The final comparison to make concerning the conduction modelling is with regard to the 1D fin approximation. Following the methodology of Alexiou (2000) and Patounas (2007), the fin solution for a disc of half-thickness L and assuming a large radial temperature gradient in relation to the axial with an adiabatic boundary, Laplace's equation can

be reduced to:

$$\frac{\partial^2 T}{\partial r^2} L + \frac{\partial T}{r \partial r} L - \frac{q_T}{k} = 0 \tag{4.13}$$

where q_T is the total normal heat flux. Rearranged:

$$q_T = kL \left[\frac{\partial^2 T}{\partial r^2} + \frac{\partial T}{r \partial r} \right] \tag{4.14}$$

Simple 1D finite differencing can be used to solve Equation 4.14 by approximating:

$$\frac{\partial^2 T}{\partial r^2} \approx \frac{T_{i+1} - 2T_i + T_{i-1}}{\delta r^2} \tag{4.15}$$

$$\frac{\partial T}{r \partial r} \approx \frac{T_{i+1} - T_{i-1}}{2 r_i \delta r} \tag{4.16}$$

where i corresponds to a node in the radial direction and δr is the node to node spacing.

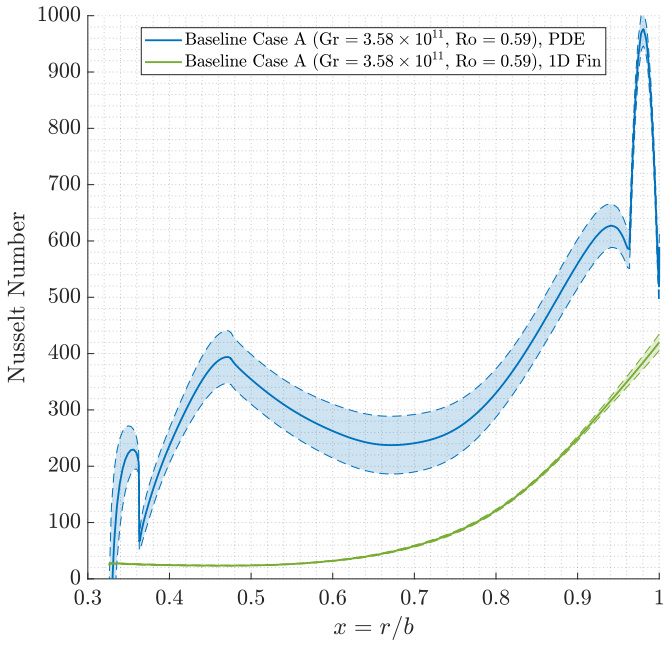

FIGURE 4.14: Comparison of PDE method to the 1D fin approximation

Figure 4.14 shows a comparison of Nusselt numbers for the previously established conduction model and 1D fin approximation. Note that the fin solution assumes a disc of

constant thickness. An exponential fit was applied in both cases and a Monte Carlo simulation performed to give confidence intervals. Clearly there is a large disparity between the two methods with the fin solution showing a much tighter confidence interval, indicating a reduced uncertainty. The profile of the fin solution also conforms to established results with an increasing magnitude of Nusselt number with radius. This suggests that over approximately half the disc there is very little heat transfer. Whilst the trend is appealing, the validity of the assumptions made is questionable and is discussed in Section 5.2.

4.8 Summary

This chapter has established the conduction methodology developed and adopted in this thesis. By using the finite element approach the real geometry of the disc can be modelled, including the outer diameter of the rotor disc pack. Validation of the model is through comparison to experimental measurement of metal temperature in the rim of the rotor disc pack and 1D heat flux through the shroud surface, both show good agreement. A curve fit of diaphragm radial temperature distribution using a second order exponential equation - not previously used - has been presented and shown to give reduced error (compared to spline and polynomial type curves) when validated against experimental measurements. Monte Carlo simulation has been used to establish confidence intervals for the results and demonstrate that increased thermocouple density does reduce the uncertainty of reported Nusselt numbers, however the accuracy is impossible to determine without a controlled experiment. The PDE solution has also been compared to the previously used FD approach using an equally spaced rectangular grid. Confidence intervals for the most part were unaffected but the FD solution gives results that do not conform to current understanding of rotationally induced buoyancy driven flows. The geometry of the conduction solution was investigated and shown to conform in some parts however the inclusion of the shroud corner has demonstrated a sharp increase in the local heat flux

suggesting a high heat transfer area. This is investigated in more detail in Section 5.4. Finally a comparison is made to a 1D fin approximation, that whilst giving a clearer trend to the heat transfer profile is of questionable accuracy when considering the assumptions made, see Section 5.2.

5 Heat Transfer Results

This chapter primarily discusses the results of Phase B with all tests used in the derivation of correlations and for comparative plots of average values. Phase A results are discussed in detail in Tang, Puttock-Brown, and Owen (2017) and presented here for comparison. Phase B covers over 30 tests however only two baseline test case results are presented in detail here - due to commercial sensitivity - and all results are reported from disc three.

5.1 Phase 2A Results

Figures 5.1-5.3 show the nondimensional temperatures and local Nusselt numbers from the disc three upstream surface for the Phase A test program, in descending order of Rossby number. The nondimensional temperature is defined as:

$$\Theta = \frac{T_s - T_{in}}{T_{sh} - T_{in}} \tag{5.1}$$

where T_{in} uses thermocouple 136 (Figure 3.2), T_{sh} is thermocouple 7 and T_s the local diaphragm surface temperature. This is used for both sides of the disc and explains why in some cases $\Theta > 1$. Across all results there is a notable trend in both the Nusselt number and Θ; at the higher Rossby number (Figure 5.1a) the diaphragm temperatures are proportionally lower. In the case of Ro = 0.6 the upstream $\Theta_{max} \approx 0.9$, this increases to $\Theta_{max} \approx 0.99$ for Ro = 0.1 . A similar trend is seen in at the lowest radius with $\Theta_{min} \approx 0.11$ for the highest Rossby number, increasing to $\Theta_{min} \approx 0.24$ in the lowest. There is also a clear difference between the up- and downstream Θ at the lowest radius in the highest Rossby case which attenuates as Rossby number trends down.

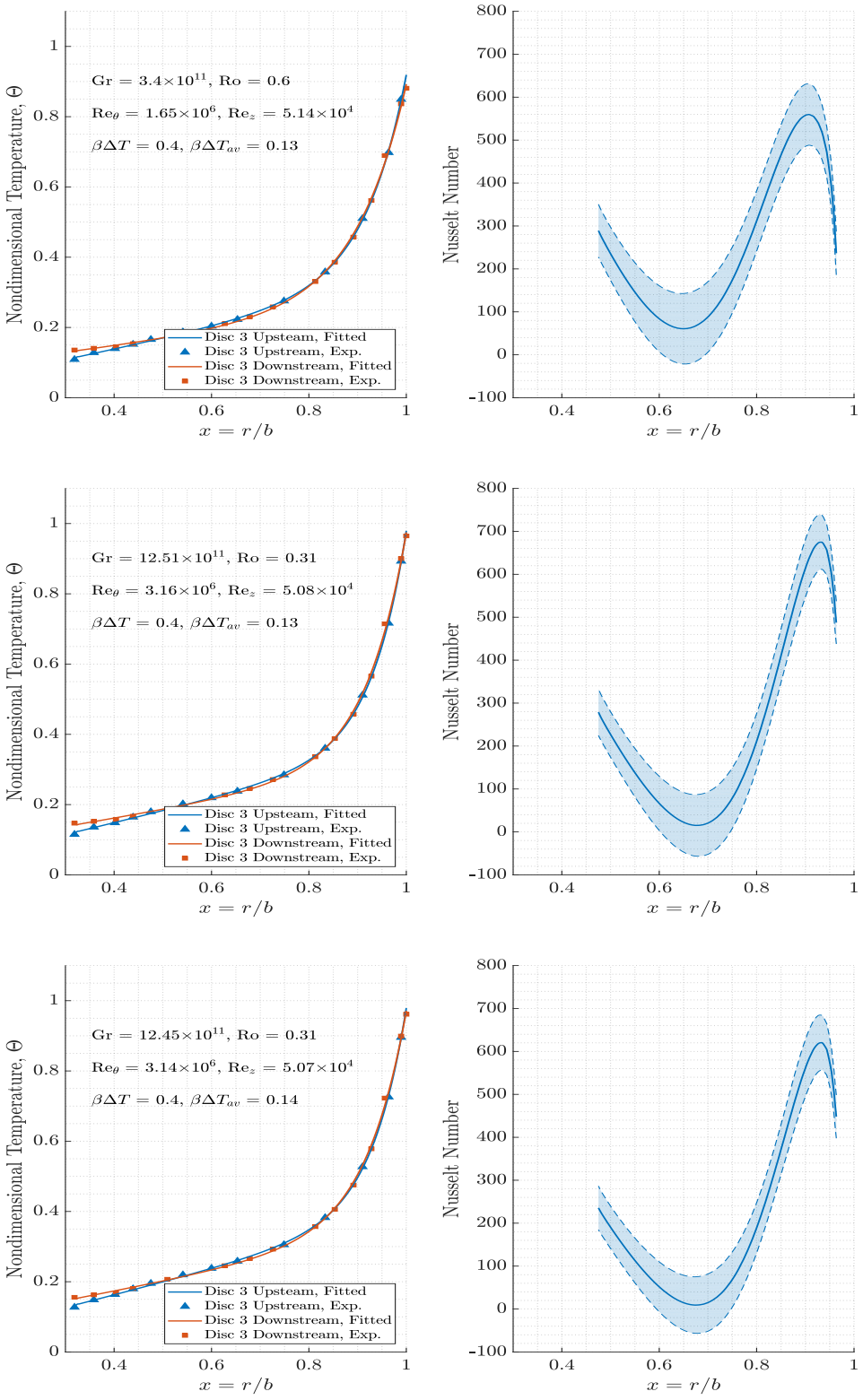

FIGURE 5.1: Nondimensional temperature and Nusselt number distributions for Phase A, $0.31 \leq \text{Ro} \leq 0.60$

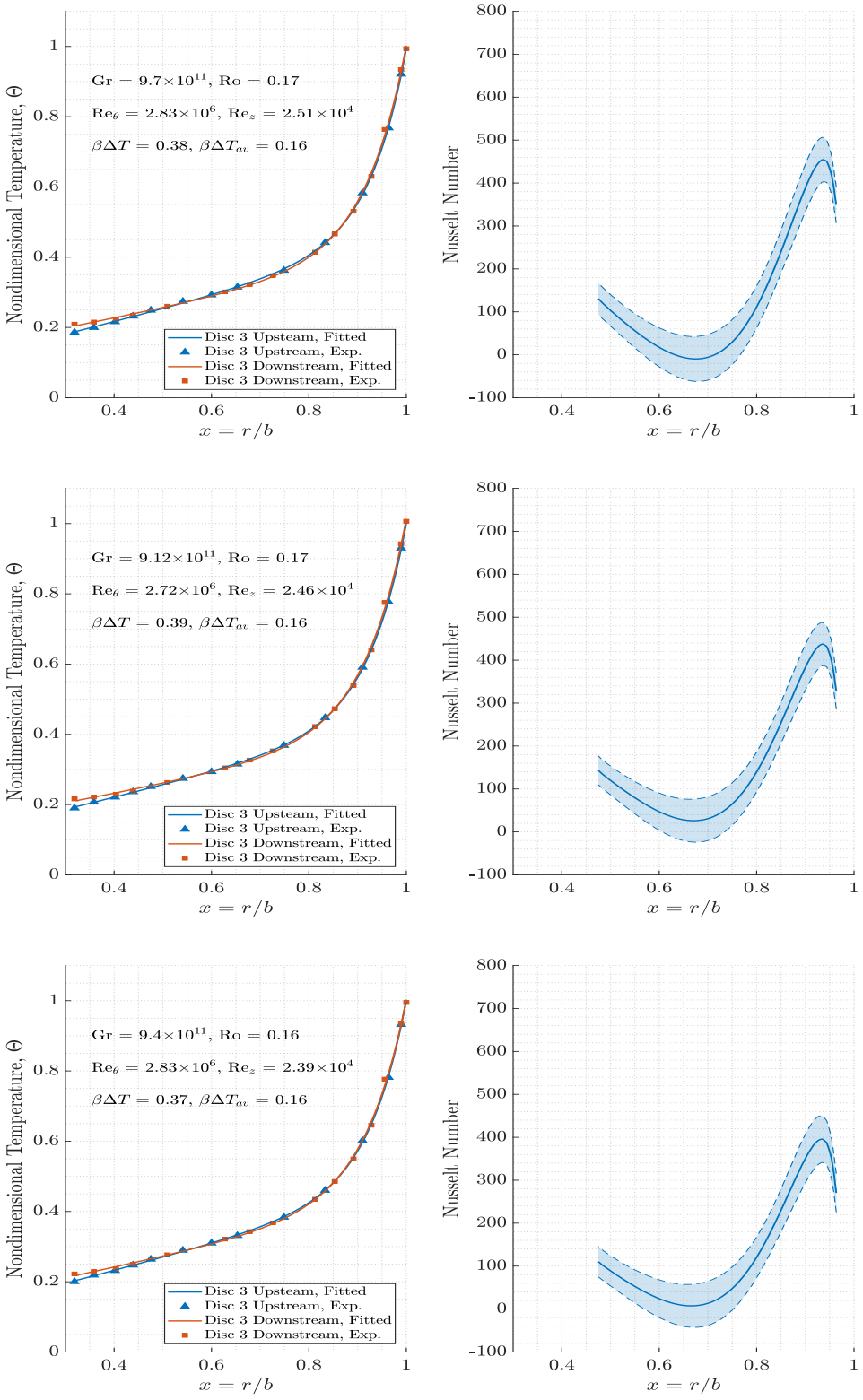

FIGURE 5.2: Nondimensional temperature and Nusselt number distributions for Phase A, $0.16 \leq \text{Ro} \leq 0.17$

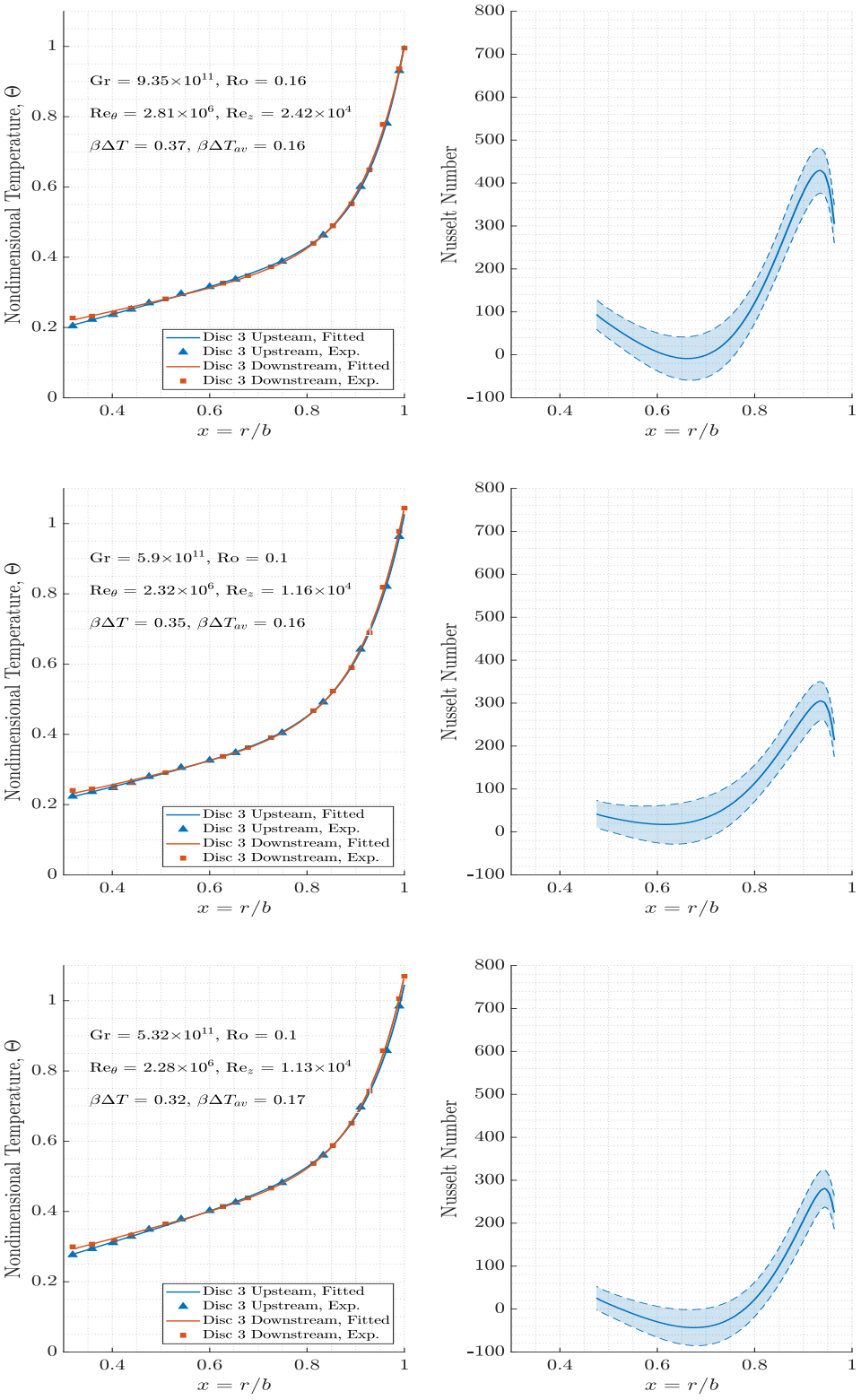

FIGURE 5.3: Nondimensional temperature and Nusselt number distributions for Phase A, $0.10 \leq \text{Ro} \leq 0.16$

The local Nusselt number, defined as:

$$\mathrm{Nu} = \frac{q_C r}{k_{air}(T_s - T_{in})} \tag{5.2}$$

where T_{in} uses thermocouple 136, show a trend dependency on Rossby number; in the higher region ($0.31 \leq$ Ro ≤ 0.6) the maximum Nusselt numbers seen across all Phase A tests are noted. The maximum value decreases with Rossby number; from Nu ≈ 680 for Ro = 0.31 to Nu ≈ 280 for Ro = 0.1. The difference in each case between the maximum and minimum Nusselt number decreases with Rossby number, indicating the disc temperatures vary less with radius, reducing the radial temperature gradient.

The distinct shape of the Nusselt number distribution seen across all tests, with a local minima at $x \approx 0.65$ can be explained in part by the difference between the upstream and downstream surface temperatures. At the point of minimum Nusselt number the downstream surface temperature is lower than the upper (contrary to the multiple rotating cavity system with increasing temperatures downstream). In all cases this is seen across $0.57 \leq x \leq 0.82$. The conduction model, using the experimentally measured temperatures as boundary conditions, in some cases indicates negative surface heat flux across this region - flowing upstream to downstream - resulting in negative Nusselt numbers. This is compounded by the uncertainity in the measurements and relatively low temperature difference across the disc, resulting in the confidence intervals in all cases showing negative Nusselt numbers.

5.2 Overview of Phase B Results

Figure 5.4 shows a representative plot of the disc heat transfer Nusselt numbers with 95% confidence intervals for both the upstream and downstream sides of disc three (Figure 3.2). The x-axis represents surface length S, beginning at the cavity mid-plane and finishing at the inner radius of the cob ($x = 0.318$). In this case the Nusselt number (Equation 2.9) uses the same length scale, local radius r, for all parts to give a comparative level but

uses different reference temperatures based on the cavity inlet air temperature; upstream uses thermocouple 136 whilst downstream uses thermocouple 138 (Figure 3.3).

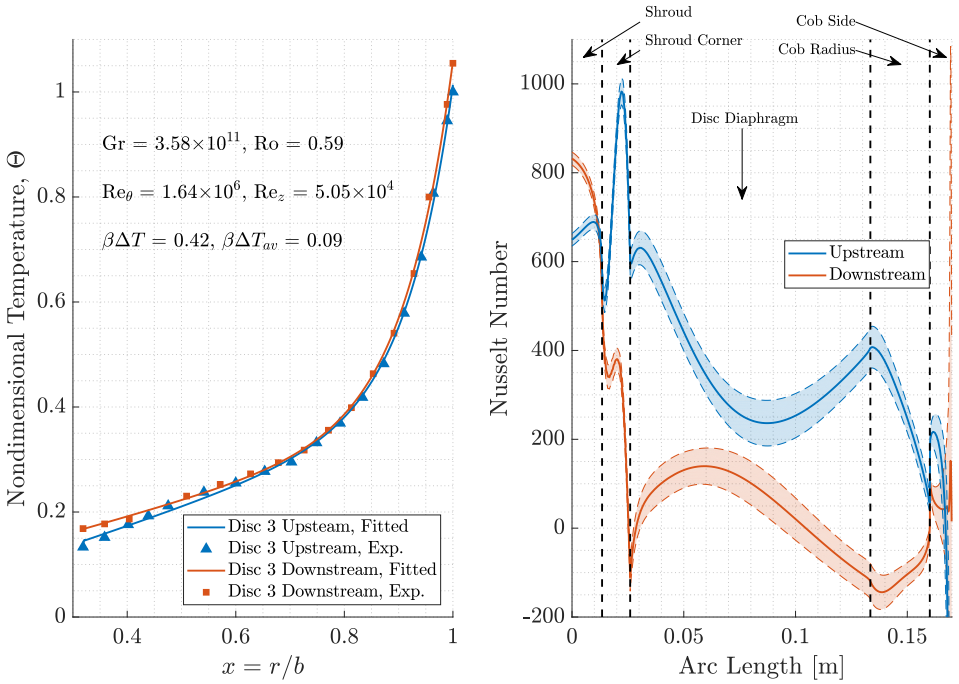

FIGURE 5.4: Nusselt number for baseline case A: Ro - 0.59 , $\beta\Delta T_{av} - 0.17$

Clearly there is a disparity between the up- and downstream sides of the disc. The upstream side predominantly shows a higher Nusselt number with a clear peak in the shroud corner region at $S \approx 0.025$ before decreasing with r (increasing S), at $S \approx 0.09$. This increases towards the cob radius corner at $S = 0.135$ where there is a decrease with radius. Whilst the downstream side does not show this trend, it does show a similar level of heat transfer at this point. The shroud Nusselt numbers between the cavities separate as they approach their respective mid-planes, a result not unexpected due to the thermal differences. As the outer rim is the heat source in the system, there is a larger axial metal temperature gradient than in the throughflow air. There is an increase of 14 K cavity to cavity at the shroud but only a 7 K increase between the bore reference temperatures, giving a progressively greater ΔT in the axial direction.

Whilst there are some regions of negative Nusselt number on the downstream disc, indicating heat transfer into (or across) the disc, it is not entirely negative. Miché (2008)

could not reconcile negative Nusselt numbers on one side of the disc when using a 2D conduction model with the understanding of cavity flows. However Günther, Uffrecht, and Odenbach (2012) used a two-cavity rig (Figure 2.12) with opposing thermocouples on each side of the disc and using 2D conduction model showed heat fluxes (Nusselt numbers were not calculated) both positive and negative. A similar result was reported by Burkhardt, Mayer, and Reile (1993) who also used a multi-stage cavity rig. The negative Nusselt numbers support the following explanation; considering that the conduction solution is not in error (as supported by Günther, Uffrecht, and Odenbach, 2012), the only rationalisation is that locally ΔT is negative, indicating a hotter gas than metal temperature. In the outer region this might possibly be explained by hot gas leaving the shroud surface and travelling down the disc surface. Compared to the metal ($k_{ti} = 7.71$ W/mK and $k_{air} \approx 0.0217$ W/mK) the gas cannot conduct heat away fast enough, leaving it hotter than the metal and inverting ΔT. Towards the bore the inverted ΔT may be due to non-uniform core flow; hot gas leaving the shroud surface and travelling radially inward in the core region. Such a phenomenon is reported in Chapter 6 using the numerical results. With this in mind it is considered that the values shown in Figure 5.4 are not necessarily in error. However it is clear that for $S > 0.16$, the cob side, the results are not reliable due to the relatively small ΔT. This demonstrates the implicit difficultly in defining an appropriate reference temperature, especially in the rotating cavity environment.

To reconcile Figure 5.4 with the understanding of cavity flows the differences between the current 2D conduction solution and previous work should be addressed. Günther, Uffrecht, and Odenbach (2012) found similar trends with heat flux along the diaphragm noting that at higher radii the results were consistent with buoyancy-induced flow, whilst at lower radii forced convection from the throughflow was likely impinging on the upstream disc surface. Historically, lack of disc instrumentation (e.g. Alexiou, 2000) and comparative similarity meant that it was prudent (and convenient) to model the discs as extended radial fins. This can be accomplished either through a 1D model of the surface temperatures or a 2D model of the disc from surface to an axial mid-plane that was assumed adiabatic. This assumption derives from the general solution of extended fins,

that the only conductive heat transfer present in the system is radial, i.e. there is no heat transfer across the sides of the fin, giving an adiabatic mid-plane. It then becomes instructive to consider this assumption in light of the 2D conduction model and instrumentation density.

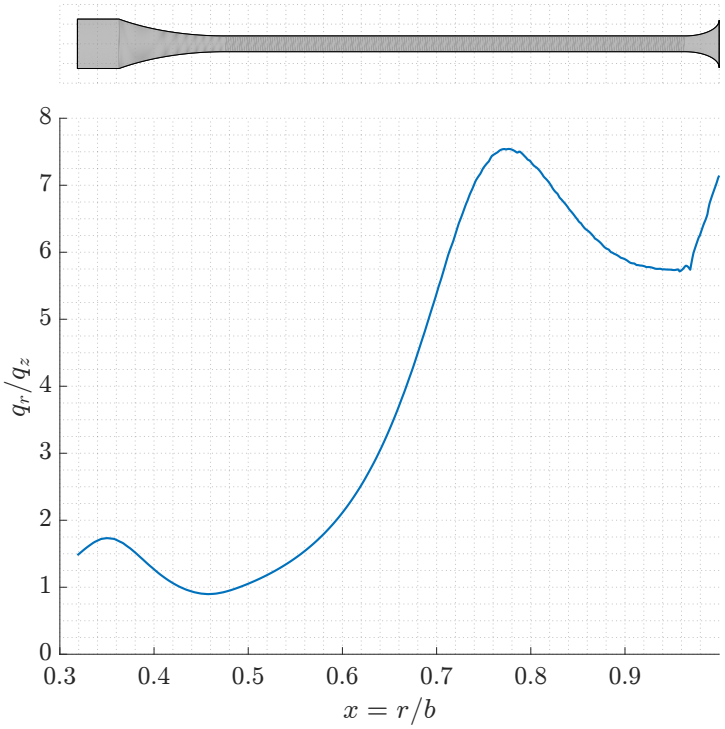

FIGURE 5.5: Radial to axial heat flux ratio on disc mid-axial plane. Result of baseline case A; Ro = 0.59 , $\beta\Delta T = 0.09$

Figure 5.5 shows the ratio of radial to axial heat flux along the mid-plane of the disc. If $q_r/q_z \gg 1$ then the heat flux across the disc surface (from cavity to cavity) can be considered negligible, allowing the disc to be modelled as an extended fin. At $q_r/q_z = 1$ the axial heat flux is equal to the radial and the fin approximation cannot be substantiated. Whilst it is clear that the radial heat flux is generally greater it cannot be considered to entirely dominate the axial, especially in the lower regions. The fact that it is stronger is no surprise as the driving temperature is from the outer radius of the rig. With this in mind it is considered appropriate to look at the up- and downstream sides independently rather than model the disc as a fin with a single temperature for both sides. For

the results presented in this thesis the focus will be on the upstream side of the disc due to the instrumentation density in that cavity, commercial sensitivity and the comparison to numerical results presented later in Chapter 6.

5.3 Heat Transfer Results from the Shroud

Results from this Section have been previously reported by Puttock-Brown, Rose, and Long (2017) and only a summary is given here.

When considering the shroud, a modified form of Grashof number Gr_{sh} is used, such that;

$$\mathrm{Gr}_{sh} = \frac{\rho^2 \Omega^2 b \beta \Delta T_{sh} \left(s/2\right)^3}{\mu^2} \tag{5.3}$$

where β is the volume expansion coefficient ($\beta = 1/T_{in}$) and fluid properties are evaluated at T_{cav}, the measured air temperature at thermocouple 175, located at $x = 0.982$. The cavity air inlet temperature, T_{in}, is the average of two shaft mounted air thermocouples (136 and 145), located upstream of the cavity at the mid-plane of the preceding disc. The surface to air temperature difference is $\Delta T_{sh} = T_{sh} - T_{cav}$, where T_{sh} is thermocouple 7. All thermocouples are shown in Figure 3.3. The use of a measured cavity air temperature is consistent with Long and Tucker (1994b).

The shroud Nusselt number, Nu_{sh}, uses a characteristic length scale that is the ratio of the exposed surface area to perimeter, such that;

$$\mathrm{Nu}_{sh} = \frac{q_{sh}(s/2)}{\left(T_{sh} - T_{cav}\right) k_{air}} \tag{5.4}$$

where the heat flux, q_{sh}, is given by Equation 4.7 and T_{cav} is used as a reference temperature. This is the total (convective and radiative) heat flux so a radiation correction has been applied to give only the conductive contribution. The radiative heat flux is found to be approximately 10% of the shroud total, similarly reported by Long and Childs (2007).

Figure 5.6 shows shroud Nusselt numbers Nu_{sh} from the Phase B test results, shown

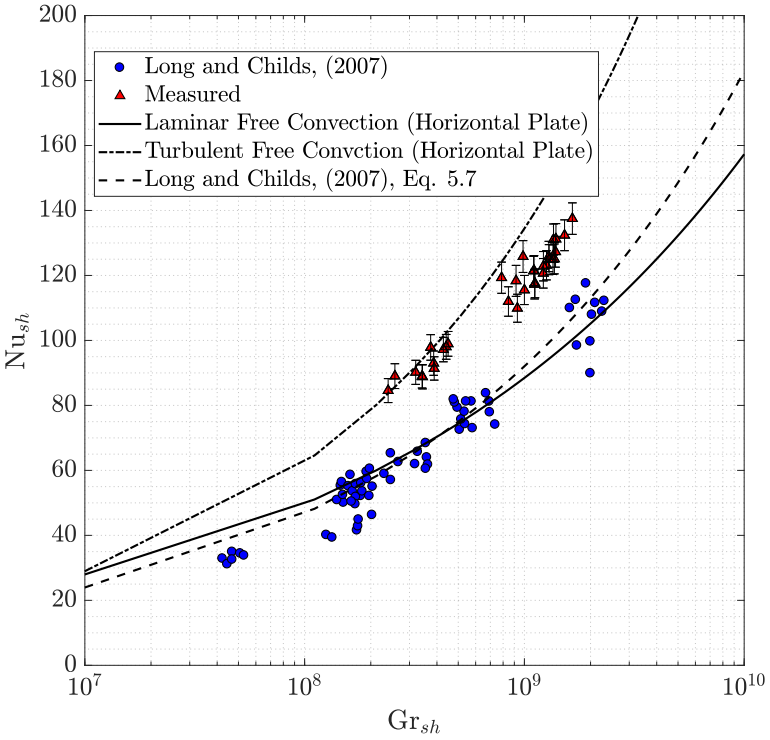

FIGURE 5.6: Variation of shroud Nusselt number with Grashof number for $d_h/b = 0.164$

as red triangles, alongside data reported by Long and Childs (2007), shown as blue circles. Uncertainty bars are also shown, these are derived using a Taylor series uncertainty propagation method and are approximately $\pm$ 5%. The accepted correlations for free convection from a horizontal plate (Lloyd and Moran, 1974) are given as:

$$\text{laminar}: \quad \mathrm{Nu}_{sh} = 0.54\,(\mathrm{Gr}_{sh}\mathrm{Pr})^{1/4} \quad \mathrm{Gr}_{sh} < 10^7 \tag{5.5}$$

$$\text{turbulent}: \quad \mathrm{Nu}_{sh} = 0.15\,(\mathrm{Gr}_{sh}\mathrm{Pr})^{1/3} \quad \mathrm{Gr}_{sh} > 10^7 \tag{5.6}$$

Alongside these, the correlation proposed by Long and Childs (2007) for an annular gap ratio $d_h/b = 0.164$ - similar to current configuration - is given as:

$$\mathrm{Nu}_{sh} = 0.25\,(\mathrm{Gr}_{sh}\mathrm{Pr})^{1/4} + 0.057\,(\mathrm{Gr}_{sh}\mathrm{Pr})^{1/3} \tag{5.7}$$

Equation 5.7 is based on a modification to the semi-empirical correlation of Grossmann

and Lohse (2000), Equation 2.14, for Rayleigh-Bénard convection between two plates in a stationary enclosure separated by a vertical distance. It was proposed that for a rotating cavity the hot surface is represented by the heated shroud and the cold by the axial throughflow (Long and Childs, 2007).

It is apparent that the current test series covers approximately the same range of Gr_{sh} however there is little agreement between the data of Long and Childs (2007) and the new measurements. This difference is primarily attributed to the air reference temperature used. In the Long and Childs (2007) data for both Gr_{sh} and Nu_{sh} is based on an adiabatic temperature increase using the inlet air temperature, T_{in}, such that:

$$T_{ref} = T_{in} + \frac{\Omega^2 \left(b^2 - a^2\right)}{2C_p} \tag{5.8}$$

as there was no cavity air temperature measurement in that programme.

Whilst there is a noticeable difference, the effects of radiation incident on the exposed thermocouple bead must be accounted for. For this a heat balance (Long, 1999) is considered between the incident radiation and the convective losses, such that:

$$h\left(T_f - T_p\right) = \sigma\epsilon\left(T_p^4 - T_s^4\right) \tag{5.9}$$

where ϵ is the probe emissivity and is assumed as 0.8, the measured flow temperature is denoted by T_p and the actual temperature by T_f. The heat transfer coefficient, h, is taken as that for a sphere of diameter d:

$$h = \frac{k}{d}\left[2 + \left(0.4Re_d^{1/2} + 0.06Re_d^{2/3}\right) Pr^{0.4}\left(\frac{\mu_\infty}{\mu}\right)\right] \tag{5.10}$$

where d is the thermocouple bead diameter, nominally 0.4 mm. As Equation 5.10 shows, there is a dependence on the relative velocity between the thermocouple and local flow. This poses a problem in that this is not known a priori due to the complex nature of the cavity flow field. From Long, Miche, and Childs (2007), time-averaged LDA gives results for the tangential velocity, V_θ, in the vicinity of the shroud. The nondimensional

rotational speed of the flow in the cavity relative to the cavity wall, swirl ratio, is given by $V_\theta/\Omega r$ and is shown to be approximately 1 in the near shroud region, indicating solid body rotation. This can vary on average between 0.95 and 1.05, indicating a $\pm 5\%$ slip of the flow to the wall. From this a 10% overestimate of slip is assumed. Heat balance convective losses are irrespective of the relative flow direction.

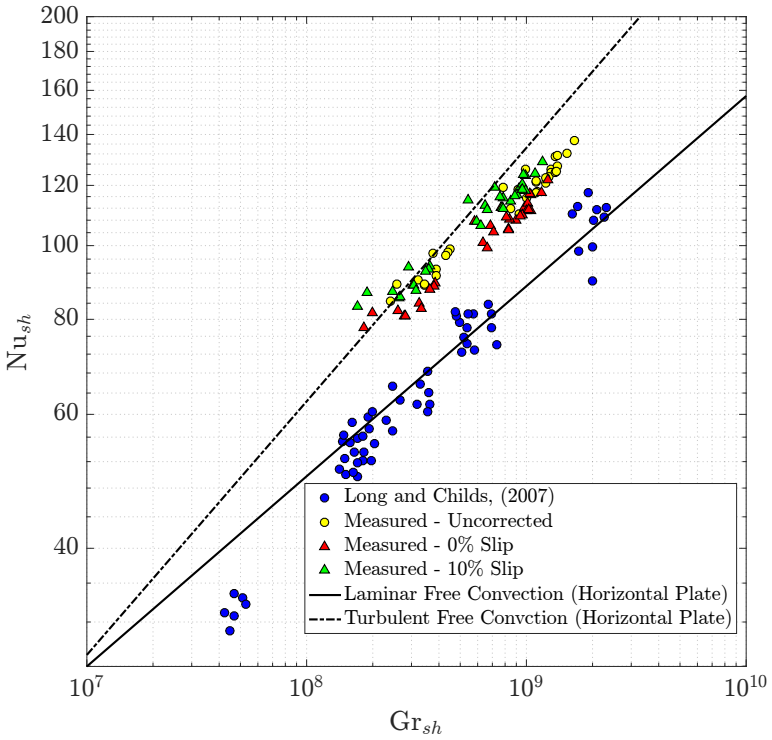

FIGURE 5.7: Log-log plot of variation of shroud Nusselt number with Grashof number for $d_h/b = 0.164$ with radiation correction

Figure 5.7 shows the measured data corrected for radiation error assuming either a 10% slip or solid body rotation (0% slip), as shown by green and red triangles respectively. In both cases there is a slight reduction in Gr_{sh} and Nu_{sh}, however there is a noticeable attenuation of the measured data and an increase in Nu_{sh} over the uncorrected data set for the 10% slip case.

The enhancement of Nu_{sh} is then attributable to not using an adiabatic temperature rise, T_{ref}, in the Nusselt number. Inspection of the experimentally measured cavity air temperature shows that T_{ref} consistently under-predicts the air temperature (compared

to T_{cav}) at the cavity periphery, in some cases by a significant fraction, indicating that Equation 5.8 is insufficient at predicting the near shroud air temperature. The close agreement to the turbulent correlation given in Equation 5.6 is considered coincidental, as turbulence has been shown to be suppressed in rotating cavities, and is thought not reflective of the underlying physical phenomena present. Whilst the magnitude of the flow is clearly in agreement with near turbulent levels of heat transfer, the underlying trend is not. It is proposed that the enhancement of the Nusselt numbers is in fact due to highly unsteady laminar flow with many differing length scales. It is noted that using $\beta = 1/T_{cav}$ in the definition of Gr_{sh} results in a reduction of the Grashof number, shifting the data to the left closer to the turbulent line, however this does not alter the trend of the data substantially and the trend is still indicative of a laminar trend.

To substantiate this, a regression analysis has been performed using the assumed solid body rotation data, giving:

$$\mathrm{Nu}_{sh} = 0.689 \left(\mathrm{Gr}_{sh}\mathrm{Pr}\right)^{1/4} \tag{5.11}$$

where the fit has an $\mathrm{R}^2 = 0.969$ with an RMS error of approximately 5% of the Nu_{sh} range. The fact that the data shows a very strong $\mathrm{Nu}_{sh} \propto \mathrm{Gr}_{sh}^{1/4}$ is in keeping with the known fact that rotation can suppress turbulent flow. The Coriolis force overrides the convection levels present and maintains a laminar behaviour at Grashof numbers that would, under non-rotating conditions, expect turbulent flow. In the present data there is no gradient change in Nu_{sh} to suggest a transition to turbulent flow, this may occur at higher levels of Grashof number.

Whilst numerical simulation of closed cavities (Sun et al., 2004) using LES has shown that the onset of turbulence is indeed suppressed by rotation, in the case of an open cavity the axial throughflow is expected to propagate into the cavity itself, leading to the onset of turbulence. The axial throughflow is shown to be highly turbulent (Puttock and Rose, 2016) and has previously been demonstrated to propagate deep into the cavity and close to the shroud (Owen and Powell, 2004), this would suggest a dependency of Nu_{sh} on the axial throughflow itself and by extension Re_z. Figure 5.8 shows a log-log plot with Re_z ranges defined via symbols. For clarity, only the radiation corrected 0% slip data is

shown.

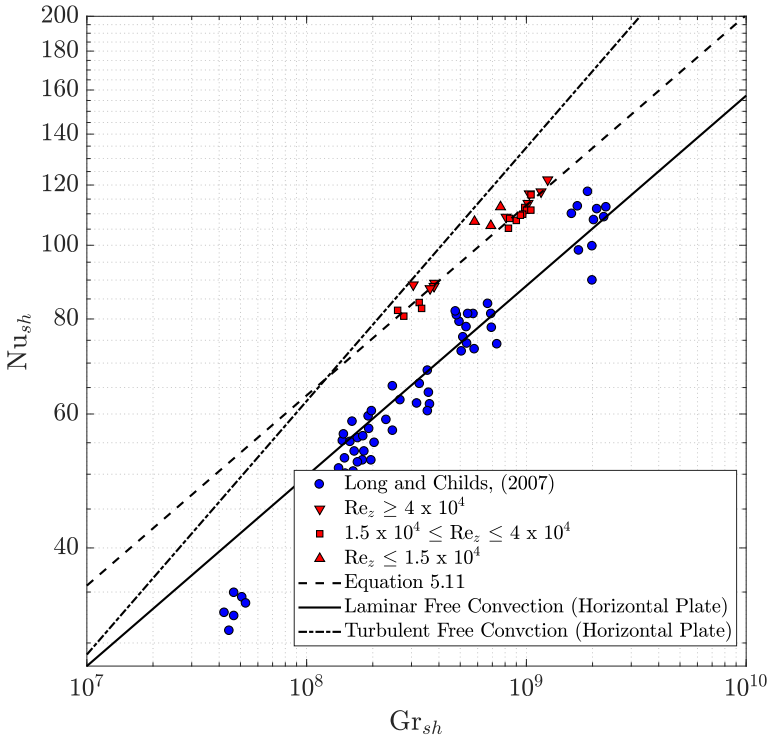

FIGURE 5.8: Log-log plot of variation of shroud Nusselt number with Grashof number for $d_h/b = 0.164$ with Re_z indicated

As Figure 5.8 shows, there is no clear dependence of Nu_{sh} on the axial throughflow, otherwise there would be a stratification based on Re_z. This suggests that the flow field in the near shroud region is dominated by free convection. The attenuation of the new results compared to the Long and Childs (2007) data suggests that T_{cav} is indeed the correct reference temperature to use in the calculation of Nu_{sh}, a conclusion reached by Long and Tucker (1994b).

There is a remaining question as to the practical implementation of these results. Whilst it is demonstrated that using T_{cav} may be the correct reference temperature for predicting Nu_{sh}, its incorporation into existing design practices may be difficult due to the lack of suitable models that can accurately predict the near shroud air temperature, especially in the higher buoyancy parameter cases which have been shown to drive increased thermal mixing (Atkins and Kanjirakkad, 2014). The original approach based on

large-scale Rayleigh-Bénard convection between the hot shroud and cold axial throughflow suggested by Long and Childs (2007) uses a reference temperature from the throughflow, or indeed the inlet temperature to a multiple cavity system. Prediction models here can be considered more reliable due to the dependence on forced convection in the axial bore throughflow.

5.3.1 Shroud Nusselt number comparison

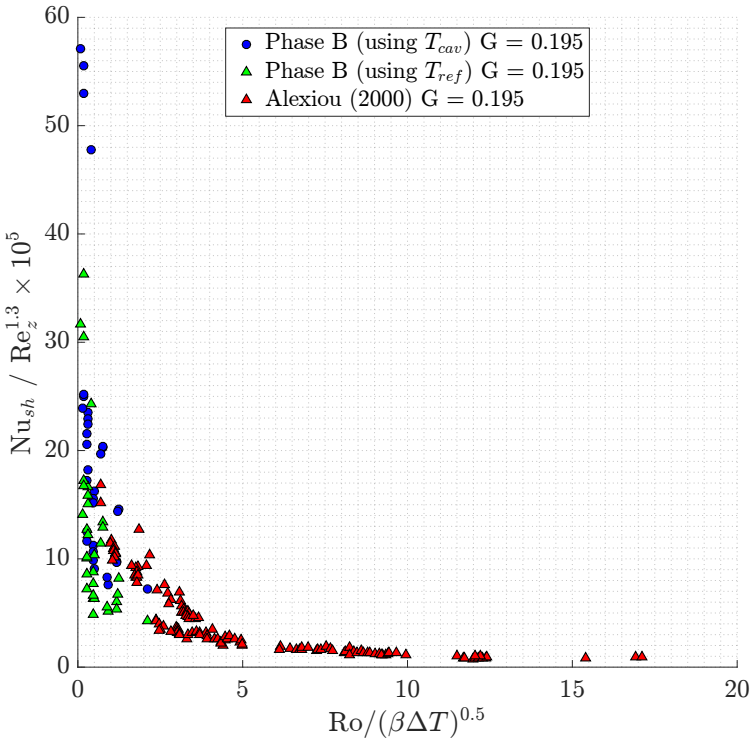

FIGURE 5.9: Comparison of shroud Nusselt numbers to Alexiou (2000)

Figure 5.9 shows a comparison of the Phase B shroud Nusselt numbers Nu_{sh} to existing results (Alexiou, 2000). The axes used reflect those used by Alexiou (2000) who found that they offered a good collapse of the data and allowed an assessment of the different regimes. For $\mathrm{Ro}/(\beta\Delta T)^{0.5} > 6$ the flow field is dominated by axial throughflow and shows very little change in gradient, for $\mathrm{Ro}/(\beta\Delta T)^{0.5} < 6$ the field is dominated by rotationally induced buoyancy effects. The term $\mathrm{Ro}/(\beta\Delta T)^{0.5}$ is also referred to as the

Buoyancy number, Bo (Sun et al., 2007). The exponent of Re_z is significant in that it is similar to that used in Nusselt number correlations for a disc-cone cavity section (Alexiou, 2000). In addition, the Phase B data using T_{ref} is also presented as this is calculated using an adiabatic temperature rise (Equation 5.8) which offers a fairer comparison.

The new results clearly continue the trend of the existing data, with the T_{cav} set showing a greater magnitude than T_{ref}. They are also all for $\mathrm{Ro}/(\beta\Delta T)^{0.5} < 6$ indicating rotational buoyancy effects and not the throughflow is significant, a conclusion also demonstrated in Figure 5.8. It is shown in Section 5.6 that the results are of a similar magnitude to the diaphragm and shroud corner.

5.4 Heat Transfer Results from the Shroud Corner

The shroud corner, where the vertical diaphragm surface transitions to the horizontal shroud, has received little attention in the past. In part this is due to the focus on both the shroud and disc surfaces as the dominant regions of interest and the lack of instrumentation. Yet being at the outer periphery of the cavity it is under very large thermal and structural stress, which is why this region is a fillet and not a square corner which would cause a stress concentration feature. In the current instrumentation layout, the shroud corner features three thermocouples on both the up- and downstream sides, and with the use of the methodology presented in Section 4.2 this area can be investigated in more detail.

Whilst there is very little literature regarding heat transfer of the shroud corner, indeed many experimental rotating cavities feature an ideal geometry and the interface between shroud and disc surface is perpendicular, there are some indications in previous work that suggests this region may have been overlooked. Farthing et al. (1992a) used calibrated fluxmeters to measure the local Nusselt number and performed comparative conduction solutions using finite-differencing. The outer fluxmeter, no. 8, was located at $x = 0.986$ on the upstream disc and $x = 0.981$ on the downstream. In tests conducted

for symmetric (both discs heated) radially increasing temperature profiles with an unheated shroud, the local Nusselt number shows a significant jump at fluxmeter 8. This is also true in comparisons made between different gap ratios and the inclusion of a central shaft. Similar results are reported in Long (1987) which show a larger number of tests from the same rig. In each test there is a significant jump in Nusselt number at fluxmeter 8, especially at lower Rossby numbers. However it should be noted that these tests did not feature a fillet or a heated shroud, which is shown to destabilise the flow (Long and Tucker, 1994b), and were a single rotating, idealised cavity.

Detailed inspection of Figure 5.4 shows the corner region on the upstream side ($0.015 \leq S \leq 0.025$) as having a significant enhancement in the local Nusselt number over both the diaphragm and shroud along with a very tight confidence interval that suggests this is not a numerical error, as it would be extremely sensitive to the temperature fitting (as with the bore).

Following Farthing et al. (1992a) in assuming the flow is governed by buoyancy-induced effects and that there is a radial inflow occurring in the boundary layers, it becomes pertinent to define the relative nondimensional parameters according to a new length scale based on the distance from the shroud, such that $y = b - r$. In this case the Grashof number (Equation 2.6) becomes:

$$\mathrm{Gr}_y = \frac{\rho^2 \Omega^2 y^3 r \beta \Delta T}{\mu^2} \tag{5.12}$$

Similarly the Nusselt number is redefined as:

$$\mathrm{Nu}_y = \frac{q_c y}{k_{air}\left(T_s - T_{ref}\right)} \tag{5.13}$$

where T_s is the local surface temperature and T_{ref} is a suitable reference temperature. Typically T_{ref} has been taken as the inlet air temperature to the cavity T_{in}, previously this has been located upstream and at a stationary point due to a lack of shaft instrumentation. In previous builds this meant outside the rotating test section (Alexiou, 2000) however the current shaft instrumentation allows a closer measurement of bore air temperature and

is taken from an average of the upstream thermocouples 136 and 145. As these can rotate (the shaft can be co- and counter-rotated or stationary) at a different speed to the rotor a suitable correction is made to give the relative total temperature in the rotor reference frame.

Whilst this is suitable, T_{in} is in some regards not representative of the free stream air temperature inside the cavity. It was found that using the film temperature, $T_f = (T_s + T_{in})/2$, which is the same temperature at which fluid properties are evaluated, offered a better representative temperature inside the cavity and led an improved correlation matching in both the shroud corner and diaphragm.

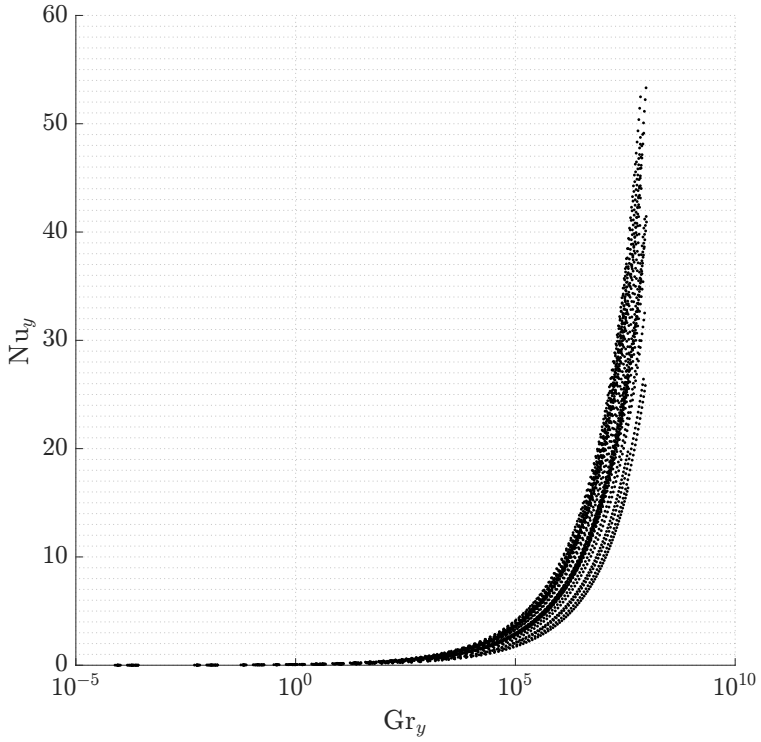

FIGURE 5.10: Variation of Nu_y with Gr_y for the upstream shroud corner for all Phase B tests

Figure 5.10 shows the variation of Nu_y against Gr_y for the shroud corner, derived using the PDE solution and represented by 100 equally spaced points around the corner for each test. The spread (no attempt was made to collapse the data) is attributed to the variation of Re_z and $\beta\Delta T$ in the series however it is clear that a common trend is shared across

tests, a strong indication that a common mechanism is responsible. Whilst it has been demonstrated that the heat transfer is dominated by free convection effects (at least on the diaphragm) the complexities of the flow in the region of a concave surface cannot be ignored. In the solution of the free convection boundary equations (Incropera et al., 2006) it can be shown that by assuming a non-zero free stream velocity (commonly in free convection, $u_\infty = 0$) the Nusselt number is expressed in the form of $\mathrm{Nu} = f\left(\mathrm{Gr}_L, \mathrm{Re}_L, \mathrm{Pr}\right)$. Therefore the effects of combined free and forced convection must be considered, namely when $\mathrm{Gr}_L/\mathrm{Re}_L^2 \approx 1$, similarly the effect of forced convection dominating free can be assumed when the inequality $\mathrm{Gr}_L/\mathrm{Re}_L^2 \ll 1$ is satisfied and free convection dominating forced when $\mathrm{Gr}_L/\mathrm{Re}_L^2 \gg 1$.

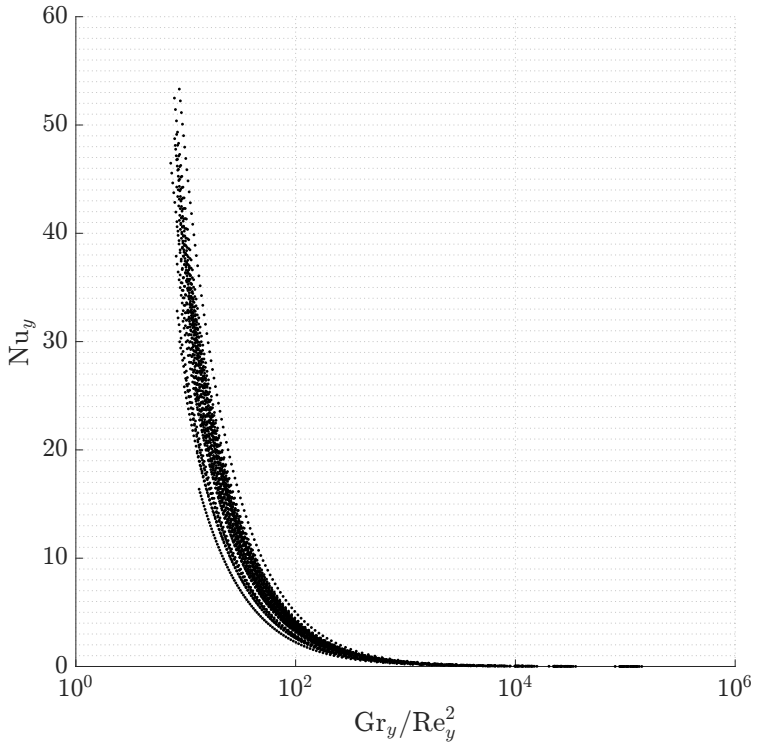

FIGURE 5.11: Variation of Nu_y with $\mathrm{Gr}_y/\mathrm{Re}_y^2$ for the upstream shroud corner

With this considered, Figure 5.11 shows a semi-log plot of Nu_y against $\mathrm{Gr}_y/\mathrm{Re}_y^2$ where;

$$\mathrm{Re}_y = \frac{\rho \Omega y^2}{\mu} \tag{5.14}$$

for all Phase B tests. Whilst the spread of data is again present, it is clear that the majority of the data shows $\mathrm{Gr}_y/\mathrm{Re}_y^2 \geq 1$. A cumulative probability distribution of all data shows that only 10% of the results are below 10 ($\mathrm{Gr}_y/\mathrm{Re}_y^2 \leq 10$) and that 80% of the data exists between a $\mathrm{Gr}_y/\mathrm{Re}_y^2$ ratio of 10 to 100. It is assumed then, that $\mathrm{Nu}_y = f\left(\mathrm{Gr}_y, \mathrm{Pr}\right)$ and a regression analysis is conducted, such that:

$$\mathrm{Nu}_y = C_1 \mathrm{Gr}_y^{C_2} \tag{5.15}$$

where C_1 and C_2 are coefficients to be determined. The effects of Pr are ignored due to the relatively low spread of temperature over the region since it only covers the nondimensional radial coordinate, $0.9636 \leq x \leq 1$.

The resulting regression analysis gives:

$$\mathrm{Nu}_y = 0.032 \mathrm{Gr}_y^{0.391} \tag{5.16}$$

with an $R^2 = 0.946$ and, more significantly, an RMS error of 4.5%, based on 3072 data points after rejecting the outliers. By allowing the exponent of Gr_y to remain *free* throughout the regression analysis it could be compared to controlled experiments which report suitable correlations without forcing. The value of 0.391 is significant as this is indicative of turbulent free convection on a vertical plate with constant surface temperature, given (Jaluria, 1980) as:

$$\mathrm{Nu}_y = 0.022 \mathrm{Gr}_y^{0.4} \tag{5.17}$$

Comparing Equations 5.16 and 5.17 shows that the multiplier is different, by approximately 50%. This is unsurprising given the unsteady and unstable nature of flow with rotating cavities. The comparison to a correlation based on constant surface temperature is thought suitable given the relatively weak variation of temperature. There does, however, remain the question of validity when concerning the geometry of the problem. It is well known that concave surfaces enhance Nusselt numbers locally, yet the question of the dominant flow direction remains.

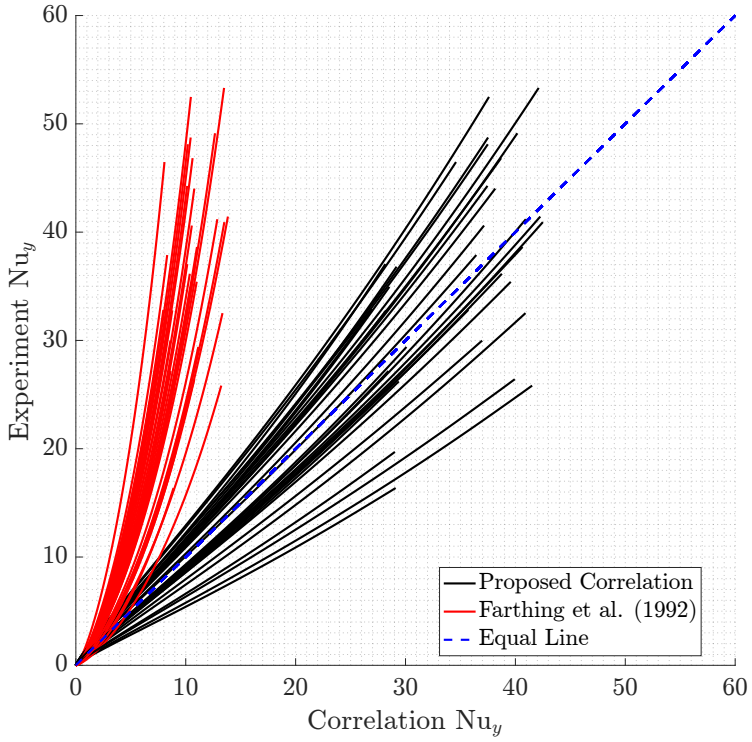

FIGURE 5.12: Experimental Nusselt numbers against correlation prediction (Equation 5.16) for the shroud corner

Figure 5.12 shows the proposed correlation, Equation 5.16, compared to experimental data alongside the correlation of Farthing et al. (1992a) given as:

$$\mathrm{Nu}_y = 0.0054\mathrm{Re}_z^{0.30}\mathrm{Gr}_y^{0.25} \tag{5.18}$$

on a plot of experimental against correlation Nusselt number. A dashed blue line is used to indicate a perfect prediction of the experimental results when using the correlation. Equation 5.16 shows mainly good agreement across the test series with some notable exceptions. Equation 5.18 shows some initial agreement yet quickly diverges. This is true in all cases and strongly under predicts the experimental results. Whilst there is a clear comparative spread from Equation 5.16 to the experimental results they are generally consistent with the accuracy of heat transfer predictions and it must be stressed that there are several parameters not acknowledged, such as Re_z. However this also supports

the hypothesis of buoyancy-induced flow in the outer part of the cavity, where the axial throughflow is thought to have minimal effect.

5.5 Heat Transfer Results from the Disc Diaphragm

The analysis of heat transfer data from the disc is split into two sections; firstly, the local Nusselt numbers are considered and then the average values, which can be compared to existing data to explore the underlying trends. All Nusselt numbers presented are (unless otherwise stated) for the upstream disc, diaphragm section, $0.47 \leq x \leq 0.96$, and derived from the conduction model described in Chapter 4.

5.5.1 Local Values

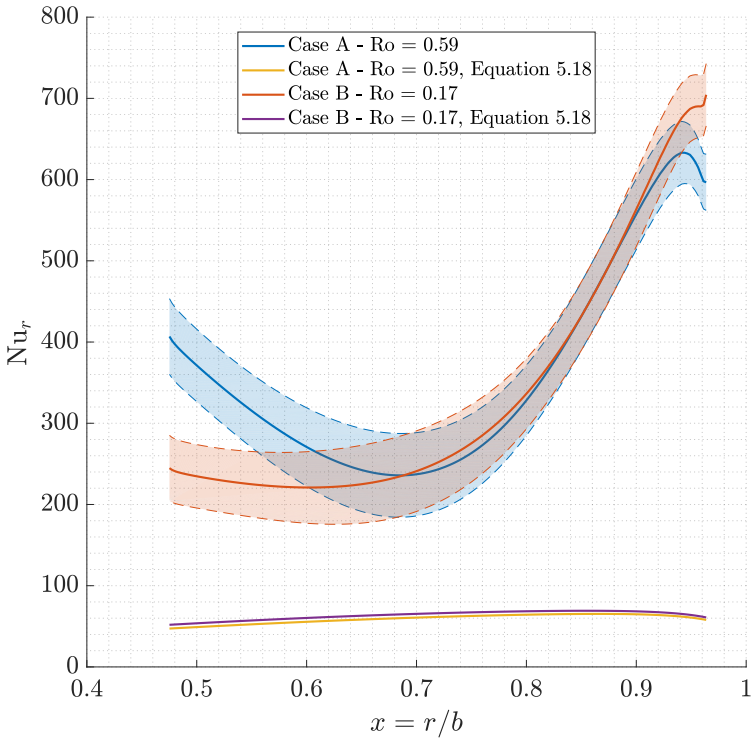

FIGURE 5.13: Measured local Nusselt numbers on the disc for baseline cases A & B with comparison to Equation 5.18

Figure 5.13 shows a comparison of Nusselt number, Nu_r against nondimensional radius, x, where:

$$\mathrm{Nu}_r = \frac{q_c r}{k_{air}\left(T_s - T_{ref}\right)} \tag{5.19}$$

where T_s is the local surface temperature and T_{ref} is a suitable reference temperature. Again this is taken as the film temperature as used in the previous section. This explains the apparently higher Nusselt numbers in Figure 5.13 when compared to previous work. This use of an assumed cavity free stream temperature (attempts were made to use measured cavity air temperatures however this resulted in poor results when using regression analysis) is similar to Tang (2017) in the calculation of Nusselt numbers, though it is worth noting that they used the fin approximation in estimating disc heat transfer.

Referring back to Figure 5.13, in both cases the local Nusselt number starts at a maximum (at least in terms of the disc section) and decreases towards a minimum located approximately halfway down the section. In the upper region of section, $x \geq 0.85$ there is close agreement between the Ro ≈ 0.59 and Ro ≈ 0.17 cases suggesting that the effects of the axial throughflow are not significant, nor is rotational Reynolds number Re_θ - given that the rotational speed of Case A is half that of B - conforming to previous work. In both cases the shaft is co-rotating at the same speed as the rotor so the effects of shaft rotation, if any, cannot be discussed though it has been previously shown that there is little to no effect of shaft rotation on disc Nusselt numbers (Miché, 2008). Further down the disc it is clear that the higher Ro case shows lower local Nusselt numbers and then trends towards higher. Given that the $\beta\Delta T$ between the two cases is approximately similar this effect is attributed to a greater Ro and greater penetration of the axial throughflow into the cavity and the possible establishment of a toroidal vortex.

The measured local Nusselt numbers are higher than those predicted by Equation 5.18 which shows less variation along the disc length. It is important to note that the differences of derivation between the measured numbers and those given by the correlation and the driving reference temperatures used, with T_{ref} taken from an upstream stationary thermocouple. Also in the experiments of Farthing et al. (1992a) the shroud was unheated. Fixing T_{ref} as the cavity inlet temperature in Equation 5.19 still results in

an under prediction, though much closer to the current measurements.

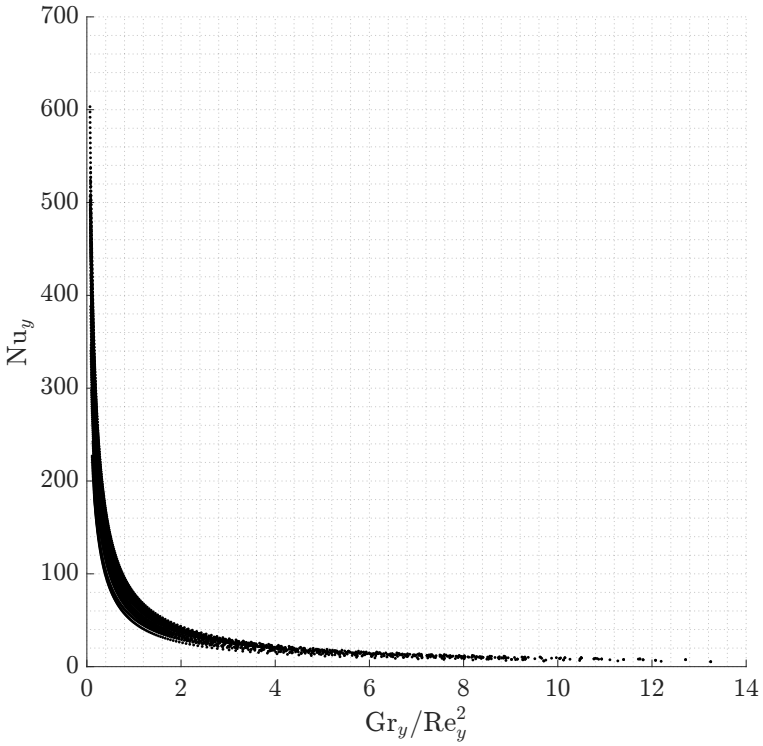

FIGURE 5.14: Variation of Nu_y with $\mathrm{Gr}_y/\mathrm{Re}_y^2$ for the upstream diaphragm

Following the analysis procedure presented in Section 5.4, the disc local Nusselt numbers are considered in terms of the shroud based length scale, y. Considering the literature on buoyancy-induced flow in rotating cavities, it seems prudent to acknowledge that the local free stream velocity, u_∞, is likely not zero, though in a time-averaged sense the flow can be considered as solid body rotation so $u = 0$. In this case it again becomes necessary to assess the relative balance of the free and forced convective effects.

Figure 5.14 shows local Nusselt numbers, Nu_y (Equation 5.13), against the ratio $\mathrm{Gr}_y/\mathrm{Re}_y^2$ for all tests, where each is represented by 200 equally spaced points along the diaphragm between $0.47 \leq x \leq 0.96$. It is clear that the ratio $\mathrm{Gr}_y/\mathrm{Re}_y^2$ is much lower compared to the shroud corner discussed in Section 5.4 with the majority of the data points below 1. There is also a noticeable spread in the local Nusselt numbers which can be attributed to the varying test conditions, namely Re_z, Re_θ and $\beta\Delta T$. However it is clear that all the

data follows the same trend, which suggests that the same convective mechanisms are responsible.

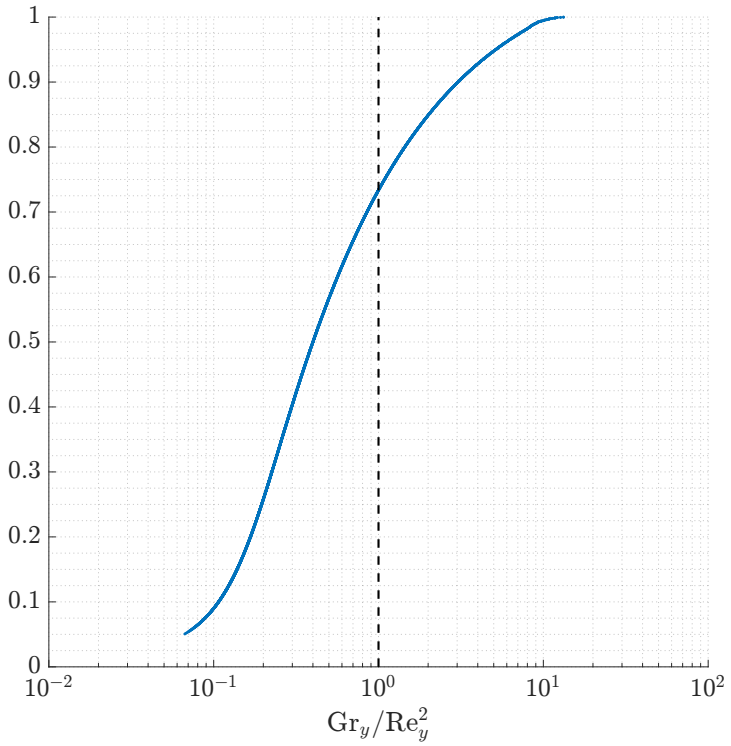

FIGURE 5.15: Cumulative probability distribution of $\mathrm{Gr}_y/\mathrm{Re}_y^2$ for all Phase B tests

Figure 5.15 shows the cumulative probability distribution for $\mathrm{Gr}_y/\mathrm{Re}_y^2$, for all data points and tests. Compared to Figure 5.11 for the shroud corner, it can be seen that nearly all points are ≈ 1, indeed 90% of the data lies within a factor of 10. This is considered to not satisfy the inequality posed regarding the domination of forced over free convection, especially when compared to Section 5.4 which showed 80% of the data was above a factor of 10. On this basis there is a strong justification to consider the effects of *both* free and forced convection when calculating the local Nusselt numbers. This is contrary to previous work that has considered only the effects of buoyancy induced flow whereby $\mathrm{Nu} = f(\mathrm{Gr}, \mathrm{Pr})$ when correlating experimental data. It is then assumed that

$\mathrm{Nu} = f\left(\mathrm{Gr}, \mathrm{Re}, \mathrm{Pr}\right)$ and the form of a correlation is:

$$\mathrm{Nu}_y = C_0 \left(\mathrm{Gr}_y \mathrm{Pr}\right)^{C_1} + C_2 \left(\mathrm{Re}_y \mathrm{Pr}\right)^{C_3} \tag{5.20}$$

The Prandtl number, Pr, is used as there is a greater variation in surface temperature along the disc. The exponents, C_1 and C_3, are left *free* so that the values can be compared to controlled experimental correlations. In this form the regression analysis gives:

$$\mathrm{Nu}_y = -0.384 \left(\mathrm{Gr}_y \mathrm{Pr}\right)^{0.324} + 5.231 \left(\mathrm{Re}_y \mathrm{Pr}\right)^{0.425} \tag{5.21}$$

with an $R^2 = 0.88$ and more significantly an RMS error of 6.3%. This is after rejecting outliers - based on Cook's distance (Cook, 1977) - and inspection of the p-values, which indicate the relative importance of each parameter according to the null hypothesis, i.e. the closer the p-value is to zero the stronger its importance in the regression; in this case all parameters are significant.

Figure 5.16 shows a comparison of Equation 5.21 to the experimental results for all Phase B data alongside Equation 5.18. Overall the new correlation presents a good agreement to the experimental results. There is a notable over prediction in some of the cases which was found to correlate in cases with both a high Rossby number and buoyancy parameter. This likely indicates the governing flow mechanisms are different from that of the lower Rossby numbers which tend to dominate the test programme. A combination of high Rossby, which would lead to more axial throughflow penetration, and high buoyancy parameter, stronger free convection, is likely leading to increased thermal mixing that would drive up the cavity air temperature and decreased disc heat transfer. Equation 5.21 cannot capture this effect.

Equation 5.21 is shown in Figure 5.17 for the baseline cases (a) and (b) respectively. Along with the experimentally measured local Nusselt numbers, Nu_y, and Equation 5.18. The axis is expressed as Nu_y so the data and correlations have been corrected. Although there is some variation, Equation 5.21 in Figure 5.17(a) provides a close fit to the data,

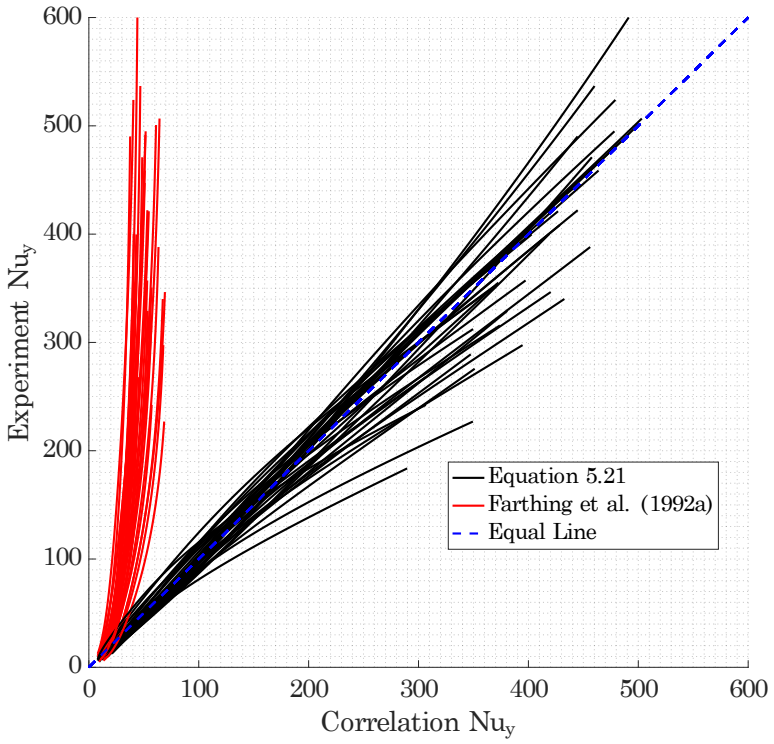

FIGURE 5.16: Comparison between measured Nusselt numbers and those predicted by Equations 5.18 and 5.21

with a slight over-prediction for most of the disc length. Equation 5.18, given its dependence on $\mathrm{Gr}_y^{0.25}$, fails to capture either the trend or the magnitude of local Nusselt. Similarly Figure 5.17(b) shows very close agreement of Equation 5.21 to measured Nusselt numbers throughout the entire disc section.

The trend of local Nusselt number in Figures 5.17(a) and (b) are worth considering in more detail. The local Nusselt number in Figure 5.13 shows a local minima at $x \approx 0.7$ and is expressed in the modified Nu_y as an inflection point. Equation 5.18 can only predict a single sense of the trend, a positive gradient giving an increasing Nusselt number towards higher nondimensional radius. The use of two separate variables in Equation 5.21 allows both a negative and positive gradient to the local Nusselt number and so can capture the experimental data more accurately.

It is suspected that competing mechanisms of forced and free convection are expressed through the inflection of the experimental data towards higher values of Gr_y.

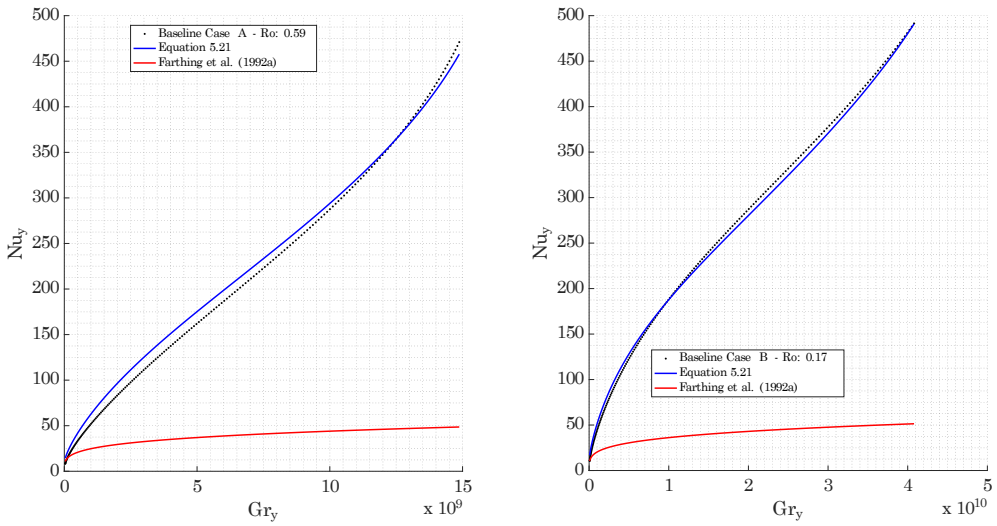

FIGURE 5.17: Experimental local Nusselt numbers against correlation prediction for diaphram surface for baseline cases A and B. The value of $\beta\Delta T$ is based upon the diaphragm average temperature (Equation 2.12)

It can be argued that this is in fact a transition from laminar to turbulent flow, in free air at $\mathrm{Gr}_y \approx 10^9$, however a separate regression analysis was performed to assess the same data using a sum of two Gr_y parameters with the expectation of exponents similar to laminar and turbulent. This failed to produce meaningful results. Figure 5.17(a) shows a slightly stronger inflection than (b) towards higher Gr_y, i.e. further from the shroud, it is thought that this is an expression of both higher Re_z and lower Re_θ (higher Ro) in that the effect of the penetration of the axial throughflow is more pronounced, especially in this low radius region and enhances the local Nusselt number. The strength of this inflection is seen throughout the test series in such cases, it is likely then that the inflection is due to the difference between the cavity flow fields; buoyancy-induced at outer radii and forced convection dominated at lower radii.

5.5.2 Average Nusselt Numbers

Whilst it is useful to estimate the local Nusselt numbers, and by extension the disc temperatures, surface average Nusselt numbers are useful in first-order energy balance of cavities and to illustrate differing flow mechanisms. Figure 5.18 shows the variation of

	$Re_z \times 10^4$		$Re_\theta \times 10^6$		$\beta\Delta T_{av}$		a/b	G	Shroud
	Min	Max	Min	Max	Min	Max			
Phase B	1.2	5.2	1.5	3.2	0.15	0.26	0.1	0.195	Heated
Farthing et al. (1992b)	2.0	1.6	0.2	5.0	0.25	0.30	0.3	0.13	Unheated
Long (1994)	2.0	1.6	0.2	5.0	0.16	0.27	N/A	0.36	Heated
Alexiou (2000)	3.3	22	1.6	11	0.04	0.09	0.1	0.135	Heated

TABLE 5.1: Test conditions used in Figure 5.18

average Nusselt number divided by $Re_z^{1.3}$ against $Ro/\left(\beta\Delta T_{av}\right)^{0.5}$, a logarithmic scale is used due to the range of data. The horizontal axis gives an indication of the ratio of throughflow effects to those caused by centrifugal buoyancy. These units allow not only determination of possible flow structure but also comparison to existing legacy data. Test conditions are listed in Table 5.1

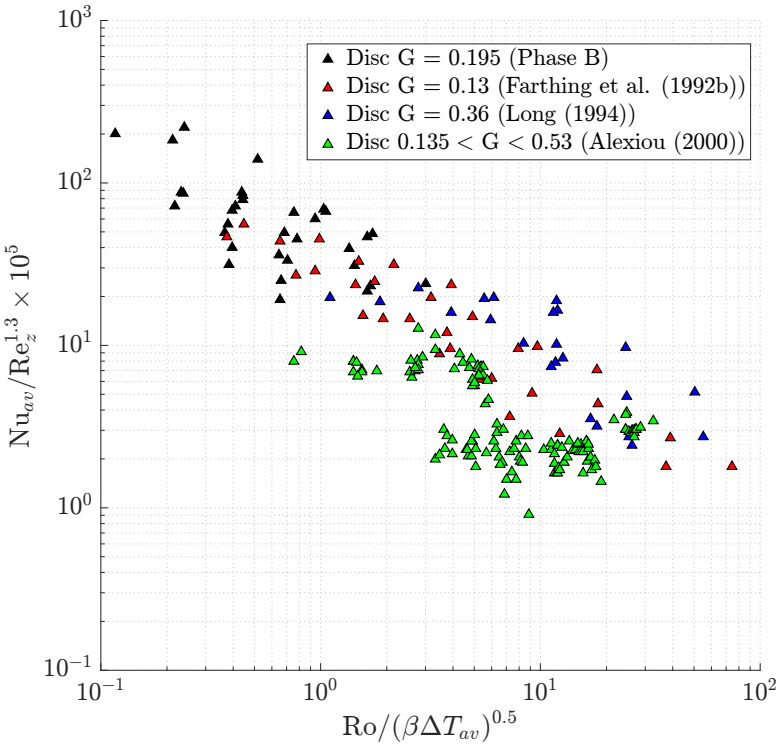

FIGURE 5.18: Disc Average Nusselt Numbers of Phase B results compared to previous works

Whilst these tests are all of rotating cavities with axial throughflow there are some important geometric differences; Long and Tucker (1994b) and Farthing et al. (1992a) both

did not feature a central rotating shaft. Whilst Alexiou (2000) did feature a central shaft these results are from a conical cavity formed by a disc and cone section, the sense of shaft rotation is not indicated as there was no discernible effect on heat transfer. There is a clear continuation of the data of Long and Tucker (1994b) and Farthing et al. (1992a) with the current test program, with similar levels of scatter present. Comparatively the results of Alexiou (2000) do not fit the trend, it is thought that this is due to both the geometric differences, inaccuracies of the experiment and uncertainty of heat transfer in low ΔT scenarios. The range of data for the current series is all $\mathrm{Ro}/\left(\beta\Delta T_{av}\right)^{0.5} < 20$. This has been suggested as the regime at which the flow is dominated by rotational effects, a finding supported by Farthing et al. (1992b) whose isothermal flow visualisation suggested that for small gap ratios the throughflow is suppressed and there is a domination of rotationally-induced buoyancy. It was previously suggested (Alexiou (2000) and Long and Tucker (1994b)) that at $\mathrm{Ro}/\left(\beta\Delta T_{av}\right)^{0.5} < 1$ the cavity becomes thermally saturated. As the axial throughflow is the thermal sink for all heat transferred from within the cavity there is a limit to the maximum value of Nusselt number that can occur for a constant value of Re_z as all of the throughflow is centrifuged into the cavity. If this were true then the current data series would level off with no further increase in Nusselt number, this is clearly not the case and we can see that there is no indication that thermal saturation has occurred.

5.6 Cavity Surfaces Heat Transfer Comparison

Figure 5.19 shows a comparison of the average Nusselt numbers from cavity surfaces discussed in this chapter. The length-scale has been modified for the shroud data set to be the consistent. On the whole the shroud and shroud corner show relatively higher Nusselt numbers compared to the disc surfaces with a similar trend to that already established in the preceding sections. This supports the conclusion that the shroud and shroud corner are the dominate heat transfer features in the cavity system and that the disc is relatively less important. However it is important to not neglect the importance

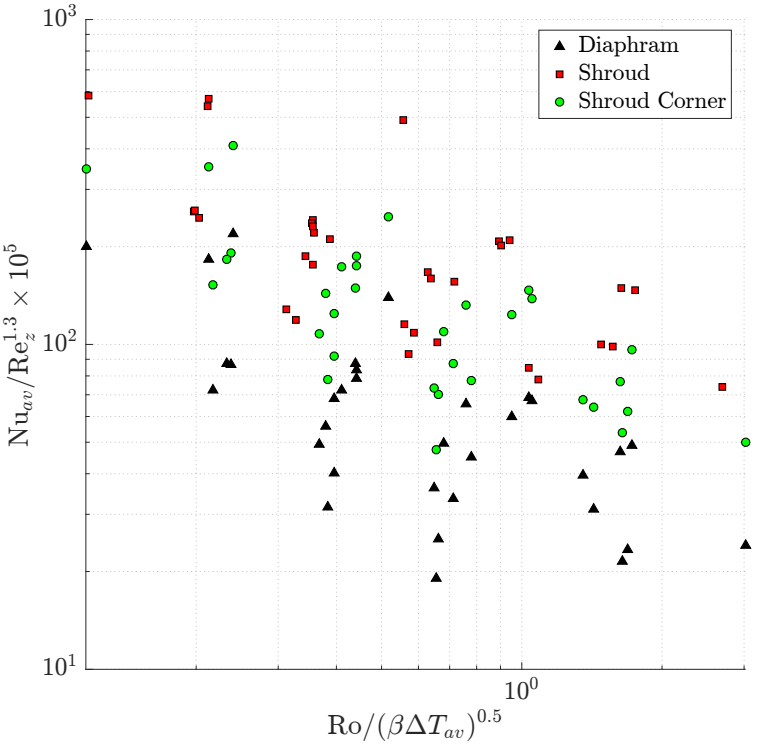

FIGURE 5.19: Comparison of Nusselt numbers between cavity surfaces

of the disc and the predictability of the metal temperatures and the impact this has on life and performance of a gas turbine engine. When looking at the mechanisms responsible for transferring heat into the coolant flow the shroud region is key. The increase in throughflow temperature between cavities is an important design factor in engines and the question of how the heat actually enters the coolant is paramount. Whilst the thermal results assist in establishing the flow regime, it cannot entirely answer this and so unsteady numerical modelling is required, this is discussed in detail in Chapter 6.

5.7 Experimental Unsteady Pressure Measurements

For the final test unsteady measurements using five pressure transducers (Section 3.2.4) were made at the same time as the thermal data used in the simulation in Chapter 6. The raw signal frequency spectra are calculated and shown for all five channels in Figure 5.20. There are a series of clear peaks in the data, with strong signal-to-noise ratios, extending

across the spectra with the last peaks in the order of 5000 Hz. The recording frequency was at 100 kHz and after anti-aliasing gives a maximum frequency resolution of 50 kHz as shown, however there is noticeable variation between channels towards the end of the spectrum as shown in the insert. The grouping of two and three channels suggests this is a facet of the two types of transducer used.

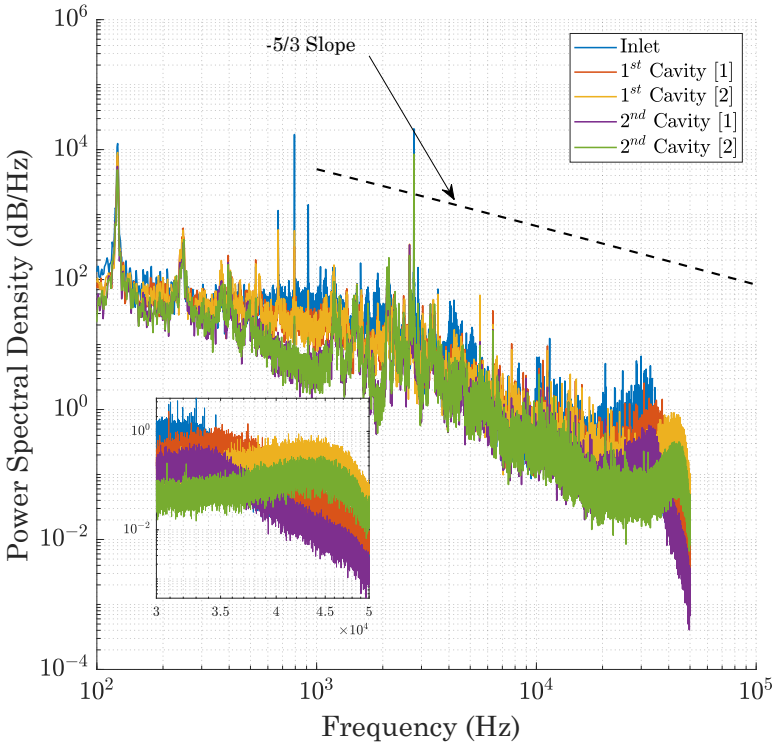

FIGURE 5.20: Power spectral density of raw unsteady pressure results for all channels; Gr= 8.94×10^{11}, $\beta\Delta T = 0.35$ and Ro = 0.29. Insert shows zoom of highest frequencies

Figure 6.26 shows the same raw signal spectra divided by the rotational frequency of the rotor, based on the fact that there is no driving frequency in the cavity system this is an appropriate choice. The six blocks representing the inlet flow restriction (Figure 3.1 K) do however give a known strong signal to match to. The rotor frequency used in this case is 132 Hz and in Figure 6.26 shows a sharp, narrow peak at x6, however by matching this exactly the fundamental x1 of the system does not align and can be seen slightly to the left at approximately x0.95. Given that the x6 is driven by the rotating blocks, and that the

other frequencies are *free* based on the fluid flow, this suggests that the fundamental is in fact showing the slip of the cavity flow field, at approximately 5%. The harmonics of this signal are also seen at x1.9 and x2.85. Indeed there are strong peaks at all multiples of the rotor frequency from 1-9, it is possible that the cyclonic and anti-cyclonic cells have been captured however it is difficult to be conclusive on this matter. Triple decomposition

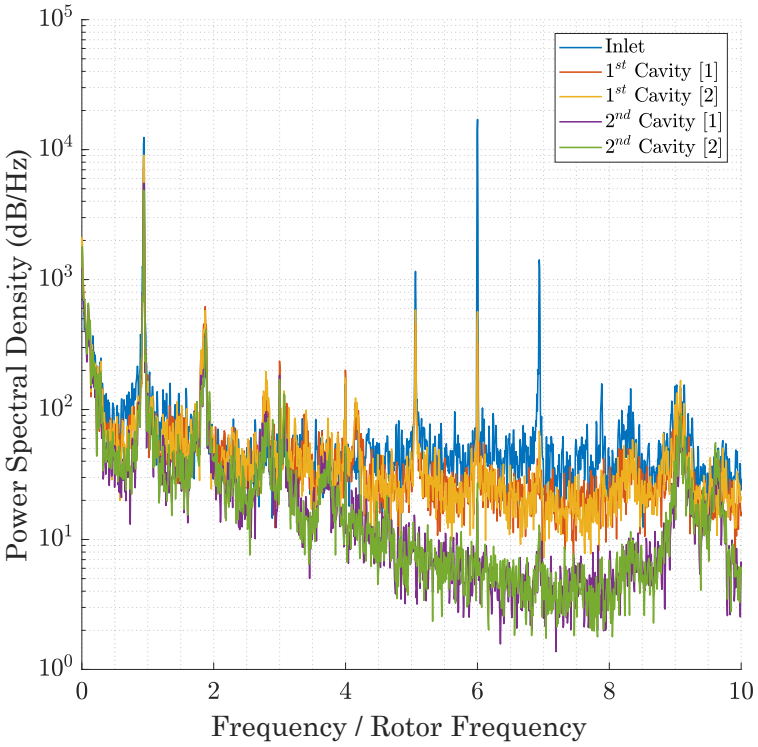

FIGURE 5.21: Power spectral density of raw unsteady pressure results for all channels divided by rotor rotational frequency 132Hz

of the raw signal into deterministic, stochastic, and periodic components is performed based on rotor rotation. The frequency spectra of the ensemble-averaged periodic and random signals are shown in Figure 5.22 up to 5000 Hz. These have been resampled from the raw data to account for minor fluctuations in the rotational speed so that each revolution is represented by the same number of data points. The periodic signal of the blocks is shown at $\approx$ 800Hz and attenuates downstream with essentially no strength by the second cavity. Whilst not seen in the periodic fluctuations, there is an indication of the first harmonic in the random component. The other strong peak is at 2778 Hz

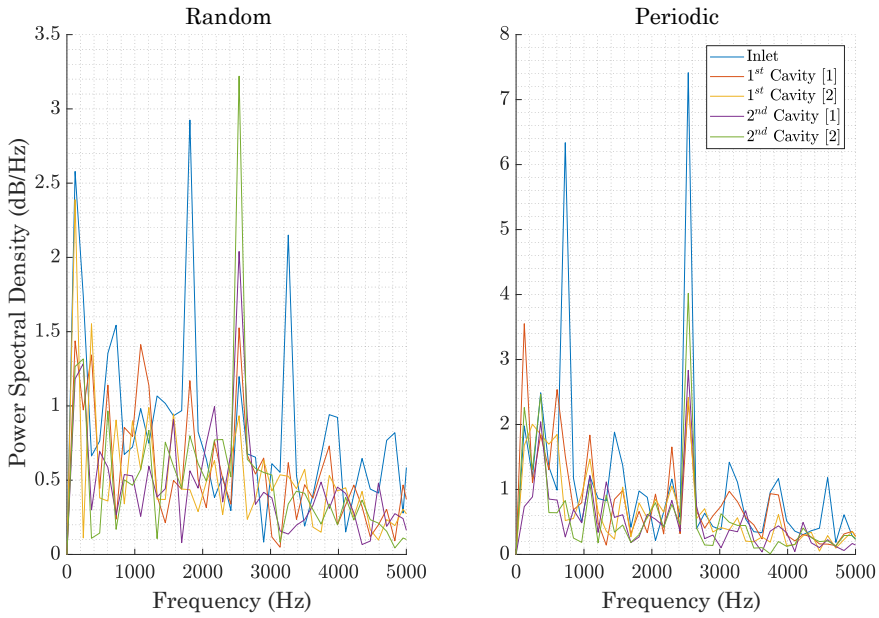

FIGURE 5.22: Ensemble-averaged frequency spectra, (a) periodic and (b) random fluctuations

and is shown in both periodic and random fluctuations. The exact nature of this signal is undetermined but is thought to be related to an acoustic resonance in the system, possibly a Helmholtz resonator formed by the cavity volume. A simple calculation was performed to calculate the Helmholtz frequency response f_H, such that:

$$f_H = \frac{a}{2\pi}\sqrt{\frac{A}{VL}} \tag{5.22}$$

where a is the speed of sound, taken at bore flow conditions, A the neck area (the cob-to-cob area), V the cavity volume and L the neck length, the vertical sides of the cob. This gives $f_H = 777$ Hz which given the block passing frequency of 792 Hz is difficult to determine and significantly lower than 2778 Hz. More investigation is required to determine the origin of this signal though it is suspected it may to be due to vortex shedding from the upstream blocks.

There are possible indications of the cavity flow structure in the random fluctuations at 260 Hz and 530 Hz. Given that these only appear in those transducers under the cavities it is thought that these could be caused by either a pair of circulations or two

pairs. Three pairs cannot be determined as this shares a frequency close to the rotating blocks. The indication of an approximate 5% slip in the cavity flow structure shown in Figure 6.26 is encouraging as this must be due to the flow field and so should be predicted by numerical simulation.

5.8 Summary

This chapter has presented the experimental results from the Phase B test programme for the cavity system. The upstream diaphragm, shroud corner and shroud has been analysed in detail and correlations produced to describe their behaviour. The shroud results demonstrate a Nusselt number profile dependent on $Gr^{1/4}$, this is in accordance with laminar free convection from a horizontal plate and yet the constant of proportionality is higher than established correlations. This suggests that the heat transfer is enhanced and it is proposed that this is due to highly unsteady laminar flow, due to the trend and magnitude of the data and the observations of the numerical results. The shroud corner Nusselt number has been considered in detail for the first time and found to correlate to a modified Grashof number with an exponent of approximately 0.4, this suggests a turbulent level of heat transfer in that region however this does not reflect the complexity of flow around a concave surface. Chapter 6 demonstrates that this region is in fact dominated by highly vortical structures that are enhancing the local heat transfer. The diaphragm surface has been analysed and suggests that the effects of both free and forced convection should be considered. A correlation has been produced based on both a modified Grashof number and Reynolds number. This correlation is compared to a previous one suggested by Farthing et al. (1992a) and is shown to give comparatively better predictions. It can also capture the inflection present in the system due to the decrease and then increase in the local Nusselt number, which are thought due to the differing flow regimes; buoyancy-induced convection at the outer radii and impinging forced convection in the lower.

6 Numerical Results

This chapter presents a numerical study conducted alongside the experimental programme. One case has been explored with dimensional parameters; Gr$= 8.94 \times 10^{11}$, Re$_z = 4.4 \times 10^4$, Re$_\theta = 2.83 \times 10^6$, $\beta\Delta T = 0.35$, $\beta\Delta T_{av} = 0.14$ and Ro = 0.29. This was the final test of the Phase B programme and featured unsteady pressure measurements. This represents an extension of the work presented in Puttock-Brown, Rose, and Long (2017).

6.1 Pre-processing

Numerical prediction of the cavity flow field has been undertaken using ANSYS Fluent 17.1. The SST k-ω turbulence model (Menter, 1994) is used as it offers the benefits of both k-ϵ and k-ω with automatic near wall treatment that switches to low-Reynolds number formulation in the viscous sub-layer. This has been shown to give good results for rotating cavity buoyancy driven flow fields (Dweik et al., 2009). Second-order temporal and spatial discretisation is used along with a pressure based solver and the PRESTO! pressure-velocity coupling scheme. Velocities were resolved in the relative reference frame.

6.1.1 Geometry

For the numerical investigation the first two cavities (in the flow direction) are modelled alongside the entire upstream inlet region in order to match as closely as possible the experimental conditions and provide a representative inlet flow field to the cavities. To aid convergence, an annular duct (300 mm x 18 mm) with a convergent outlet is used to extend the bore exit. Figure 6.1 shows a meridional and isometric view of the geometry (without the duct).

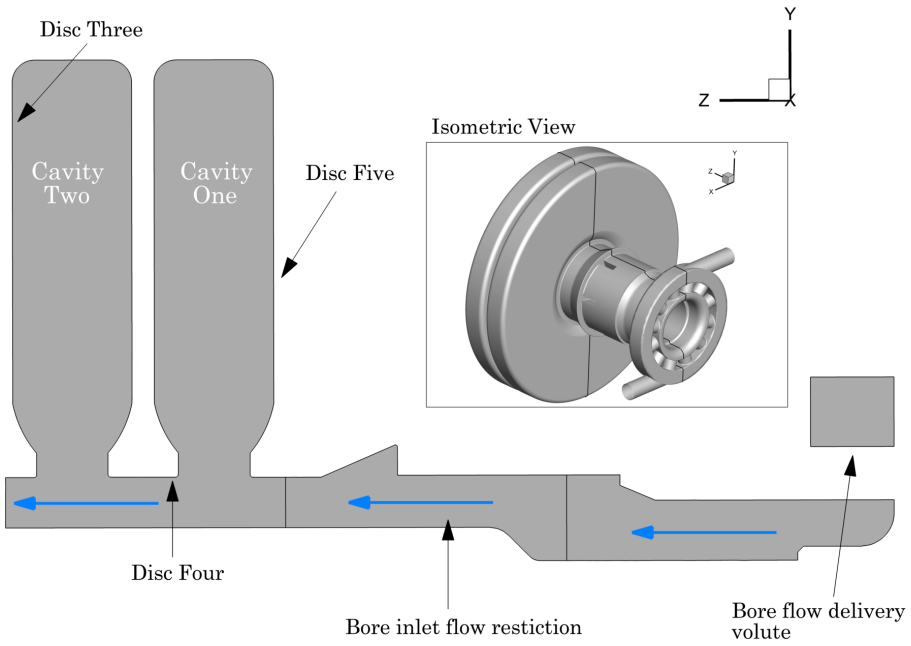

FIGURE 6.1: Meridional view of CFD geometry, insert shows isometric view.

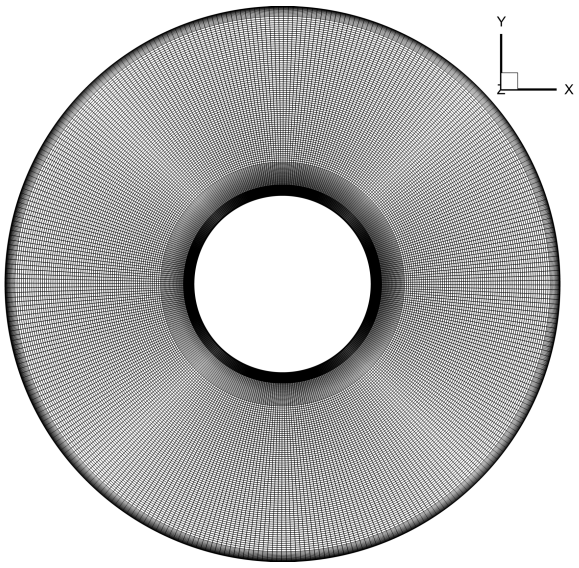

FIGURE 6.2: Circumferential mesh of cavity walls

6.1.2 Grid

A 2D multi-block grid was generated and revolved about the rotational axis using ICEM-CFD to create a 3D domain using 360 cells (each cell covering 1^o) in the circumferential direction. Following Dweik et al. (2009), the boundary layer was resolved using 25 layers up to an off wall height of 2mm on all cavity surfaces with an expansion ratio of 1.1 giving $y^+ < 1$. The twin-cavity domain consists of approximately 13 million nodes with an equal split between the two. Figure 6.2 shows a circumferential view of the domain walls.

The upstream inlet region is of lower resolution to improve computational time. Details of the inlet region are given by Puttock and Rose (2016).

6.1.3 Boundary Conditions

Experimentally measured temperatures are applied to all disc (Figure 6.3) and shroud surfaces. This is especially effective in the downstream cavity due to the number of thermocouples present. The radial temperature profiles are fitted using a second-order exponential curve as discussed in Chapter 4. In areas without sufficient instrumentation thermally matched results from a 2D axisymmetric thermo-mechanical simulation are used, in particular the downstream face of disc 5 and the inlet region. The temperatures are taken from thermally steady-state conditions, a minute (corresponding to 180 samples) of data is averaged to reduce stochastic variation. A total pressure inlet boundary (flow angle normal to surface) is used along with a static pressure at outlet, this was iterated to match the measured mass flow rate. Leakage from the pressure balanced labyrinth seals is neglected, as this is assumed negligible.

6.1.4 Solution Procedure

Initially each case was converged to a steady-state before being switched to an unsteady mode. The solutions were run for approximately 20 complete revolutions using $\approx 20\mu$s time steps that equate to 1° of rotation per step. Equation residuals for each time step reduced by three orders-of-magnitude and convergence was monitored via area-average

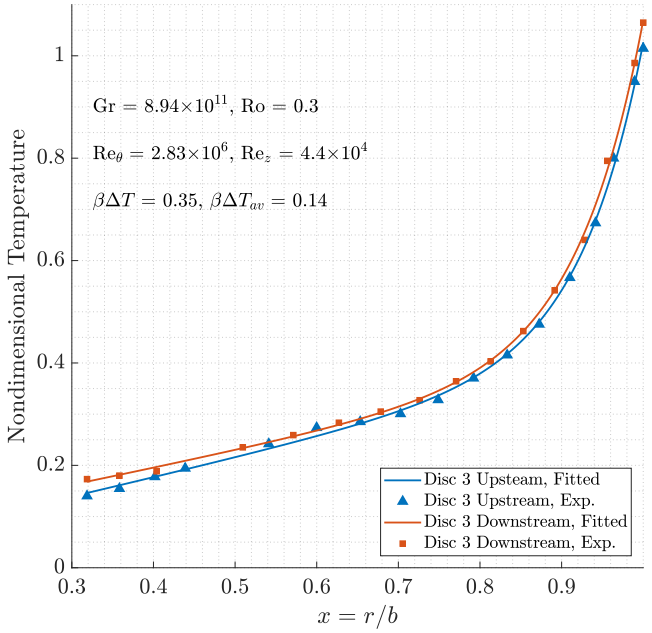

FIGURE 6.3: Nondimensional disc three surface temperatures, defined by Equation 5.1. Working conditions: Gr= 8.94×10^{11} and Ro = 0.29

heat fluxes on the cavity surfaces. As expected the flow did not become periodic but continued to evolve in time, illustrating the unstable nature of rotating cavity flow fields which is consistent with previous work (Owen and Powell, 2004).

6.2 Validation

Validation of the numerical results is presented via four methods: comparison to experimentally measured air temperatures in the downstream cavity; velocity profiles on the cavity axial mid-plane; comparison to the disc three upstream heat flux from the conduction solution presented Chapter 4 and experimentally measured unsteady pressures.

6.2.1 Nondimensional Air Temperature

Comparison is made to the cavity air temperatures measured at points; 62, 175, 176, 178, 179 and the cavity air inlet temperature 137 shown in Figure 3.3. Given that the measurements are in the rotating reference frame the comparison is made to the relative total

temperature. Figure 6.4 shows the comparison of $T_{0\text{rel}}$, the CFD results are derived from time and circumferential averages of the relative total temperature at the suitable spatial coordinate. In both cases the cavity air temperatures have been fitted with second-order polynomial trend, in keeping with the adiabatic temperature rise (Equation 5.8) assumed to occur in the rotating cavity (Long and Childs, 2007). However the bore flow temperature has not been used as T_{in}, given that the adiabatic rise cannot account for mixing in the shear layer between the cavity and axial throughflow. Whilst there is an under-prediction, the trends are aligned and near parallel, indicating the CFD has captured the underlying temperature increase throughout most of the cavity. The under-prediction cannot be attributed to an upstream temperature difference given the very close agreement in the bore region.

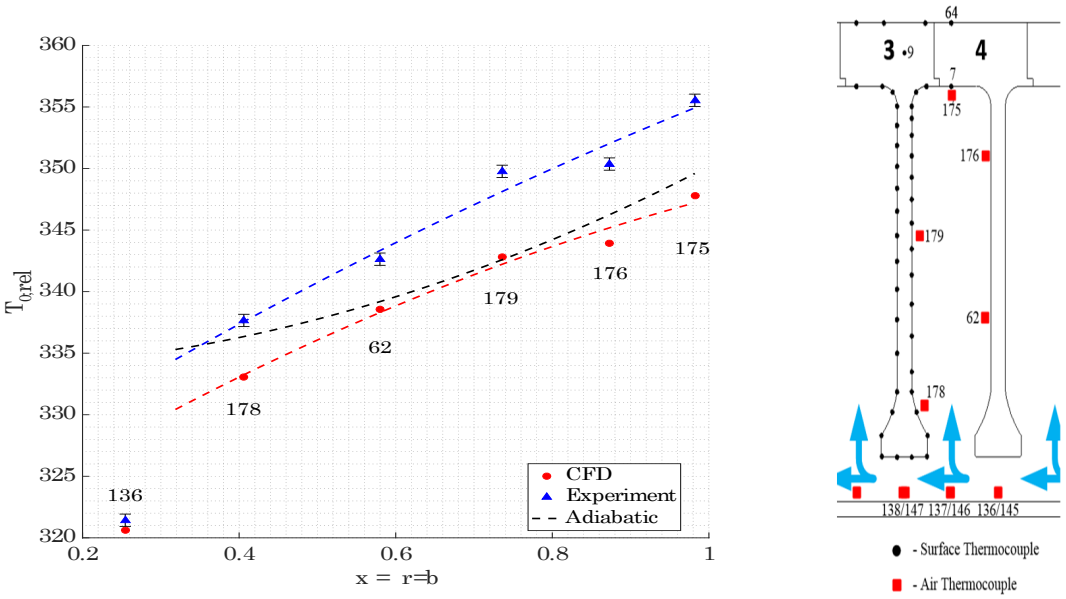

FIGURE 6.4: Relative total temperature comparison between CFD and experimental results for high speed case.

It is thought that the CFD fails to effectively capture the thermal mixing present in the cavity, a conclusion derived from the consideration that RANS models (unsteady or otherwise) are not effective at capturing large scale, predominately laminar structures such as the cyclonic and anti-cyclonic structures known to exist inside buoyancy-induced rotating cavity flows (Tucker et al., 2012).

The black dashed line using Equation 5.8 is the predicted adiabatic temperature rise in the core. This uses an assumed T_{in} from the experimental trend at $x = 0.318$. This is thought most appropriate given the lack of experimental air temperature between the cobs. Clearly the trends are dissimilar and the temperature rise is under-predicted using Equation 5.6, consistent with the results presented in Puttock-Brown, Rose, and Long (2017) where the shroud Nusselts numbers of Long and Childs (2007) show a comparatively lower value as the ΔT is under-predicted.

6.2.2 Time-Averaged Velocity Profile

Whilst this experimental programme has not featured LDA, Long, Miche, and Childs (2007) performed comprehensive measurements on a previous build of the MCR (Figure 2.6) and provides a good comparative resource. Whilst the gap ratio G is the same, there are some important geometric differences. The rotating blocks (Figure 3.1 K) act as a crude compressor and turn the flow, imparting some swirl on the axial throughflow. The annular gap ratio $d_h/b = 0.165$ places the current MCR configuration used in the CFD study with the *wide* annular gap tested by Long, Miche, and Childs (2007). Figure 6.5 shows the comparison of the low and high speed CFD cases to the experimental measurements for swirl ratio given as $V_\theta/\Omega r$, where $V_\theta/\Omega r = 1$ represents solid body rotation. Again the CFD results are circumferentially and time averaged. All data is compared on the cavity axial mid-plane.

In Figure 6.5 the CFD results (red circles) show an under-predicition of the slip ratio. Which may be due to the difference in the time-scale between the experiment and simulation. Typically LDA results are collected over several minutes (and many thousands of rotor rotations) for each data point, with a large number of observations averaged to produce a single value of velocity. The CFD results are only considered over 5 rotor rotations and so observation over a longer timescale may show better comparison. Whilst the impact of the lower Rossby number is not clear, the core flow indicates a slight negative slip. This is also seen in observed animations which indicate an approximate 90° relative translation over five revolutions of the bulk structures, equating to one relative revolution

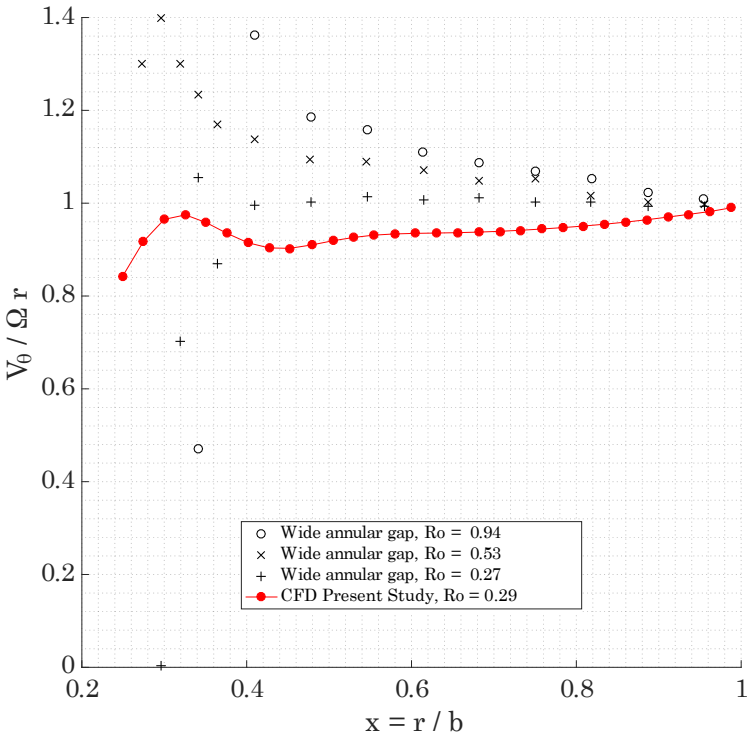

FIGURE 6.5: Comparison of circumferential and time average results of simulation compared to previous experimental results, from Long, Miche, and Childs (2007)

in twenty or a 5% slip which is indicated in Figure 6.5. Whilst there is some agreement in the bore region, it is inappropriate to compare the bore flow region directly due to the geometric differences between $0.24 \leq x \leq 0.32$.

Figure 6.6 shows the detailed circumferential average of the velocity components for the high speed case. The individual time steps are shown by black dots, the time average by red circles. The dashed line indicates the bottom of the cob. The radial velocity component is shown in Figure 6.6(a) and indicates both radial-inflow and outflow, particularly in the cob region, suggesting ingestion and expulsion of air from the cavity. Radially outward in the core region the average radial velocity is very close to zero, consistent with previous work.

The swirl ratio is shown in Figure 6.6(b). In the bore region there is a large spread of swirl indicative of the highly turbulent flow typically found in the axial throughflow.

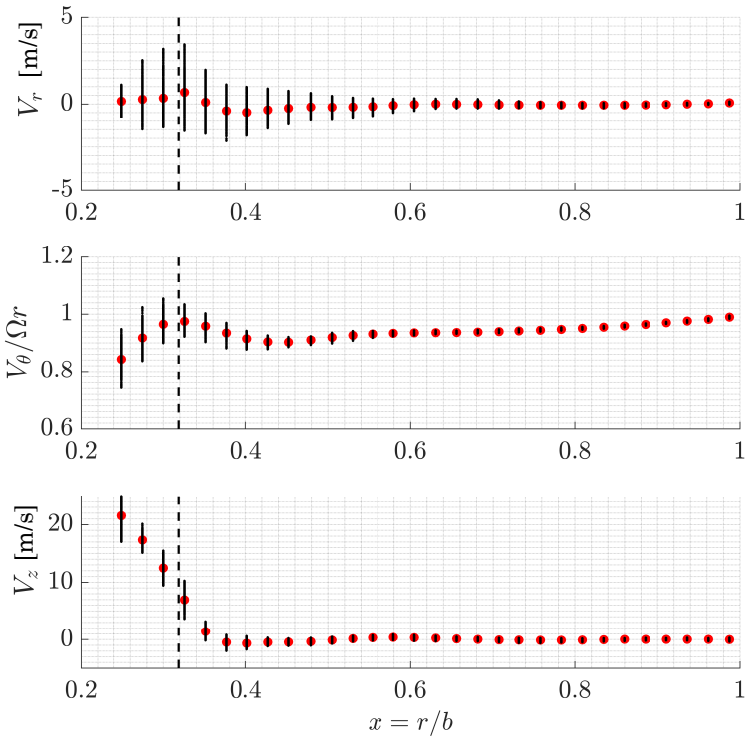

FIGURE 6.6: Component velocities; V_r and V_z and slip ratio $V_\theta/\Omega r$ from the high speed case. Circumferential averages of individual time-steps indicated by black dots and temporal average shown as red circles

Previously, Amirante et al. (2016) reported that the cob region is highly sensitive to the bore flow and that RANS typically under-predicts the swirl in this region. In the core region there is a small bandwidth (spread of black dots) indicating that the flow is relatively stable and not in a start-up transient.

The axial velocity (Figure 6.6(c)) shows large values in the bore flow, decreasing towards the bottom of cob. A moderate positive axial velocity is seen between the cobs that quickly decreases. There is no indication of a dominant separated positive and negative axial flow direction in the cob region that would suggest a toroidal vortex. Given the low Rossby number there is thought to be no toroidal vortex, instead a shear layer exists between the entrained cavity flow and axial throughflow. These results support that interpretation.

6.2.3 Wall and Shroud Nusselt Numbers

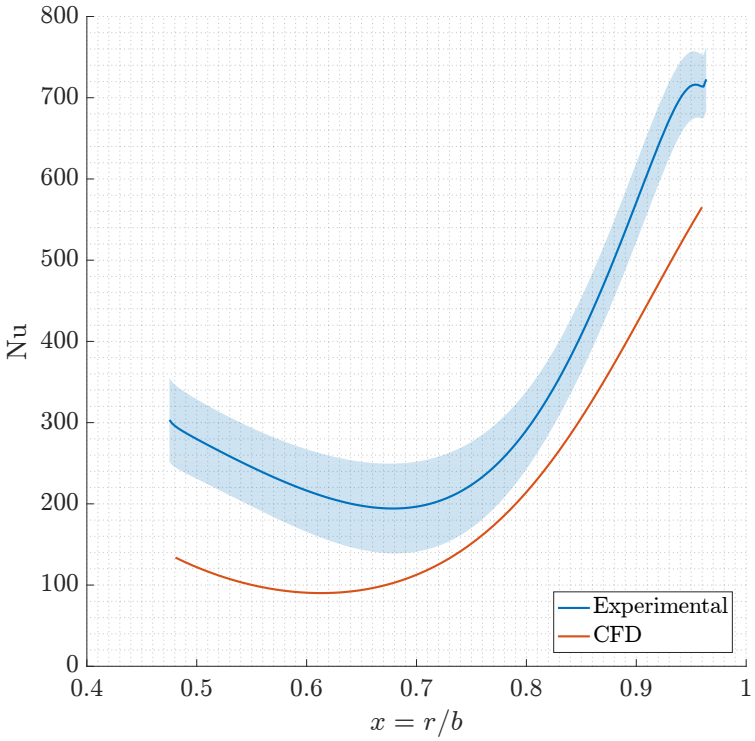

FIGURE 6.7: Comparison of circumferential and time averaged cavity downstream diaphragm Nusselt number CFD results compared to experimental

Using the experimental metal surface temperatures Nusselt numbers on the surface of the disc can be evaluated, as presented in Chapter 4, and compared to the numerical predictions. Figure 6.7 shows a comparison of the Nusselt numbers between the experiment and simulation for the downstream disc surface of cavity two (as shown in Figure 6.1). The 95% C.I. for the experimental results is also shown as the shaded area. The CFD results are taken from a circumferential and time average of the recorded time-steps. Whilst the magnitudes do not agree there is generally good agreement of the trend over the section shown. This may in part explain the under-prediction of the cavity air temperatures shown in the previous section. A lower Nusselt number indicates relatively weaker heat transfer from the metal disc into the cavity air, resulting in a lower air temperature than that predicted. This explains that the turbulent shear stresses are also likely to be low,

resulting in weaker mixing. This may therefore indicate that the mixing of the turbulence model is the reason behind the under-predicted air temperature, however further work is required to ascertain this fully.

Comparison of the area-averaged shroud Nusselt numbers predicted by the CFD and those obtained from experimental results using the 1D conduction, Equation 4.7, show agreement to within 25%. This is consistent with the findings of Sun et al. (2007).

6.2.4 Unsteady Pressure Comparison

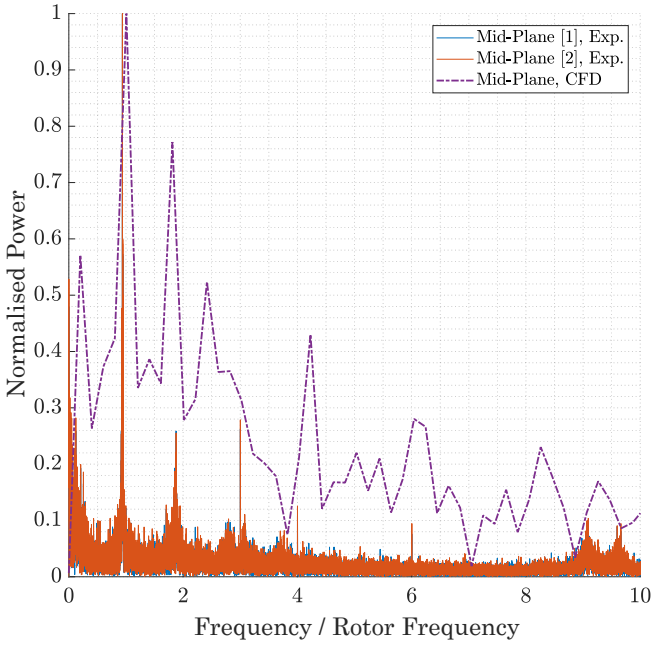

FIGURE 6.8: Comparison of circumferential and time averaged cavity downstream diaphragm Nusselt number CFD results compared to experimental

Figure 6.8 shows a comparison of the CFD results to the unsteady pressure measurements presented in Section 5.6.1 on the 2nd cavity axial mid-plane at the shaft surface. The y-axis shows normalised power, with the CFD results shown as a dashed line and the experimental results as solid lines. The x-axis shows the frequencies divided by the rotor rotational frequency of 132 Hz, with strong peaks at approximately; $\times 1$, $\times 2$ and exactly at $\times 3$, $\times 4$ and $\times 6$ times the fundamental. The CFD results show good agreement to the first

peak at appoximately $\times 1$ suggesting the slip has been captured, however this is weaker at $\times 2$ and does not show any indication of predicting a $\times 3$. This could be expected; as a sub-harmonic of $\times 6$ and the weakness of RANS models at predicting vortex shedding, especially from a blunt body such as the rotating blocks. There is indication of $\times 4$ being over-predicted whilst the $\times 6$ is moderately matched suggesting the downstream effects of the rotating blocks are captured.

Comparison of the numerical results to four separate validation measures shows that the cavity flow field has been well predicted and substantiates a qualitative assessment of the flow field.

6.3 Results & Discussion

The results presented here are all taken from the recorded time-steps of the high speed case and represent a qualitative analysis of the cavity flow field. Firstly the temporal evolution is presented using space-time diagrams and discussed in relation to the current understanding of buoyancy-induced rotational flows. Following this the instantaneous results, taken from the last recorded time-step, are discussed. Finally the numerical results are shown to indicate a previously unrecorded flow structure present in the near shroud region that has been designated as Rayleigh-Bénard streaks and are shown to modify the local heat fluxes.

6.3.1 Heat Transfer Distribution

The contribution of each cavity surface to the temperature increase of the axial throughflow air can be calculated from the wall normal heat flux and surface area. From CFD post-processing, the shroud and shroud corner surfaces contribute 66% of the heat transfered, the diaphragms 31% and the cobs 2%. These results are similar to the findings of Tang, Puttock-Brown, and Owen (2017). Individually the shroud and shroud corners contribute 36% and 30% respectively. Alternatively, the downstream cavity surfaces (cob, diaphragm and shroud corner) contribute 38% and the upstream 26%, agreeing with the

findings of Günther, Uffrecht, and Odenbach (2012) and Burkhardt, Mayer, and Reile (1993).

6.3.2 Temporal Evolution of the Flow Field

To visualise the temporal evolution of the cavity core it becomes necessary to reduce the 4D flow field to a 2D surface. Considering the cylindrical frame of reference r, θ, z in the relative (rotating with the cavity) reference frame, the inviscid momentum equation (in the case of $Ro << 1$) can be written as:

$$2\Omega \times \mathbf{v} + \frac{1}{\rho}\nabla P - \nabla\left(\frac{1}{2}\Omega^2 r^2\right) = 0 \tag{6.1}$$

Assuming an incompressible flow and taking the curl of Equation 6.1, such that:

$$(2\Omega \cdot \nabla)\,\mathbf{v} = 0 \tag{6.2}$$

from which is derived:

$$\frac{\partial \mathbf{v}}{\partial z} = 0 \tag{6.3}$$

This is the Taylor-Proudman theorem: that a slow, steady, frictionless fluid motion cannot vary in the direction of the axis of rotation and has been used successfully to characterise rotating cavities with superposed radial-inflow (Owen and Rogers, 1995). If the flow is incompressible then a similar derivation gives:

$$2\Omega\frac{\partial \mathbf{v}}{\partial z} = -\frac{1}{\rho^2}\nabla\rho \times \nabla P \tag{6.4}$$

assuming non-divergent flow and the Boussinesq approximation. Equation 6.4 is an expression of the natural tendency for rotating flow to remain two-dimensional, the baroclinic circulation in the meridional plane is counter-balanced by rotation. In the case of buoyancy-induced flow in a rotating cavity with an axial throughflow of cooling air, the structure features are expected to predominately develop in the cross-sectional plane

(Amirante et al., 2016). This tendency is reflected in the results shown in Figure 6.6(c) which show essentially zero axial flow across the cavity mid-plane in the core region.

On this basis it is useful to consider a space-time diagram of the cavity. For this a cylindrical surface of constant radius is considered extending across the core region. This surface is unwrapped and averaged in the axial direction, giving a single line that describes the selected variable. This is repeated for each time-step to build a contour map with angular position on the x-axis and time, or revolutions on the y-axis. Importantly, the velocity of a structure can be determined by its angle in a space-time diagram. All diagrams are in the relative frame, indicating that any inclined structures are moving relative to the cavity walls.

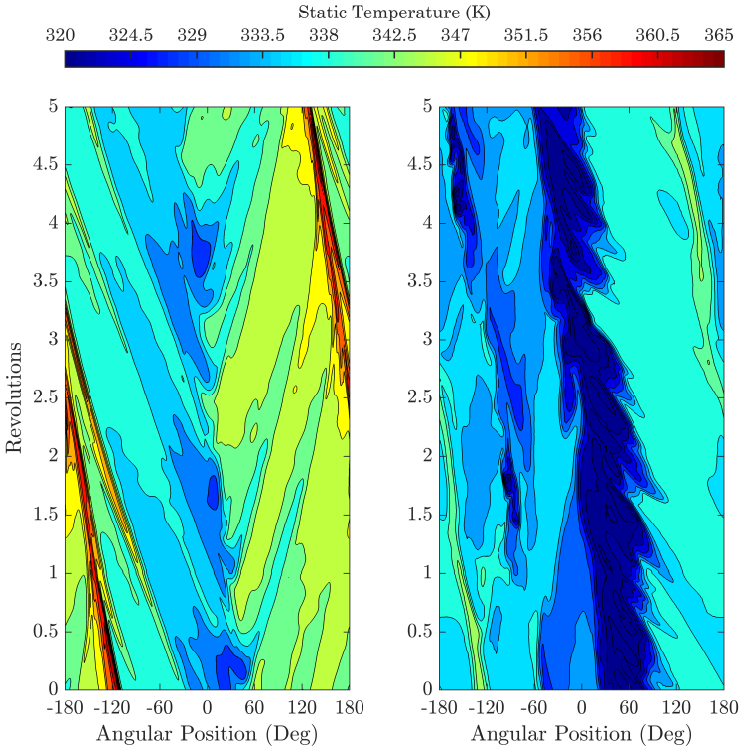

FIGURE 6.9: Static temperature space-time diagram of cavity core region. Left is at $x = 0.91$ and right is at $x = 0.45$

Figure 6.9 shows space-time diagrams of static temperature at $x = 0.91$ and $x = 0.45$ on the left and right respectively. There is a substantial plume of cold air entering the cavity, at the lower radius this is a region of air at below 320 K. This is initially at 60° and

moves relative to the rotor by approximately 90° through five revolutions, as discussed in Section 6.2.2. There is also a secondary plume developing from 1.5 revolutions onwards, the angle of this indicates a similar slip to the main plume. The bifurcation (splitting of the radial arm into cyclonic and anti-cyclonic circulations, Figure 2.3) of this plume and the relative effects of the circulation cells are indicated in the outer radius diagram. The location of the plume is still apparent yet there are a series of high relative velocity temperature contours that are moving towards a very narrow and high temperature jet approximately 150° from the plume, this is also seen at the lower radius albeit at a lower temperature. The temperature level of this jet suggests that it can only come from the shroud surface, suggesting radial inflow in the core region. To the right of the cold plume temperatures are hotter and to the left they are cooler. The bifurcation of the plume is indicative of cyclonic and anti-cyclonic circulations in the core region.

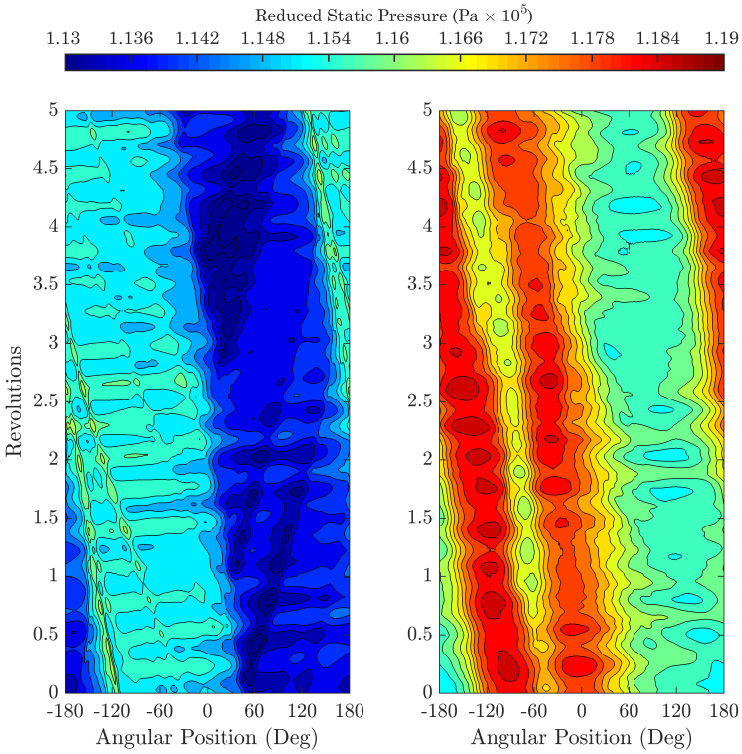

FIGURE 6.10: Incompressible reduced static pressure space-time diagram of cavity core region. Left is at $x = 0.91$ and right is at $x = 0.45$

Figure 6.10 shows the same radial levels with reduced static pressure, which can be

thought of as the static pressure in the rotating frame. The incompressible form of the reduced static pressure is defined as:

$$P^* = P - \frac{1}{2}\rho\Omega^2 r^2 \tag{6.5}$$

which is the equivalent of static pressure in the rotating reference frame. It is known that radial plumes of cold air entering the cavity bifurcate (as seen in Figure 6.9) forming the cyclone, rotating with the rotor, and anti-cyclone which rotates in the opposite direction. The different circulation directions mean that they are at two different pressures with the lower pressure corresponding to the cyclonic region. This is demonstrated in the space-time diagram of Figure 6.10, where at the higher radius there is a low pressure region indicated to the right of the plume whilst there is a high pressure region to the left, indicating cyclonic and anti-cyclonic cells respectively. The consequence of the tangential variation of P^* is demonstrated for a steady, incompressible and inviscid flow by:

$$2\Omega V_r = -\frac{1}{\rho r}\left(\frac{\partial P*}{\partial \theta}\right) \tag{6.6}$$

which shows that the radial flow V_r is caused by circumferential variation of pressure (Owen and Rogers, 1995).

The indication of a secondary anti-cyclonic cell developing is clear from the outset in the lower radial position, this is only apparent in Figure 6.9 at later revolutions. The series of near horizontal lines in Figure 6.10(a) and high pressure spots in (b) show that the flow is oscillating - that the centre of the circulations cells are moving in and out on radius - which could be indicative of a *breathing* mechanism. This would suggest that the bulk density of the cavity core is oscillating in time as the volume is fixed, a Helmholtz resonance phenomenon. This raises the question of the applicability of the form of incompressible reduced static pressure in Equation 6.6 as the density is not constant, especially when considering buoyancy-induced flow.

However it can be determined that in the case of the cyclonic cell there is a series of

increasing pressure contours (moving left to right) indicating an adverse pressure gradient. Yet the anti-cyclonic cell is already a region of high pressure, flow moves right to left in this instance and there is a favourable pressure gradient suggesting accelerating flow. Whilst this an important observation it is in the vicinity of a wall boundary layer that this becomes critical in discussing how the heat transfer is affected, which is discussed in Section 6.3.3.

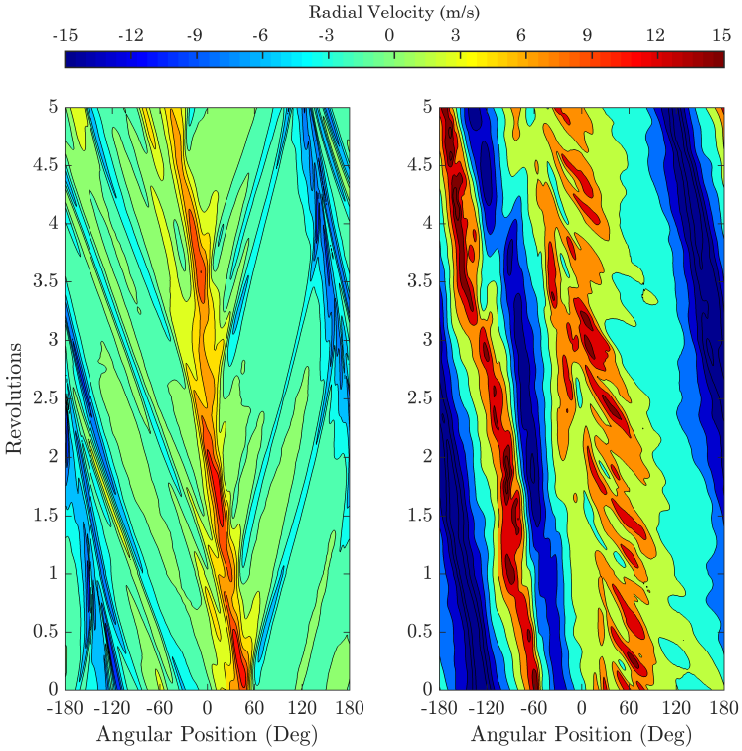

FIGURE 6.11: Radial velocity space-time diagram of cavity core region. Left is at $x = 0.91$ and right is at $x = 0.45$

Whilst Figure 6.9 suggests both radial in and outflow, the cavity velocity field is required to confirm this. Figure 6.11 illustrates the radial velocities at the same radial locations previously used, Figure 6.11(b) shows that the flow is stratified into a series of radial in- and outflows. The postulated plume region beginning at 60° is rather diffuse, suggesting a highly turbulent region rather than a strong jet. This is in contrast to the developing cell beginning at -60° that shows a much more localised outflow suggesting an almost jet like structure. In Figure 6.11(a) the plume is weaker but attenuated, there is

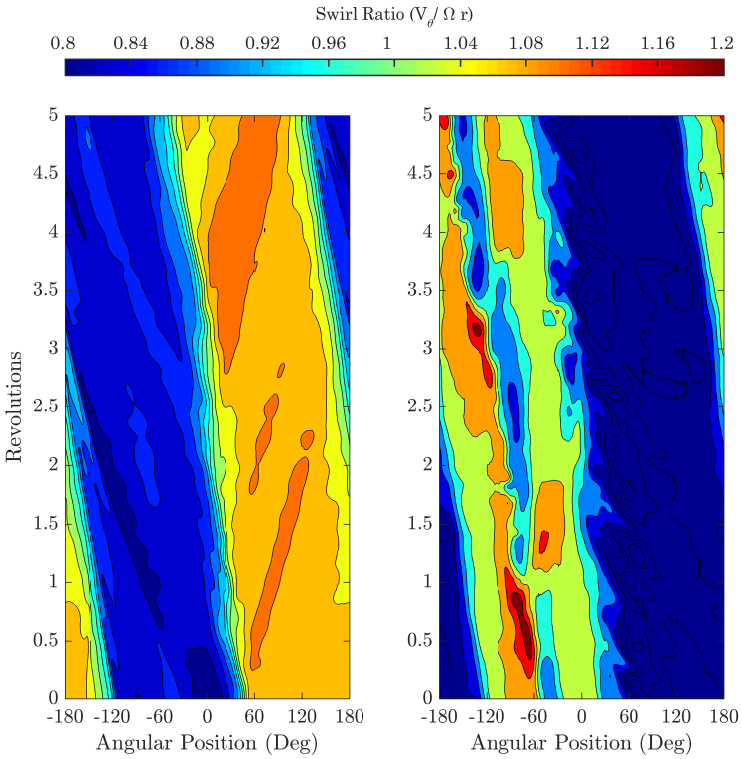

FIGURE 6.12: Slip ratio space-time diagram of cavity core region. Left is at $x = 0.91$ and right is at $x = 0.45$

no indication of the secondary jet. The bifurcation of the primary plume is visible from the streaks travelling left and right, these are extended across the entire core region to a strong localised radial inflow (this was seen in Figure 6.9 as a hot zone). This inflow is more strongly indicated by the inflow beginning at -120° in the lower radial position, here this jet like structure has a higher radial velocity, consistent with the conservation of angular momentum which would tend to accelerate radially descending flow. The secondary inflow beginning at -30° is partnered to the secondary inflow previously discussed.

Figure 6.12 shows the swirl ratio, $V_\theta/\Omega r$. Whilst the circumferentially averaged results show a 5% slip, the local values are much stronger. Beginning with the higher radial position (a); either side of the primary plume starting at 60° there a clear indication of the relative slip, on the left there is approximately -15% slip whilst to the right the slip is positive at approximately 8%, indicating anti-cyclonic and cyclonic circulations respectively.

In both circulations there are streaks of higher velocity fluid, however in the case of the cyclonic cell, these are associated with regions of denser, colder gas (Figure 6.9) flowing into the cavity. At the lower radial position the converse is true, the cyclonic cell to the right shows a strong negative slip and the anti-cyclonic shows a positive, albeit weaker slip. In the region of the secondary inflow there are unsteady slugs of strong positive slip. The inversion between the two diagrams suggests that the centre of the circulations is between $x = 0.45$ and $x = 0.91$.

It has been shown that the circumferential average of the axial velocity within the cavity is essentially zero, an expression of the Taylor-Proudman theorem. Figure 6.13 shows space-time diagrams of the axial velocity at the same locations, in (b) the inlet plume is shown as a series of negative axial velocity patches, suggesting a highly unsteady plume. This, compared with the radial velocity contours shown in Figure 6.11 in the same region, suggests a series of Kevin-Helmholtz type eddies rising from the shear layer interface between the bore region and the spacing between the bottom of the cobs. This would be consistent with previous work and, given that there is no steady stratification of the axial velocity, there is no toroidal vortex. Again the secondary outflow beginning at -60° is apparent from the outset and more stable than the primary plume.

In Figure 6.13(a) the contours of axial velocity suggest a much more two-dimensional flow. The remnants of the primary plume are shown as a series of localised but unsteady positive and negative contour bands. These are also seen to diminish in strength from approximately 3.5 revolutions, suggesting a weakening in the primary plume as the secondary gains in strength. The radial inflow jet shows essentially zero axial velocity, suggesting that the flow has become highly two-dimensional as part of the cyclonic and anti-cyclonic cells.

Figures 6.9-6.13 illustrate the unsteady nature of the cavity core region over five revolutions for the high speed case and from this series of qualitative observations can be made. There is a clear plume of axial throughflow coolant migrating radially outward from the bore region towards the shroud, this is seen to bifurcate is a manner consistent with the flow visualisation experiments of Farthing (1988) and Farthing et al. (1992b)

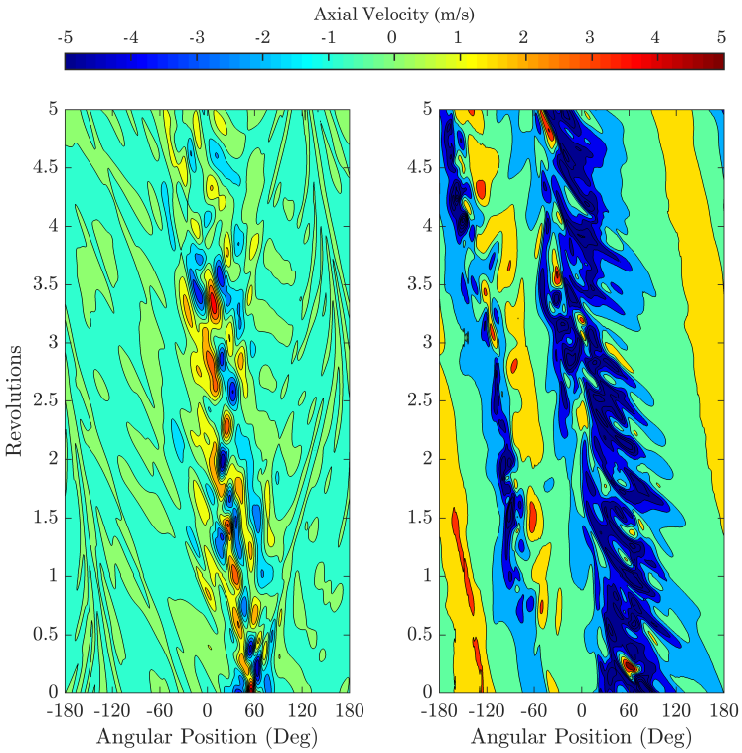

FIGURE 6.13: Axial velocity space-time diagram of cavity core region. Left is at $x = 0.91$ and right is at $x = 0.45$

and form into cyclonic and anti-cyclonic cells. A secondary plume is seen to be developing as indicated in the diagrams at lower radius and is shown to grow in strength as the primary diminishes, this is consistent with rotating cavity experiments with a heated shroud. In this case the cellular structure is unstable and is known to vacillate between multi-cellular configurations with multiple radial arms (Owen and Powell, 2004). It is likely that this is occurring and would be observed over a longer timescale.

Opposite the primary plume there is a strong jet of hot gas travelling radially inwards. This is more apparent at the higher radial location, yet there is evidence of a radial acceleration due to the conservation of angular momentum between $x = 0.45$ and $x = 0.91$ as shown in Figure 6.11. This may be linked to large scale Rayleigh-Bénard (R-B) convection. Between the cyclonic and anti-cyclonic circulation zones hot gas is drawn from the shroud boundary layer and convected in the cavity core region. Previous flow visualisation experiments by Farthing (1988) named this as the *dead zone* as none of the smoke

(introduced from the axial throughflow) was seen to penetrate into the region between the circulation zones. Similar hot gas jets emanating from the shroud surface can be seen between the cells in the instantaneous temperature difference $(T - T_{in})$ contours of Dweik et al. (2009) (Figure 2.16), though it should be stated that the nondimensional parameters are different (though not too dissimilar).

Reduced static pressure (Figure 6.10) clearly illustrates the cyclonic and anti-cyclonic structures denoted by low and high pressure regions respectively. Also shown is a series of contour bands suggesting a strong circumferential pressure gradient as flows in opposing cells converge. In the case of the low pressure cyclonic cell this is seen as an adverse pressure gradient which is known to decelerate flow, this has important implications in the presence of the shroud boundary layer. The anti-cyclonic cell is at a higher pressure and causes an acceleration of the local flow.

6.3.3 Circumferential Flow Structure

Whilst the previous section illustrates the temporal evolution within the core region and the unstable nature of buoyancy-induced flow a view must be taken of the cavity on an axial plane. This shows the circumferential and radial variations but is limited to an instantaneous snapshot of the flow field. Figure 6.14 shows the reduced static pressure P^* (Equation 6.5) on the mid-axial plane of cavity two at the last recorded time-step after five revolutions (all subsequent figures are at the same location and time unless otherwise stated and rotor rotation is counter-clockwise). The single large cyclonic region extends around the upper-right half of the cavity with the two smaller anti-cyclonic cells in the lower left. At the 12 o'clock position in the shroud periphery are several smaller structures extending radially inward showing a higher P^*. Given that the stationary frame static pressure, radius and angular speed are unchanged - with respect to local conditions - it suggests that a local, reduced density is the cause, implying hot gas is leaving the shroud. This is particularly apparent in the upper-left, this is location of the radial -inflow jet previously mentioned.

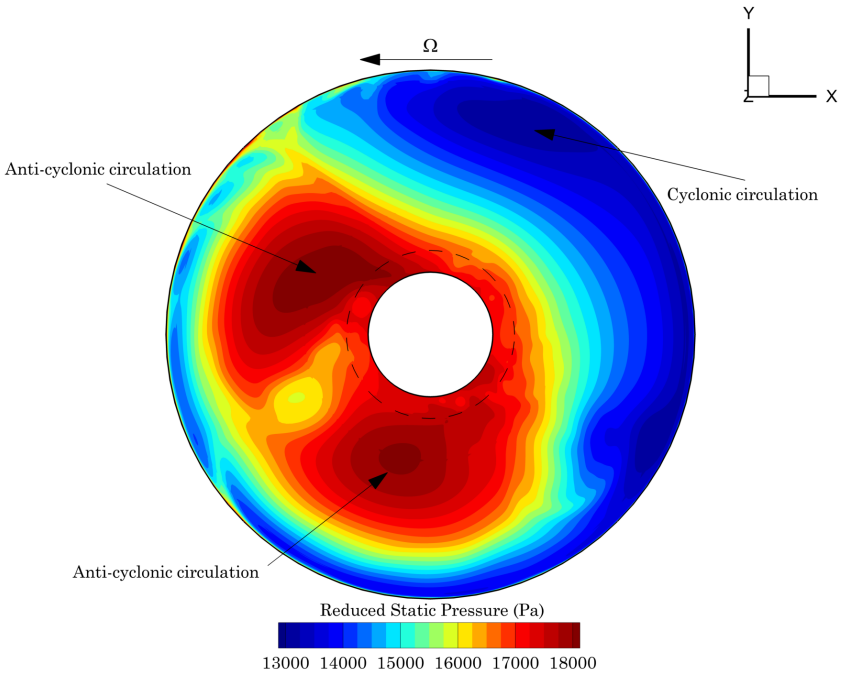

FIGURE 6.14: Cavity mid-plane reduced static pressure P^*

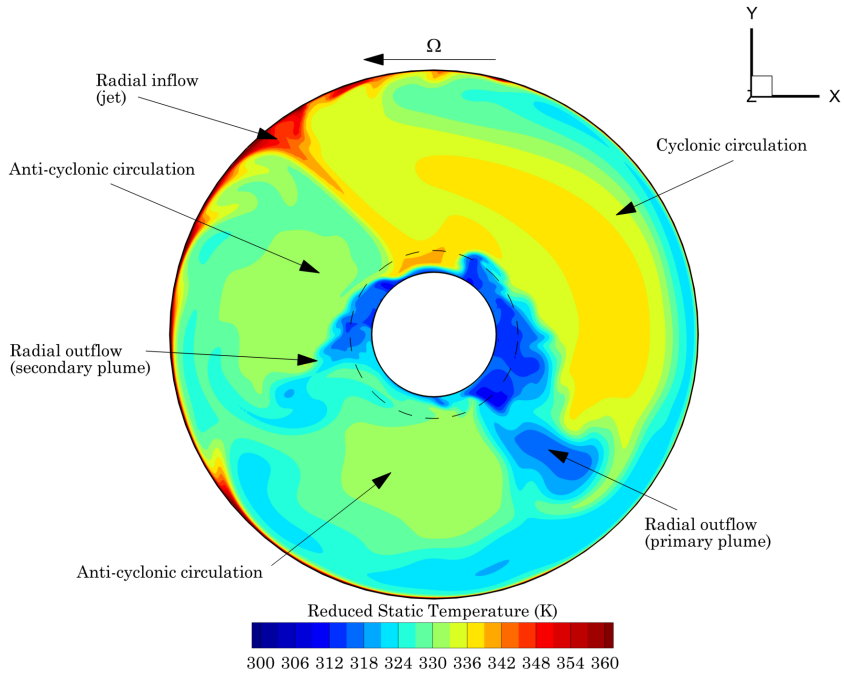

FIGURE 6.15: Cavity mid-plane reduced static temperature T^*

This interpretation of the flow is substantiated by Figure 6.15 which shows the reduced static temperature. At the same position as the low pressure inward spirals are high temperatures structures. This is most pronounced at the radial-inflow jet that penetrates deep into the cavity core region, as shown Figure 6.9 which also indicates a series of temperature waves approaching from both sides. The primary radial-outflow plume in the lower-right is clear as is the secondary plume in the lower-left. There is an indication that the top of the primary plume has developed a *mushroom* cap that bifurcates but does not impinge directly on the shroud surface, this has also been observed over animations of the flow field and is substantiated by the lack of any dependency of the shroud Nusselt numbers on Re_z (Figure 5.8). Indeed there appears to a relatively stable layer of warm gas over much of the shroud periphery.

Figures 6.16 and 6.17 show the radial and relative tangential velocities respectively. The primary and secondary plumes are shown as large areas of positive V_r indicating radial-outflow, there is also a tertiary band of radially migrating flow at the approximate 6 o'clock position that does not appear to be a plume like structure due to the lack of cold gas emanating from the bore. This does however have a small band of neutral V_r in the bore below and is shown in Figure 6.17 to be an area of high positive V_θ. This combined with the observation that the the bore region has a very high axial velocity suggests that the shear layer between the cavity and bore has deflected a relatively weak inflow and turned it outwards. The radial-inflow is dominated by the large area in the upper-left of Figure 6.16, this extends from the shroud to the shaft though the shear layer, showing an exit mechanism for flow in the cavity similar to the precessing radial-arms observed in the flow visualization experiments of Owen and Pincombe (1979). Both the cyclonic and anti-cyclonic cells are contributing to this inflow jet that is positioned between them. This region has already been indicated as the dead-zone due to the lack of any observable flow in experimentation.

The tangential velocity, V_θ contours are consistent with previous observations; the cyclonic cell is charaterised by positive flow at higher radii and negative flow at lower. Conversely the anti-cyclonic shows negative flow at higher radii and positive flow at

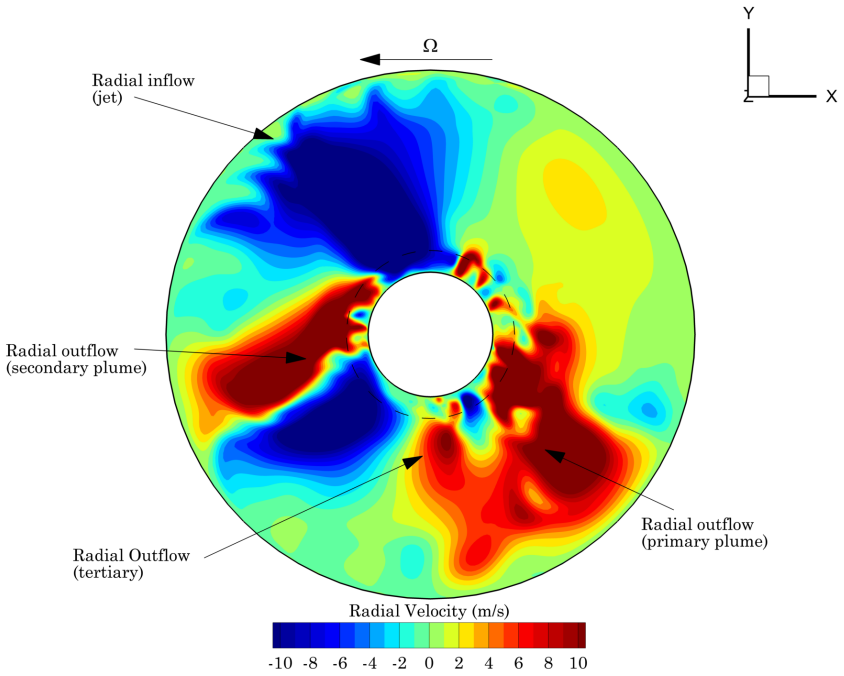

FIGURE 6.16: Cavity mid-plane radial velocity V_r

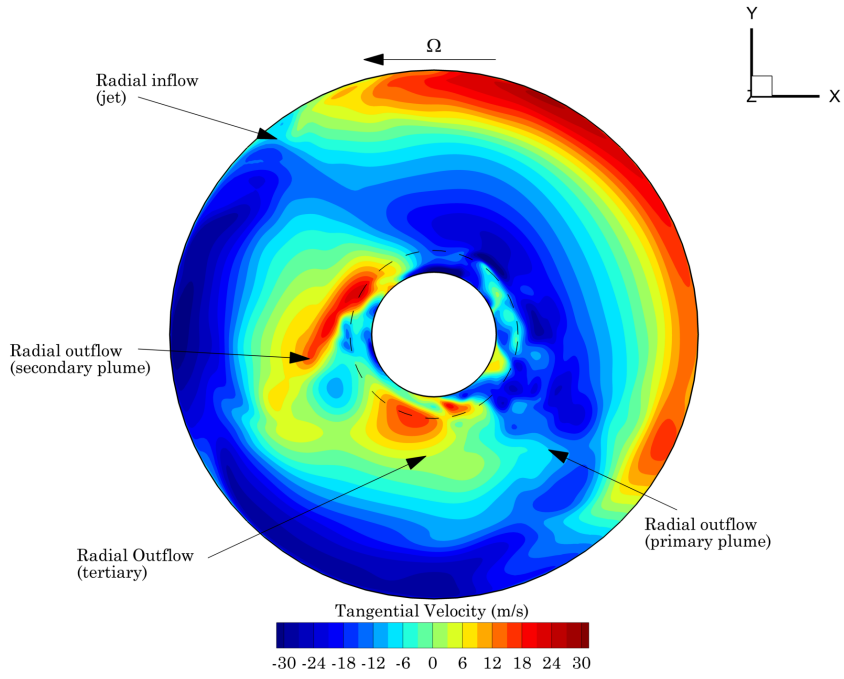

FIGURE 6.17: Cavity mid-plane relative tangential velocity V_θ

lower, circumferentially this averages very close to solid body rotation in the core region. Whilst these are a logical step in describing the flow phenomena in terms of the temperature and pressure fields they serve to decouple the two velocity components, to overcome this the vorticity field is required. Whilst the vorticity is irrelevant in terms of the pressure field it is necessary to understand the effects of the large-scale rotations and small, highly turbulent structures in the axial throughflow. Figure 6.18 shows the axial vorticity field, where a positive value indicates counter-clockwise rotation. From this the cyclonic and anti-cyclonic cells are immediately apparent and are shown to each occupy approximately half the cavity. The two radial-inflow plumes are shown to contain highly turbulent eddies of both signs, in part due to the strong streamwise trailing vortices generated by the rotating blocks at the inlet to the rotor section (Figure 3.1 K). The inflow jet contains both signs of vorticity and is entraining a series of structures from the shroud boundary layer. The shroud boundary layer above each circulation shows an opposing sign of vorticity.

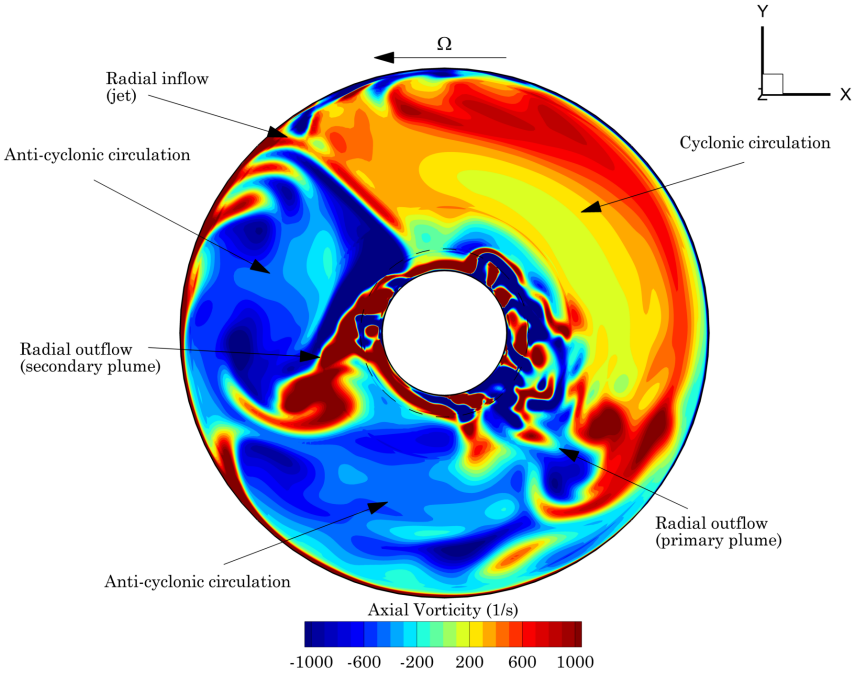

FIGURE 6.18: Cavity mid-plane relative axial vorticity ω_z

This axial cross-section illustrates the large-scale structures and substantiates the R-B natural convection interpretation of the cyclonic and anti-cyclonic cells which, due to their rotation, would manifest as a series of self-organising positive and negative vortices. However the near shroud flow in the vicinity of the radial-inflow jet suggests a highly unsteady 3D boundary layer, this requires a more in-depth investigation and in particular answering why does the shroud Nusselt numbers in Figure 5.7 suggest a turbulent magnitude of heat transfer but with a laminar trend.

6.3.4 Rayleigh-Bénard Streaks

According to the Taylor-Proudman theorem in the core of the cavity there are no axial gradients, however the near shroud region cannot be considered in the core and so it is instructive to review the meridional plane. Inspection of a series of planes illustrated a previously unreported structure in the shroud vicinity that is consistent with self-organising Rayleigh-Bénard cells stretching across the shroud. Figure 6.19 details a single meridional plane taken approximately at the 12 o'clock position (in the previous figures) for ω_θ (a), V_r (b) and T^* (c). Despite the limited bandwidth the contours of radial velocity indicate a series of in- and outflows extending across the shroud, which coincide with the cells of positive and negative tangential vorticity where the axis of rotation is perpendicular to the plane.

The reduced static temperature indicates that hot gas is drawn radially inward, against the centrifugal force, a significant way past the thermal boundary layer. Indeed the convective cells are affecting the shroud corners which shows a thin layer on the right and a bulging layer on the left. The cells are having a significant influence on the structure of the boundary layer.

R-B type convection is a 3D phenomenon and it is instructive to consider the cells in this way, Figure 6.20 shows an iso-surface of $T^* = 350$ K with the meridional cutting plane previously used indicated. The iso-surface itself is contoured according to radius, indicating the depth of the hot gas penetration. The R-B cells are seen to extend in both directions, however they are more coherent to the left and show streak-like behaviour.

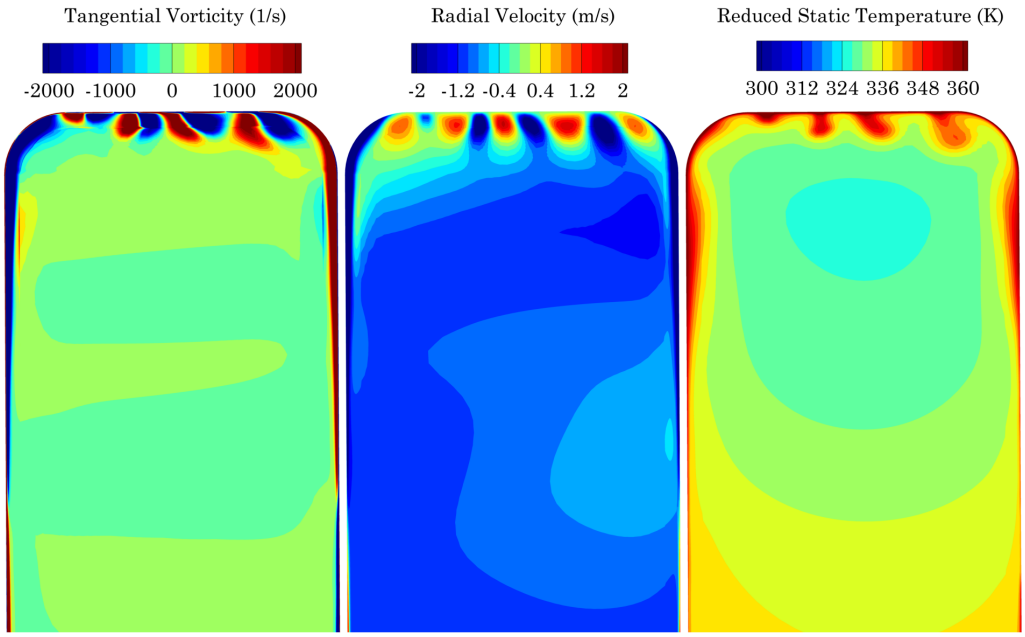

FIGURE 6.19: Cavity meridional plane at approximately 12 o'clock position for tangential vorticity ω_θ (left) and radial velocity V_r (right)

Beginning from the far left the iso-surface is approximately 0.4 mm from the shroud, as the streaks develop the contours show the gas is forced closer to the shroud and drawn radially inwards in an alternating pattern consistent with Figure 6.19. To the right of the cutting plane the streaks begin to break down, the contours show the iso-surface is moving radially inwards. This location is the radial inflow jet previously discussed.

The R-B streaks have been shown to modify the shroud boundary layer through the convective effects of the cells. Figure 6.21 shows the wall normal heat flux on the shroud and shroud corner surfaces at the same view as before. Between the radial penetrations are patches of high heat flux (at least 40% higher than the shroud average). Given that Figure 6.20 shows the gas forced closer to the shroud it is postulated that the R-B streaks are drawing colder gas towards and across the shroud surface at an accelerated velocity, enhancing the heat flux. Where there is radial inflow, the boundary layer is relatively stagnant; thick, warm and of low velocity, this would locally reduce the heat flux. The shroud corners are also indicating a higher heat flux, yet this is only associated with the cyclonic circulation. The insert in Figure 6.21 shows the whole cavity surface, the bottom half indicating higher heat fluxes in the cyclonic circulation and lower in the upper half

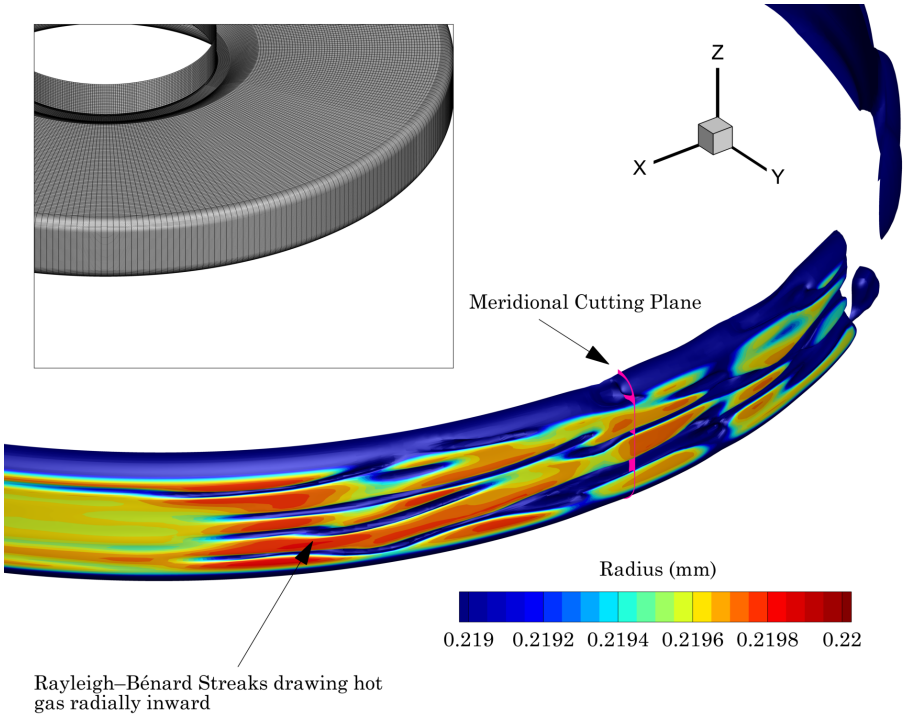

FIGURE 6.20: Iso-surface of reduced static temperature T^* at 350K, coloured by radius (mm)

where there is anti-cyclonic circulation.

The modification of the local heat flux between the cyclonic and anti-cyclonic circulation in the cavity indicates that the R-B streaks do not form on all shroud surfaces. Given that the tangential vorticity contours in Figure 6.19 show positive and negative vorticies, iso-surfaces of both would illustrate structures across the whole cavity. Figure 6.22 shows iso-surfaces of $\omega_\theta = -1000$ and $\omega_\theta = 1000$, the R-B streaks begin to form at the 1 o'clock position and are drawn along the shroud with the rotor (rotation is counter-clockwise), in the vicinity of the radial inflow jet the streaks begin to dissipate. These are associated with cyclonic circulation. The lower region does not show any indication of the streaks and is associated with anti-cyclonic circulation. The question then becomes; why do the streaks only form with cyclonic circulations?

To answer this the contours of $dP^*/d\theta$ are considered on the axial mid-plane. Previously Figure 6.14 showed that the cyclonic circulation is associated with a low pressure

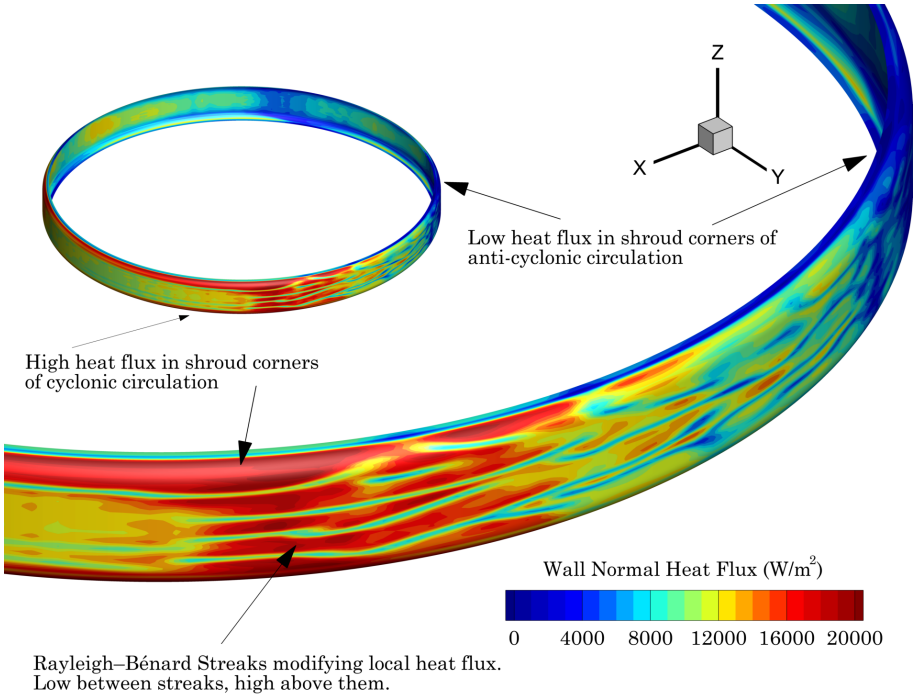

FIGURE 6.21: Wall normal heat flux (W/m^2) on shroud and shroud corner surfaces

centre and the anti-cyclonic with a high. Figure 6.23 shows $dP^*/d\theta$ with the the circulations indicated, it has already been seen that the flow: enters in a radial plume, bifurcates into opposing cells, is convected around the cavity and approaches the opposing cells. This then gives two pressure gradients; flow associated with the anti-cyclonic is at a higher pressure and finds a favourable pressure gradient, this causes it to accelerate and keep the boundary layer relatively thin. This can be seen by tracking the flow path of the anti-cyclonic circulation from the outflow, the contours indicate that the flow will encounter a negative band of $dP^*/d\theta$ first. Conversely the cyclonic circulation is at a lower pressure, as flow approaches the radial inflow it finds an adverse pressure gradient causing the boundary layer to thicken and depart the surface as it does not have the necessary momentum to overcome it. Again by tracking the flow path from the outflow along the cyclonic circulation the first strong contours are of positive $dP^*/d\theta$.

Having considered the reason why the R-B streaks are only associated with cyclonic circulation an explanation of their formation is required. Figure 6.24 shows the formation of the streaks at three tangential locations along the shroud, to illustrate them, streamlines

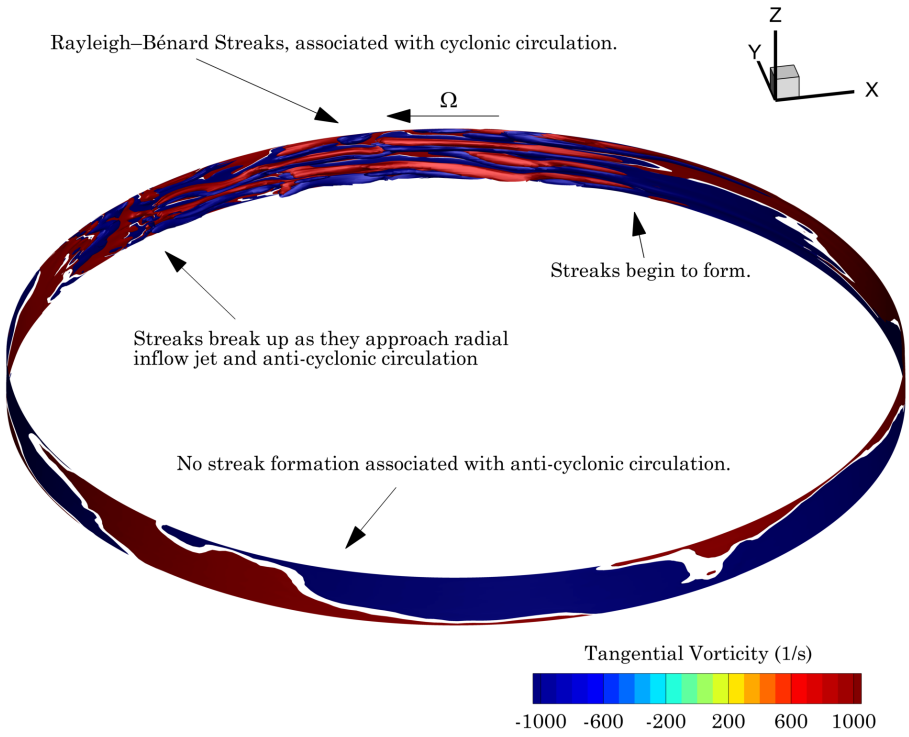

FIGURE 6.22: Iso-surface of tangential vorticity at -1000 (1/s) and 1000 (1/s)

based on the vorticity components are used showing vortex loops. The vortex loops are shown to extend across the shroud surface, around the shroud corner and down the disc wall. At some point the loops depart from the wall, cross the cavity and up the opposite disc wall completing the loop. Initially (a) the vortex loops show no perturbations across the shroud. Further along (b) vortex lines show slight perturbations (indicated) similar to the inflows of hot gas shown in the meridional plane. In the last instance (c) the vortex lines show several strong perturbations away from the shroud surface, on the left side a streamline has indicated the R-B streak itself and propagates along the shroud periphery coincident with the perturbation.

The vortex loop perturbations shown in Figure 6.24 and cyclonic circulation adverse pressure gradient (Figure 6.23) allow us to postulate on the formation of the R-B streaks. The pressure gradient in this region causes the boundary layer to thicken, this allows the formation of plumes of hot gas from the shroud surface against the centrifugal force,

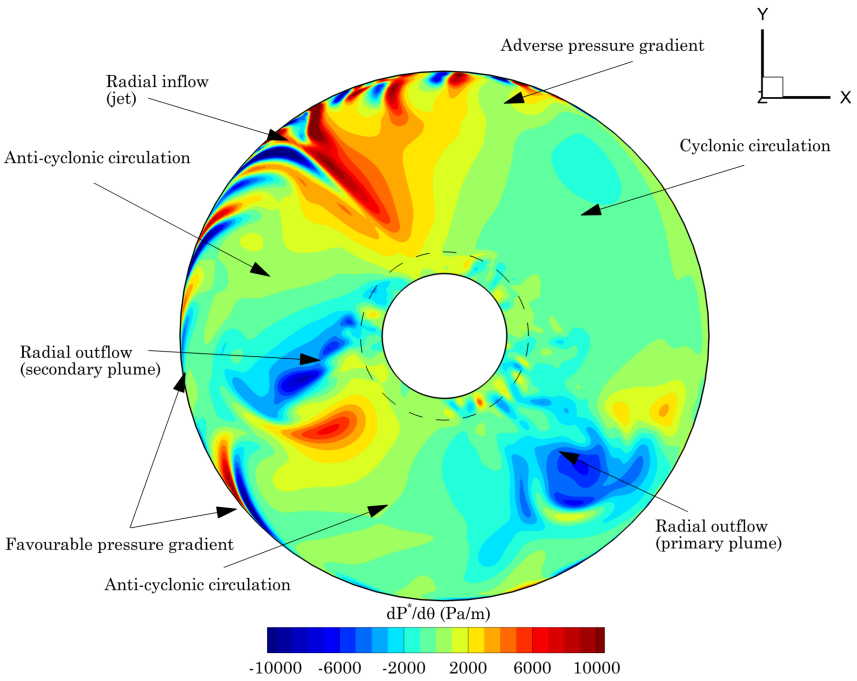

FIGURE 6.23: Cavity mid-plane of $dP^*/d\theta$

consistent with typical R-B convection in a non-rotating frame. These plumes perturb the vortex loops which move radially inwards. These perturbations are caught by the high positive tangential velocity (in this case faster than the rotor) and dragged relative to the rotor forming the convection cells into extended streaks.

There is a secondary observation that can be made with regard to Figure 6.24 concerning the radial extent of the vortex loops. It can be seen in Figure 6.19 that the wall boundary layers indicate a radial inflow, consistent with the assumed flow structure in the theoretical modelling of Owen and Tang (2015) and the observations of Farthing et al. (1992a). This radial flow combined with the rotation of the disc walls gives opposing signs of ω_θ on opposing disc walls, which are indicated in the vortex loops by the direction of the arrows, i.e. down one side of the cavity and up on the other. The radial extent of the vortex loops therefore indicates the extent of the radial inflow in the Ekman layers on the disc walls. Unlike the previously mentioned literature the flow does not travel all the way to the axial throughflow, it is instead arrested by radial outflow coming from the axial throughflow consistent with classical Ekman flow. This suggests at some locations

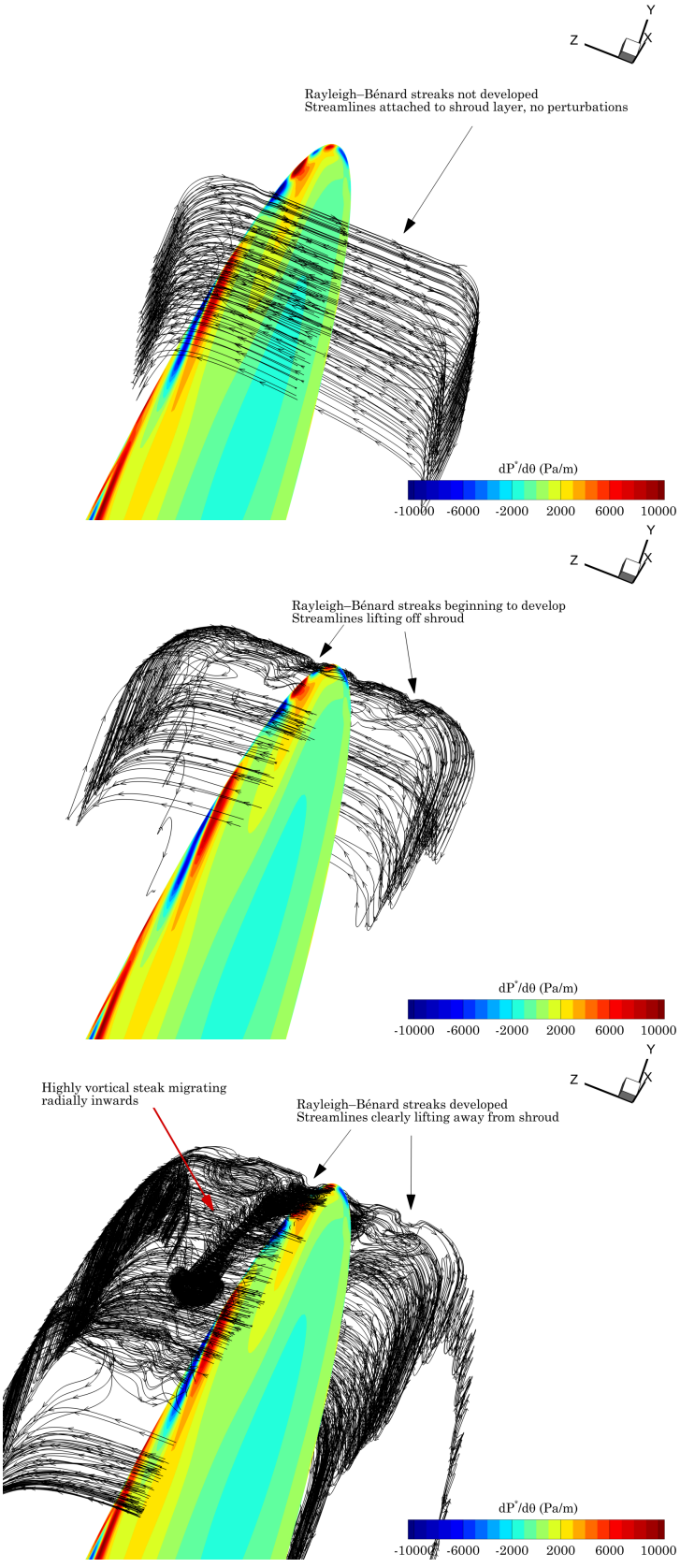

FIGURE 6.24: Vortex lines of Rayleigh-Bénard streak development

a double boundary layer on the cavity walls and explains the sharp turn in the vortex loops to the right of Figure 6.24(b), the loop when leaving the cavity wall, first turns back on itself and travels radially outward before crossing the cavity to the opposing wall.

6.3.5 Use of RANS model for Buoyancy Induced Flow

The use of RANS based turbulence modelling is questionable for the typical flow field found within a rotating cavity. It has been shown that RANS does not capture the fine detail of the large-scale rotating cells nor accurately predict heat transfer when compared to LES predictions, Sun et al. (2007). It has been shown, via experimental validation, in this chapter that the current SST k-ω URANS solution provides reasonable agreement. However the impact of turbulence modelling on the cavity flow field has not been considered. Figure 6.25(a) shows the dissipation rate (based on the turbulent viscosity) and turbulent viscosity ratio (TVR) for the high speed case at the same instantaneous time-step as before. Whilst it is not instructive to compare the results to typical turbo-machinery simulations, the relative levels show where the turbulent kinetic energy is being converted. Immediately apparent is the bore region and radial outflow plumes, the mushroom cap of the bifurcating secondary plume is clearly shown, as is the bifurcation of the primary plume. There is a strong layer around the entire circumference at the bottom of the shroud boundary layer (at highest radius), which is consistent with boundary layer modelling. The structures lifting off the shroud surface are illustrated alongside the contribution to the radial inflow jet from both cyclonic and anti-cyclonic cells, the jet itself is showing moderate dissipation which is unsurprising given its intensely vortical nature.

Figure 6.25(b) shows the TVR for the same plane. This shows that the circulation cells are of a relatively low (when compared to turbo-machinery blading simulations) TVR and that this stems almost entirely from the bore region via the radial outflows. The turbulence carried by the bifurcation of the primary plume extends significantly into both circulations cells, this is also seen in the secondary plume. In the shroud boundary layer a low TVR is seen with the thinnest region directly above the primary plume. Impingement of the bore flow on the shroud is not seen, agreeing with the results in Figure 5.8. In

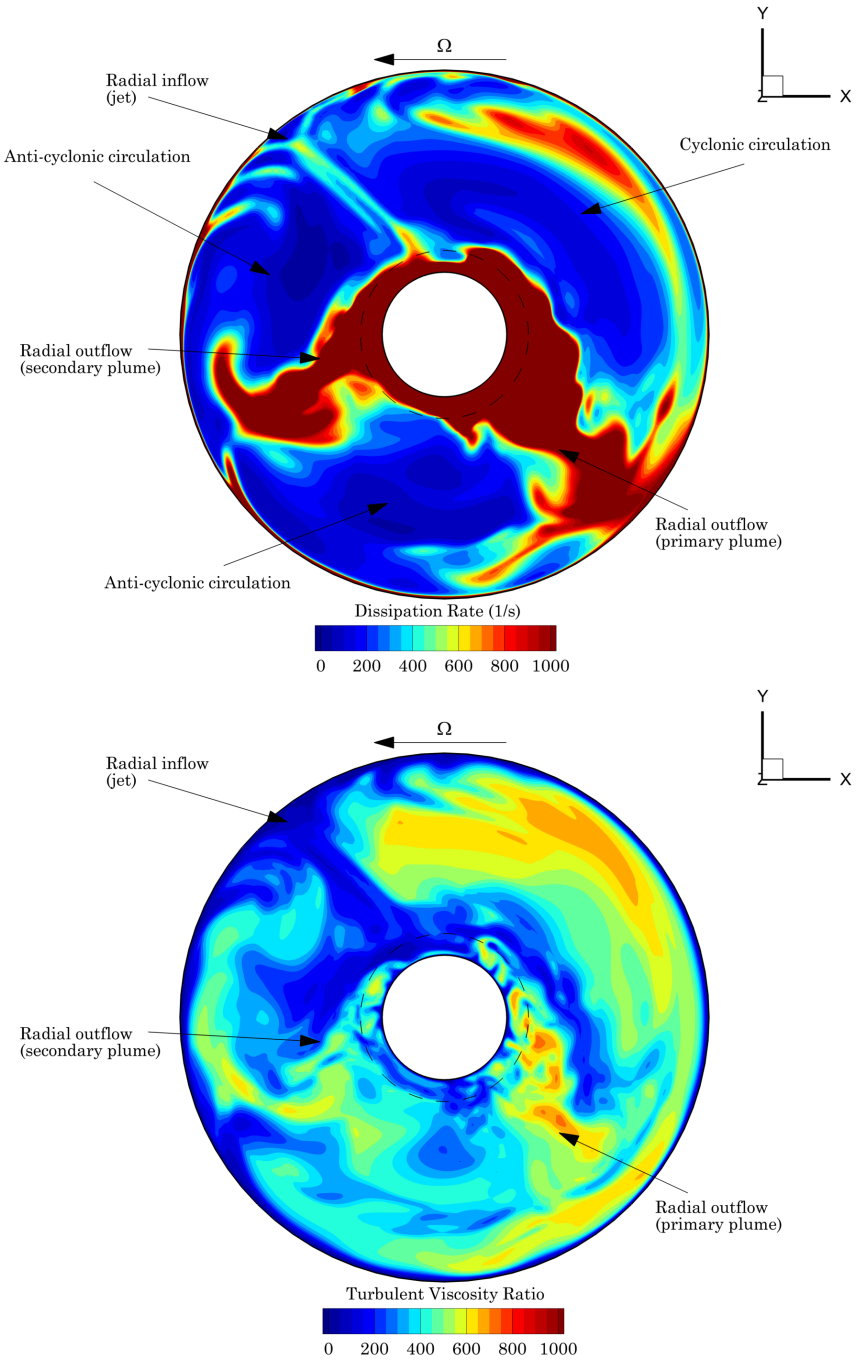

FIGURE 6.25: Dissipation rate (top) and turbulent viscosity ratio (bottom) on cavity mid-plane

both directions from the radial outflow this low TVR region thickens, however there is a notable difference, as the cyclonic cell shows a relatively uniform increase whereas the anti-cyclonic cell shows a wave-like pattern. It is not until after the centre of circulation is passed (as the boundary layer encounters an adverse pressure gradient) that the cyclonic cell shroud boundary layer is seen to destabilise. The radial inflow jet shows low TVR all the way to the bore region, suggesting its origin is in the boundary layers from the shroud surface of both circulation cells.

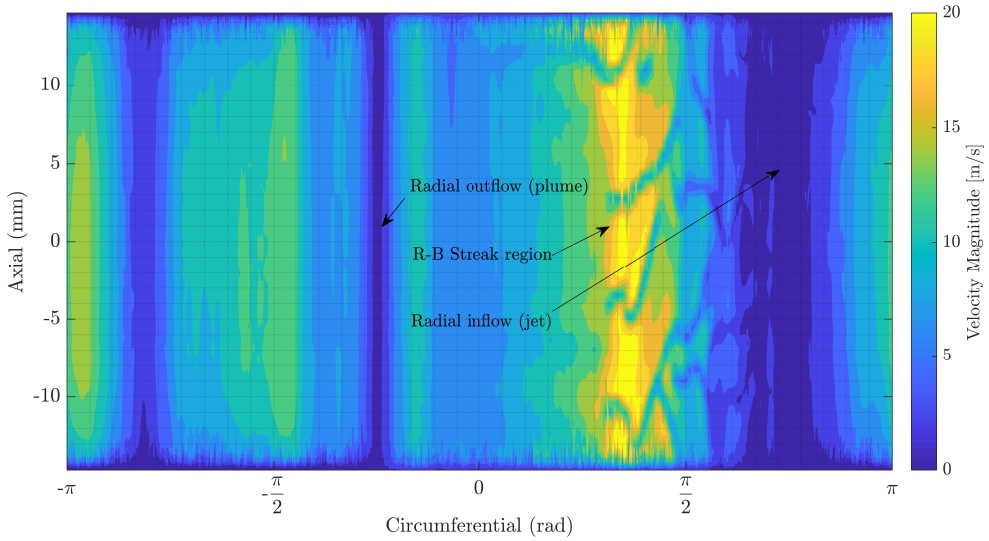

FIGURE 6.26: Velocity magnitude (m/s) in shroud boundary layer at $x = 0.9995$

The state of the whole shroud boundary layer is investigated in Figure 6.26 which shows contours of velocity magnitude 0.1 mm from the shroud surface. The axial location on the y-axis is located such that 0 corresponds to the cavity mid-axial plane The cyclonic circulation boundary layer extends from approximately $-\pi/4$ to $\pi/2$ after which the radial inflow jet is encountered. The R-B streaks form approximate $\pi/4$ before dissipating in the inflow region. The contours of the velocity, which show a predominately coherent structure indicate that the shroud boundary is indeed laminar and confirms both the interpretation of experimental results from Chapter 5 and previous work (Sun et al., 2004). There is no indication of transition which, admittedly, the RANS model would

not capture effectively. The observation that the RANS model is showing a laminar region here suggests the turbulence model is not altering the flow and that the R-B streaks are not a facet of numerical error.

6.3.6 Summary

This chapter has primarily presented the numerical results from a single URANS calculation of a low Rossby number (Ro=0.29) buoyancy driven flow field from inside a rotating cavity of the MCR. The complete inlet of the MCR is used to provide a representative flow field to allow fair comparison to experimental results. A four point comparison to new and existing results shows that the SST k-ω provides fairly good agreement albeit under-predicting the heat transfer and by extension cavity air temperatures. Space-time diagrams have been used to assess the temporal evolution of the flow-field and conform to current understanding. The shroud and shroud corner surfaces are shown to contribute 66% of all heat transferred in the cavity to the axial throughflow, underlining their importance in the study of buoyancy-induced heat transfer in rotating cavities.

The circumferential flow field for an instantaneous time-step of the high speed case has been presented. Contours of $P*$, $T*$, V_r, V_θ and ω_θ show the structure of a predominantly single pair of cyclonic and anti-cyclonic circulations with a radial outflow arm. This arm enters the cavity, travels outward and bifurcates into the circulation cells. Though it is highly turbulent, the cold gas does not impinge on the shroud surface, consistent with Figure 5.8. Where the two circulations meet a strong radially inflowing jet is observed, this region has previously been referred to as a dead zone due to the lack of observable smoke in the core, though radial inflow has been observed in the Ekman layers (Farthing et al., 1992a). This jet is shown to carry high temperature gas from the shroud boundary layer inward through the core region to the axial throughflow.

The shroud boundary layers in the cyclonic circulation are shown to be unstable, eventually forming a series of Rayleigh-Bénard streak that propagate along the shroud periphery before being drawn into the radial inflow jet. These are formed by the adverse pressure gradient thickening the shroud boundary layer allowing R-B like plumes

to develop, these are pulled by the positive relative tangential velocity eventually forming streaks and shown by the vortex loops in Figure 6.24. Whilst the existence of the R-B streaks in the shroud boundary layer cannot be ascertained without experimental evidence they have been observed under different conditions. Haramina and Tilgner (2004) used a dye technique to observe streak like structures in thermal boundary layer of R-B type convection. The streaks were found to advect with the mean flow and lift off the surface when approaching a sidewall, similar to the numerical results presented here however it must be stated the experimental conditions were very different, with Pr = 6.7 and Ra = 1.3×10^9.

The contribution of each cavity surface to the temperature increase of the axial throughflow air can be calculated from the wall normal heat flux and surface area. From CFD post-processing, the shroud and shroud corner surfaces contribute 66% of the heat transfered, the diaphragms 31% and the cobs 2%. Individually the shroud and shroud corners contribute 36% and 30% respectively. Alternately the downstream cavity surfaces (cob, diaphragm and shroud corner) contribute 38% and the upstream 26%, agreeing with the findings of Günther, Uffrecht, and Odenbach (2012) and Burkhardt, Mayer, and Reile (1993).

7 Conclusions

This thesis presents evidence that the outer surface is the dominant region of heat transfer in the rotating cavity system. Numerical URANS results indicate the shroud surface contributes 66%, the disc diaphragms 31% and the cobs 3%. Alternately the shroud can be considered as made up from the shroud and shroud corners. Individually these contribute 36% and 30% respectively which, when considering the differences in surface area between, them indicates much higher heat fluxes.

The experimental and numerical investigation of the heat transfer and flow structure of a buoyancy-induced rotating cavity flow field has been undertaken using the University of Sussex TFMRC Multiple Cavity Rig. The Phase A working conditions explored cover the range: $1.1 \times 10^5 < \mathrm{Re}_z < 5.1 \times 10^5$, $1.7 \times 10^6 < \mathrm{Re}_\theta < 3.2 \times 10^6$, $0.1 < \mathrm{Ro} < 0.6$, $0.32 < \beta\Delta T < 0.40$ and $3.1 \times 10^{11} < \mathrm{Gr} < 1.3 \times 10^{12}$. The Phase B working conditions explored cover the range: $1.2 \times 10^4 < \mathrm{Re}_z < 5.2 \times 10^4$, $1.5 \times 10^6 < \mathrm{Re}_\theta < 3.2 \times 10^6$, $0.05 < \mathrm{Ro} < 1.34$, $0.33 < \beta\Delta T < 0.51$ and $2.4 \times 10^{11} < \mathrm{Gr} < 1.6 \times 10^{12}$. A numerical study using URANS with working conditions: Gr$= 8.94 \times 10^{11}$, $\beta\Delta T = 0.35$ and Ro = 0.29 has also been presented.

Using disc metal temperature measurements and a 2D conduction model the surface normal heat fluxes have been estimated and the corresponding Nusselt numbers computed for the upstream surface of disc three (the downstream surface of the cavity formed between discs three and four). This cavity features the highest instrumentation density on a single rotating disc of any currently reported rotating cavity experiment. The typical Nusselt number of the rotating disc shows a region of high heat transfer at high radius, decreasing to a minimum at $x \approx 0.6$ before increasing again slightly. This is thought to be due to the differing flow fields; at high radius, the buoyancy-induced flow is dominant and forming a free convection flow field, and at low radius the effects of

forced convection from the axial throughflow are dominant. Using Phase B experimental results, a correlation using a modified Grashof and Reynolds numbers based on a length scale y is proposed such that:

$$\mathrm{Nu}_y = -0.384\left(\mathrm{Gr}_y\mathrm{Pr}\right)^{0.324} + 5.231\left(\mathrm{Re}_y\mathrm{Pr}\right)^{0.425} \tag{7.1}$$

Equation 7.1 does not include the effects of axial Reynolds Re_z number but reflects the interaction of the forced and free heat transfer mechanisms along the disc surface. With an RMS error of 6.3% this correlation shows agreement to the working conditions used in this thesis, though the lack of Re_z will likely limit its applicability at high Rossby numbers. However, this is not common in gas turbine aero engines.

Similarly, the shroud corner - the fillet radius between the disc diaphragm and shroud surface - has (to the author's knowledge) been investigated for the first time. Again, using a modified Grashof number the local Nusselt numbers were computed such that:

$$\mathrm{Nu}_y = 0.032\mathrm{Gr}_y^{0.391} \tag{7.2}$$

with an RMS error of 4.5%. Most significantly, the exponent of Gr_y is a very close match to the accepted value for turbulent free convection from a vertical plate, suggesting a locally turbulent flow in these corners, whereas the bulk buoyancy-induced flow field in a rotating cavity is thought to be predominantly laminar.

The shroud surface was also investigated and using a 1D heat flux equation (the 2D showed results to within 2.5%) through the rim the Nusselt numbers were calculated. Using a locally measured relative total air temperature as a reference it was shown, after radiative heat transfer corrections, that the shroud exhibits a Grashof number trend consistent with laminar free convection from a horizontal surface, yet with a magnitude similar to turbulent free convection. The results were correlated such that:

$$\mathrm{Nu}_{sh} = 0.689\left(\mathrm{GrPr}\right)^{0.25} \tag{7.3}$$

with an RMS error of 5%, where the exponent 1/4 indicates a laminar free convection.

Numerical simulation using URANS was undertaken to gain a phenomenological understanding of the rotating cavity flow field. Validation is presented using comparison to measured cavity air relative total temperatures, diaphragm surface heat transfer, measured unsteady pressures and historical laser Doppler anemometry results from a similar rig configuration. Agreement is consistent with literature results for rotating cavity simulations using RANS.

Output processing of the CFD results identified structures consistent with those predicted by Farthing et al. (1992a): cyclonic and anti-cyclonic circulations of low and high reduced static pressure respectively and radially outflowing arms. Where the circulation cells meet, a radial inflow jet of hot gas is observed. Though not identified by Farthing et al. (1992a) there are several indications in the literature of such a structure. This jet is shown to draw hot gas from the shroud boundary layer and flow radially inwards through the core region and into the axial throughflow. The link between the radial outflow arm and the inflow jet is observed using space-time diagrams which, by taking advantage of the Taylor-Proudmann theorem, illustrate the temporal evolution of the cavity core flow field.

A series of coherent structures are identified in the shroud periphery of the cyclonic circulation, referred to as Rayleigh-Bénard (R-B) streaks as they form as pairs of vortices with alternate signs, indicative of R-B type convection. These are thought to be responsible for enhancing the magnitude of the shroud Nusselt numbers in the experimental results as they are shown (in the CFD) to modify the local wall heat fluxes by at least 40% above the average. It is postulated that the formation of these streaks is due to an adverse pressure gradient in the cyclonic circulation that causes the boundary layer to slow and thicken, allowing R-B type plumes to develop extending radially inward. These are caught by the positive relative tangential velocity and dragged along the shroud periphery, forming streaks.

It cannot be confirmed that the Rayleigh-Bénard streak are physical without experimental verification. It would not be suitable to base a claim to their existence based

only on the results of a URANS simulation with turbulence modelling and it's associated shortcomings. However it should be noted that R-B streaks have been experimentally observed, albeit under very different experimental conditions (Haramina and Tilgner, 2004). Using the turbulent viscosity ratio the shroud boundary layer is shown to be laminar (consistent with experimental results), giving some confidence that the R-B streaks are not caused by numerical error.

7.1 Recommendations and future work

Future experimental work is required to prove (or disprove) the existence of the shroud Rayleigh-Bénard streaks alongside high-fidelity numerical simulation using LES or DNS. Given the contribution of the shroud to the overall cavity heat transfer this region cannot be ignored and such investigations could ultimately lead to proposals to modify the geometry of the shroud surface to control the heat transfer. Moving the study of rotating cavities from a measurement and predictive exercise to that of design and control will be paramount to maintaining optimal compressor blade tip clearances in next generation engines.

To better quantify the buoyancy-induced flow field high-frequency instrumentation - preferably in-frame - is needed. To understand the state of the shroud boundary layer, surface thin film gauges are recommended as these have been successfully used to investigate low Reynolds transition and unsteadiness in low pressure turbines (Kürner, 2014). In the short term, LDA phase-locked to on-shaft unsteady pressure measurements may be able to successfully illustrate the cavity flow structure by capturing the cyclonic and anti-cyclonic circulations and also any radial in- and outflows. Such data would also be vital in the validation of future numerical studies.

Bibliography

Alexiou, A. (2000). "Disc Heat Transfer in Gas Turbine H. P. Compressors Internal Air Systems". PhD Thesis. Falmer: University of Sussex.

Amirante, D. D. et al. (2016). "Modeling of Compressor Drum Cavities With Radial Inflow". ASME Paper No. GT2016-56505.

Atkins, N. R. (2013). "Investigation of a Radial-Inflow Bleed as a Potential for Compressor Clearance Control". ASME Paper No. GT2013-95768.

Atkins, N. R. and V. Kanjirakkad (2014). "Flow in a Rotating Cavity With Axial Throughflow at Engine Representative Conditions". ASME Paper No. GT2014-27174.

Bohn, D. et al. (1995). "Experimental and Theoretical Investigations of Heat Transfer in Closed Gas Filled Rotating Annuli". *ASME J. Turbomach.* 117 (1), pp. 175–183.

Bohn, D. et al. (2000). "Flow Visualisation in a Rotating Cavity With Axial Throughflow". ASME Paper No. 2000-GT-0280.

Burkhardt, C., A. Mayer, and E. Reile (1993). *Transient Thermal Behaviour of a Compressor Rotor with Axial Cooling Air Flow and Co-rotating and Contra-rotating Shaft*. Tech. rep. AGARD CP527, pp. 22.1–21.9.

Coleman, H. W. and W. G. Steele (1999). *Experimental and Uncertainty Analysis for Engineers*. John Wiley & Sons.

Cook, R. D. (1977). "Detection of Influential Observations in Linear Regression". *Technometrics* 19 (1), pp. 15–18.

Cooke, A. O. (2007). "Turbomachinery Disc Heat Transfer Uncertainty". PhD Thesis. Falmer: University of Sussex.

Coren, D. D. et al. (2012). "An Advanced Multiconfiguration Stator Well Cooling Test Facility". *ASME J. Turbomach* 135 (1), p. 011003.

Dweik, Z. et al. (2009). "Computational Study of the Unsteady Flow Structure of the Buoyancy-Driven Rotating Cavity With Axial Throughflow of Cooling Air". ASME Paper No. GT2009-59969.

Farthing, P. R. (1988). "The Effect of Geometry on Flow and Heat Transfer in a Rotating Cavity". PhD Thesis. Falmer: University of Sussex.

Farthing, P. R. et al. (1992a). "Rotating Cavity With Axial Throughflow of Cooling Air: Heat Transfer". *ASME. J. Turbomach.* 114 (1), pp. 229–236.

Farthing, P.R. et al. (1992b). "Rotating Cavity With Axial Throughflow of Cooling Air: Flow Structure". *ASME. J. Turbomach.* 114 (11), pp. 237–246.

Grossmann, S. and D. Lohse (2000). "Scaling in thermal convection: a unifying theory". *Journal of Fluid Mechanics* 407, pp. 27–56.

Günther, A., W. Uffrecht, and S. Odenbach (2012). "Local Measurements of Disk Heat Transfer in Heated Rotating Cavities for Several Flow Regimes". *ASME J. Turbomach* 134 (5), p. 051016.

Günther, A., W. Uffrecht, and S. Odenbach (2014). "The Effects of Rotation and Mass Flow on Local Heat Transfer in Rotating Cavities With Axial Throughflow". ASME Paper No. GT2014-26228.

Haramina, T. and A. Tilgner (2004). "Coherent Structures in Boundary Layers of Rayleigh-Bénard Convection". *Physical Review E* 69, p. 056306.

He, Xiaozhou et al. (2012). "Transition to the Ultimate State of Turbulent Rayleigh-Bénard Convection". *Phys. Rev. Lett.* 108 (2), p. 024502. DOI: 10.1103/PhysRevLett.108.024502. URL: https://link.aps.org/doi/10.1103/PhysRevLett.108.024502.

Howell, J. R. (1982). *A Catalog of Radiation Configuration Factors*. New York: McGraw-Hill Book Company.

Incropera, F. P. et al. (2006). *Fundamentals of Heat and Mass Transfer*. John Wiley & Sons.

Jaluria, Y. (1980). *Natural Convection Heat and Mass Transfer*. Pergamon.

Kantha, M. Sri (1987). *A Correlation of Heat Transfer Measurements From the Mk II Rotating Cavity Rig With an Axial Throughflow of Coolant*. Tech. rep. Report No. 87/TFMRC/TN48.

Kürner, Matthias (2014). "The Effect of Low Reynolds Number on Transition and Unsteadiness in a Low Pressure Turbine Rig". PhD Thesis. Stuttgart: Institut fü Luftfahrtantriebe der Universität Stuttgart.

Lloyd, J. R. and W. R. Moran (1974). "Natural Convection adjacent to horizontal surfaces of various platforms". ASME Paper 74-WA/HT-66.

Long, C. A. (1987). *Heat Transfer in a Rotating Cylindrical Cavity with an Axial Throughflow of Cooling Air*. Tech. rep. Report No. 87/TFMRC/106.

Long, C. A. (1999). *Essential Heat Transfer*. Longman.

Long, C. A., A. Alexiou, and P. D. Smout (2003). "Heat Transfer in H.P. Compressor Internal Air Systems: Measurements From the Peripheral Shroud of a Rotating Cavity with Axial Throughflow". *2nd International Conference on Heat Transfer, Fluid Mechanics and Thermodynamics (HEFAT 2003)*. (Victoria Falls, Zambia). Paper No. LC1.

Long, C. A. and P. R. N. Childs (2007). "Shroud Heat Transfer Measurements Inside a Heated Multiple Rotating Cavity With Axial Throughflow". *International Journal of Heat and Fluid Flow* 28 (6), pp. 1405–1417.

Long, C. A., N. D. D. Miche, and P. R. N. Childs (2007). "Flow Measurements Inside a Heated Multiple Rotating Cavity With Axial Throughflow". *International Journal of Heat and Fluid Flow* 28 (6), pp. 1391–1404.

Long, C. A., A. P. Morse, and P. G. Tucker (1997). "Measurement and Computation of Heat Transfer in High-Pressure Compressor Drum Geometries With Axial Throughflow". *ASME J. Turbomach* 119 (1), pp. 51–60.

Long, C. A. and P. G. Tucker (1994a). "Numerical Computation of Laminar Flow in a Heated Rotating Cavity With an Axial Throughflow of Air". *Int. J. Numer. Heat Transfer A* 4 (4), pp. 347–365.

Long, C. A. and P. G. Tucker (1994b). "Shroud Heat Transfer Measurements From a Rotating Cavity With an Axial Throughflow of Air". *ASME. J. Turbomach.* 116 (1), pp. 525–534.

Long, C.A. (1994). "Disk heat transfer in a rotating cavity with an axial throughflow of cooling air". *International Journal of Heat and Fluid Flow* 15 (4), pp. 307 –316.

Lopez, J. M., F. Marques, and M. Avila (2013). "The Boussinesq approximation in rapidly rotating flows". *Journal of Fluid Mechanics* 737, pp. 56–77.

Menter, F. R. (1994). "Two-Equation Eddy-Viscosity Turbulence Models for Engineering Applications". *AIAA Journal* 32 (8), pp. 1598–1605.

Miché, N. D. D. (2008). "Flow and Heat Transfer Measurements Inside A Heated Multiple Rotating Cavity with Axial Throughflow". PhD Thesis. Falmer: University of Sussex.

Owen, J. M., H. Abrahamsson, and K. Linblad (2007). "Buoyancy-Induced Flow in Open Rotating Cavities". *ASME J. Eng. Gas Turbines Power* 129 (4), pp. 893–900.

Owen, J. M. and C.A. Long (2015). "Review of Buoyancy-Induced Flow in Rotating Cavities". *ASME. J. Turbomach.* 137 (11), p. 111001.

Owen, J. M. and J. R. Pincombe (1979). "Vortex breakdown in a rotating cylindrical cavity". *Journal of Fluid Mechanics* 90 (1), 109–127.

Owen, J. M. and J. Powell (2004). "Buoyancy-Induced Flow in a Heated Rotating Cavities". *ASME J. Eng. Gas Turbines Power* 128 (1), pp. 128–134.

Owen, J. M. and R. H. Rogers (1995). *Flow and Heat Transfer in Rotating-Disc Systems. Volume 2: Rotating Cavities*. John Wiley & Sons.

Owen, J. M. and H. Tang (2015). "Theoretical Model of Buoyancy-Induced Flow in Rotating Cavities". *ASME J. Turbomach* 137 (11), p. 111005.

Patounas, D. S. (2007). "Disc Heat Transfer in Gas Turbine HP. Compressor Internal Air Systems". PhD Thesis. Falmer: University of Sussex.

Pitz, D. B. et al. (2017). "Direct Numerical Simulation of Rotating Cavity Flows Using a Spectral Element-Fourier Method". *ASME J. Eng. Gas Turbines Power* 139 (7), p. 072602.

Puttock, M. R. and M. G. Rose (2016). "Measurement of thermal wakes in compressor secondary air systems using low frequency thermocouple data". XXIII Biennial Symposium on Measuring Techniques in Turbomachinery, Stuttgart, Germany.

Puttock-Brown, M. R., M. G. Rose, and C. A. Long (2017). "Experimental and Computational Investigation of Rayleigh-Bénard Flow in the Rotating Cavities of A Core Compressor". ASME Paper No. GT2017-64884.

Sun, X. et al. (2007). "LES and RANS Investigations Into Buoyancy-Affected Convection in a Rotating Cavity With a Central Axial Throughflow". *ASME J. Eng. Gas Turbines Power* 129 (2), pp. 318–325.

Sun, Z. et al. (2004). "Numerical simulation of natural convection in stationary and rotating cavities". ASME Paper No. GT2004-53528.

Tan, Q., J. Ren, and H. Jiang (2009). "Prediction of Flow Features in Rotating Cavities With Axial Throughflow by RANS and LES". ASME Paper No. GT2009-59428.

Tan, Q., J. Ren, and H. Jiang (2014). "Prediction of 3D Unsteady Flow and Heat Transfer in Rotating Cavity by Discontinuous Galerkin Method and Transition Model". ASME Paper No. GT2014-26584.

Tang, H. (2017). "Theoretical Models of Buoyancy-Induced Flow in Rotating Cavities". PhD Thesis. Bath: University of Bath.

Tang, H. and J. M. Owen (2018). "Theoretical Model of Buoyancy-Induced Heat Transfer in Closed Compressor Rotors". *ASME J. Eng. Gas Turbines Power* 140, pp. 032605–1.

Tang, H., M. R. Puttock-Brown, and J. M. Owen (2017). "Buoyancy-Induced Flow and Heat Transfer in Compressor Rotors". *ASME J. Eng. Gas Turbines Power*. In Review.

Tang, H., T. Shardlow, and J. M. Owen (2015). "Use of Fin Equation to Calculate Nusselt Numbers for Rotating Disks". *ASME J. Turbomach* 137 (12), p. 121003.

Tian, S. et al. (2004). "Investigation of Flow and Heat Transfer in a Rotating Cavity With Axial Throughflow of Cooling Air". ASME Paper No. GT2004-53525.

Tucker, P. et al. (2012). "Hybrid LEW Approach for Practical Turbomachinery Flows - Part II: Further Applications". *ASME J. Turbomach* 134 (2), p. 021024.

Tucker, P. G. (1993). "Numerical and Experimental Investigation of Flow Structure and Heat Transfer in Rotating Cavity with an Axial Throughflow of Cooling Air". PhD Thesis. Falmer: University of Sussex.

Tucker, P. G. (2002). "Temporal Behaviour of Flow in Rotating Cavities". *Numer. Heat Transfer A* 41 (6–7), 611–627.